

Doctoral Thesis ETH No. 16290

Search for TeV-Antiprotons in Space from the
Shadowing of Cosmic Rays by the Moon
with the L3+C Detector

A dissertation submitted to the
Swiss Federal Institute of Technology Zürich

for the degree of
Dr. Sc. ETH Zürich

presented by

Yupeng Xu

Master, IHEP Beijing

born April 10th, 1971

citizen of China

accepted on the recommendation of

Prof. Dr. Felicitas Pauss	examiner
Prof. Dr. Jan Olof Stenflo	co-examiner
Dr. Pierre Le Coultre	co-examiner

Contents

Abstract	v
Zusammenfassung	vii
Introduction	1
1 Cosmic Rays	3
1.1 A brief history of cosmic ray physics	4
1.1.1 The discovery of cosmic rays	4
1.1.2 Cosmic rays as a source of high energy particles	5
1.1.3 The extensive air showers	6
1.2 The primary cosmic ray flux	8
1.2.1 Energy spectra of primary cosmic rays	8
1.2.2 The composition of cosmic rays	12
1.3 Direct measurements	14
1.3.1 Passive instruments	14
1.3.2 Active instruments	14
1.3.3 New experiments	15
1.4 Indirect measurements	15
1.4.1 The atmosphere	17
1.4.2 Air shower development	17
1.4.3 Observation techniques	21
1.4.4 Air shower simulations	23
1.5 Astrophysics and astronomy with cosmic rays	23
1.6 Summary	24
2 Antiprotons in space	25
2.1 Antimatter in the Universe	26
2.2 Antiprotons in cosmic rays: Investigations	27
2.2.1 Direct measurement	27
2.2.2 An “indirect” measurement	29
2.2.3 Estimation of the \bar{p}/p ratio from the muon charge ratio	29
2.3 Antiprotons in cosmic rays: Interpretations	30

2.4	Previous L3+C result and the present work	31
3	The L3+C experiment	33
3.1	Location and environment	33
3.2	The experimental setup	34
3.2.1	The L3 muon detector	35
3.2.2	The t_0 detector	39
3.2.3	The air shower array	41
3.2.4	The data acquisition system	42
3.3	Event reconstruction	44
3.3.1	Modelling of the detector and its surroundings	46
3.3.2	The “standard” reconstruction program	47
3.3.3	Cross-octant reconstruction	48
3.4	Detector simulation	49
3.4.1	Input interface	49
3.4.2	Muon tracking and simulation of interactions	49
3.4.3	The generic M.C. production	50
3.5	Physics topics	50
4	Detector performance and data selection	53
4.1	Data taking	53
4.2	Run selection	55
4.3	Event selection	58
4.4	Detector performance	59
4.4.1	Timing accuracy	59
4.4.2	Scintillator efficiency	61
4.4.3	Muon chamber efficiency and alignment	61
5	Angular Resolution	65
5.1	Muon propagation (multiple scattering)	66
5.2	Resolution Function	67
5.3	An unbinned maximum likelihood method	68
5.4	The detector’s intrinsic resolution	69
5.5	Angular distribution of secondary muons at surface level	69
5.5.1	Shower simulation with CORSIKA	69
5.5.2	Angle between muons and primaries	70
5.5.3	Angle between secondary muons	74
5.6	Double-muon data	76
5.6.1	The double-muon data sample	76
5.6.2	Maximum likelihood analysis	77
5.7	Summary	80

6	The Moon shadow analysis	83
6.1	The Moon shadow observations	83
6.2	Method	85
6.2.1	Coordinate systems	85
6.2.2	The Earth magnetic field	87
6.2.3	Tracing a charged particle through a magnetic field	89
6.3	Monte Carlo study	90
6.3.1	Energy distribution of primary particles	90
6.3.2	Primary cosmic-ray composition	95
6.3.3	Deflection function	96
6.3.4	Moon shadow simulation	96
6.4	The Moon data sample	97
6.4.1	The expected angular resolution	100
6.4.2	The expected deflection in the Earth magnetic field	100
6.4.3	The background	103
6.5	The shadowing effect	104
6.6	Maximum likelihood analysis	109
6.6.1	The likelihood function	109
6.6.2	Verification of the angular resolution	110
6.6.3	Search for primary antiprotons	111
6.6.4	The effect of different spectral indices on the \bar{p}/p ratio	114
6.7	Summary	115
7	Conclusion	117
	Bibliography	119
	List of Abbreviations	135
	Acknowledgements	137
	Curriculum Vitae	139

Seite Leer /
Blank leaf

Abstract

A search for antiprotons in the primary cosmic ray flux has been performed by observing the Moon shadow with the muon data collected by the L3+C experiment at CERN during 1999 and 2000.

The angular resolution of the detector and its dependences on the muon energy and zenith angle are obtained at the event level with a Monte Carlo simulation and the analysis of real double muon data using a maximum likelihood method.

The Moon shadow effect is observed in three muon momentum bands $> 100 \text{ GeV}/c$, $65 - 100 \text{ GeV}/c$ and $30 - 65 \text{ GeV}/c$ with a significance of 7.0σ , 5.8σ and 5.2σ respectively. Two dimensional maximum likelihood analyses are performed, both with binned data and unbinned data. The unbinned method gives a smaller uncertainty on the measurement of the antiproton to proton ratio. For a muon momentum cut at $70 \text{ GeV}/c$, the antiproton to proton ratio is measured to be -0.12 ± 0.11 and an upper limit of this ratio is estimated to be 0.08 (at 90% confidence level) for primary energies in the range 0.8 TeV to 2.4 TeV.

In addition, the above mentioned angular resolution is confirmed by the Moon shadow observation and the pointing precision of the detector is determined to be better than 0.1° .

Seite Leer /
Blank leaf

Zusammenfassung

Im kosmischen Primärstrahlungsfluss wurde nach Antiprotonen gesucht, indem anhand der im L3+C-Experiment am CERN in den Jahren 1999 und 2000 gesammelten Myonendaten der Mondschatten beobachtet wurde.

Die Winkelauflösung des Detektors und ihre Abhängigkeit von Myonenenergie und Zenitwinkel werden auf Ereignisebene durch eine Monte-Carlo-Simulation sowie durch die Analyse realer Daten von Myonen-Doppelereignissen unter Verwendung einer Maximum-Likelihood-Methode bestimmt.

Der Mondschatteneffekt wird in drei Myonenimpulsbändern beobachtet: $> 100 \text{ GeV}/c$, $65 - 100 \text{ GeV}/c$ und $30 - 65 \text{ GeV}/c$. Die Signifikanz beträgt 7.0σ , 5.8σ bzw. 5.2σ . Zwei dimensionsbehaftete Maximum-Likelihood-Analysen werden ausgeführt, sowohl mit Histogrammbildung als auch ohne. Das Verfahren ohne Histogrammbildung liefert für das Antiproton/Proton-Verhältnis eine geringere Messunsicherheit. Das Antiproton/Proton-Verhältnis wird für einen Myonen-Impulsschnitt bei $70 \text{ GeV}/c$ gemessen und beträgt -0.12 ± 0.11 . Für Primärenergien im Bereich von 0.8 TeV bis 2.4 TeV wird für dieses Verhältnis eine obere Schranke von 0.08 angesetzt (Konfidenzniveau: 90%).

Außerdem wird die obengenannte Winkelauflösung von der Beobachtung des Mondschattens bestätigt und die Richtungsgenauigkeit des Detektors zu besser als 0.1° bestimmt.

Introduction

Antiprotons in primary cosmic rays are subject of intense research. They may be annihilation products of dark matter candidates, or signal the presence of primordial antimatter. Cosmic-ray physics has played an important role in elementary particle studies before the accelerator era. Today, cosmologists and particle physicists find a common interest in a more elaborate exploration of these high energy messengers reaching us from deep space and far distant sources.

The Earth atmosphere is still the unique “laboratory” to study primary cosmic rays and very high energy interactions through extensive air showers. Thanks to its excellent angular resolution, the L3+C experiment provides a unique opportunity to estimate the \bar{p}/p ratio in the primary cosmic ray flux using the *Moon-shadow* method. Primary protons, charged positively, are deflected towards the East by the Earth magnetic field. The Moon absorbs part of them, which results in a deficit of primaries, to be recorded as a *shadow* on the West side of the Moon. Antiprotons, if present, will generate a shadow on the East side of the Moon. These deficits are observed through missing muons, otherwise produced in the atmosphere and pointing back, parallel to the direction of the incoming primary. The ratio of the two deficits determines the \bar{p}/p value. In this work a limit on this ratio could be obtained around 1 TeV, at energies much higher than recorded in balloon- and space-borne experiments.

Chapter 1

Cosmic Rays

The widely accepted definition of *cosmic rays* is that they are particles and high energy radiation coming from extraterrestrial space. At energies below say a TeV the primary cosmic ray flux is dominated by protons ($\sim 90\%$) and helium nuclei. The average composition changes to heavier nuclei as energy increases and at extreme energies protons may again dominate. In addition, electrons, positrons, antiprotons, gamma-rays, neutrinos, neutrons and eventually other yet unknown particles are present.

As observed from the contributions to the biennial International Cosmic Ray Conference (ICRC), a meeting place for the cosmic-ray community, the field of *cosmic rays* has a wide coverage, including topics about the Origin of cosmic rays, Galactic phenomena (OG) (accelerations and interactions); multi-wavelength and gamma-ray astronomy, gravitational wave detection; Solar and Heliospheric phenomena (SH) (Sun and corona, transient phenomena in the heliosphere, galactic cosmic rays in the heliosphere), anomalous cosmic rays, and High Energy phenomena (HE) (extensive air showers, muon and neutrino measurements, interactions and particle physics aspects) [1].

The fundamental questions like “Where do cosmic rays come from?” and “How are they accelerated to such high energies?” are puzzles throughout the nearly one-century lasting history of cosmic ray physics [2]. Today these questions are still not fully understood.

In order to answer these basic questions, a precise knowledge of the spectrum, the composition, and the propagation of the primary cosmic rays is mandatory.

In this chapter, the milestones of cosmic ray studies and their impact on other fields, mainly on elementary particle physics will be given chronologically [3–5]. This is followed by the current knowledge on the spectrum and composition of primary cosmic rays. The main techniques being or having been used for cosmic ray studies will be discussed at the end of this chapter.

1.1 A brief history of cosmic ray physics

1.1.1 The discovery of cosmic rays

Natural radioactivity was discovered in 1896 by A. H. Becquerel. Salts of Uranium could darken an unexposed photographic plate which has been carefully shielded from light. The radiation from Uranium salts also causes an electroscope to discharge. Later in 1899, E. Rutherford found that the radiation consists of two components by measuring the radiation density of the source behind aluminium foils with different thicknesses. He called the one which was dense and quickly absorbed as “ α -radiation” (or α -rays), while the one with more penetrating power as “ β -radiation” (or β -rays). In 1900, P. Villard identified a third more penetrating radiation, the “ γ -radiation” (or γ -rays).

The electroscope played an important role in these discoveries. It consists of two thin metal leaves suspended at the end of a metal bar in a closed vessel. The bar and the leaves are electronically isolated with respect to the vessel. When it is charged, the two leaves are separated due to the repellent force. When the electroscope is exposed to ionisation radiation, the ionised gas in the vessel conducts a small leakage current and causes the electroscope to discharge. The speed of the discharge indicates the intensity of the radiation.

In 1900, C. T. R. Wilson, while measuring the conductivity of air, as well as Elster and Geitel independently, observed an unknown penetrating radiation at the Earth surface using electroscopes. At the beginning, Wilson attempted to account for the radiation as of extra-terrestrial origin. However, he found that the discharge rate of the electroscope in an ordinary room and in a train tunnel under solid rocks were nearly identical. Therefore, his first hypothesis had to be discarded. Later investigations by Rutherford showed that the penetrating radiation could mainly be attributed to the radioactive substances in the vessel wall or in the rock.

More observations followed and new evidences supporting an extra-terrestrial origin appeared around 1910. The ionisation, which was measured at places far away from radioactive materials, on the top of the Eiffel Tower in Paris by Wulf in 1910, over the sea by Simpson and Wright in 1911, as well as on mountains, over a lake, and again over the sea by Pacini in 1912, was much stronger than expected.

In 1911, Gockel performed the first measurement on board of a balloon up to 4000 m above sea level. He found that the ionisation did not decrease as expected with increasing height. However, his results were uncertain because he had difficulties to calibrate the electroscope in a vessel in which the pressure varied with the outside pressure.

V. F. Hess made a major breakthrough with a series of balloon flights up to 5000 m above sea level in 1912 and 1913. Using an ionisation chamber, he discovered that the ionisation, after passing through a minimum, increased significantly with height. Therefore, he concluded that the penetrating radiation must come from above, from an extra-terrestrial origin [6]. The results of Hess were confirmed by Kolhörster with flights up to 9200 m above sea level in 1914.

The discovery of Hess marked the start of a new field. The name of *cosmic rays* was given by Millikan later in 1925.

1.1.2 Cosmic rays as a source of high energy particles

New experimental techniques very often lead to exciting and unforeseeable discoveries. A good example is the cloud chamber (Wilson chamber) developed by C. T. R. Wilson in 1911. It is a chamber filled with a mixture of vapour in equilibrium with liquid, and a non-condensating gas. When the mixture is brought into a supersaturated state either, by cooling or by expansion, condensation starts around the ions generated by the passage of charged particles leaving a visible track which can be photographed [7]. The first tracks of cosmic rays were captured by Skobeltsyn in 1929 with a cloud chamber in a strong magnetic field, which was constructed to study β -rays from radioactive decays.

In 1932, C. D. Anderson discovered a positively charged particle with similar mass as that of an electron when examining the cosmic ray tracks photographed with a cloud chamber equipped with a very strong magnet [8]. He named the new particle *positron* (meaning a positively charged electron, “positive electron”). The discovery of the positron confirmed P. A. M. Dirac’s theory:

During 1928-1930, Dirac developed relativistic quantum mechanics to describe the properties of electrons. In contrast to classical quantum mechanics, the existence of the spin and the magnetic moment of electrons are a consequence of the relativistic wave equation. Moreover, this equation had solutions with negative energies which puzzled him for a long time. In order to solve this problem, Dirac introduced a term known as *Dirac sea* in which near all the states of negative energies for electrons are occupied. A *hole* in the sea (a mirror image of the electron, the positron) will have a positive energy and charge, and behaves like an ordinary particle [9].

In 1937, S. H. Neddermeyer and C. D. Anderson using an improved cloud chamber, in which the chamber and cameras were triggered by two Geiger-counters above and below the chamber, discovered a new type of charged penetrating particles with masses intermediate between those of the electron and the proton [10–12]. They named them *mesotrons* [13] and made a nearly correct argument that the *mesotrons* might be created in pairs by photons, and that they might be represented as higher mass states of ordinary electrons [11].

The *mesotrons* presumably agreed with Yukawa’s theory of nuclear forces in which the short-range nuclear force which binds the neutrons and protons together in a nucleus is mediated via exchange particles of about 250 electron-masses. This was questioned at that time, however, since the new particles did practically not interact with matter. The name was changed to *meson* in 1939 [14], and later to *mu meson* when more intermediate-mass particles were discovered. Today, the name of *meson* is used for subatomic strongly interacting particles composed of an even number of quarks and antiquarks and the *mu meson*, now called *muon* has been identified to be a member of the family of leptons.

More particles were discovered with cloud chambers in the 1940s. These were the charged and neutral *kaons* (K^+ , K^- , K^0), with a mass about half that of the proton, and a heavy particle, the *Lambda* (Λ).

In contrast to the cloud chamber, which can make charged particle tracks visible over a large volume, another classical particle detection technique, the photo emulsion plate can provide very high positional precision ($\sim 1 \mu\text{m}$) and this played a key role in the discovery

of X-rays and radioactivity in the 1890s. It is still being used in some circumstances today (see Section 1.3.1). According to Ref. [7], an emulsion is made, as a photographic film, of silver salt, usually bromide, embedded in gelatine and spread thinly on a substrate. Powell and his collaborators improved this technique and developed the so called *nuclear emulsions* which were sensitive to all charged particles known at that time, in particular to electrons. With stacked layers of emulsion, which could be separated and developed individually, they obtained three-dimensional pictures of the interactions taking place in the emulsion. In 1947, Powell discovered with this technique the *pion* (π), the second *meson* (after the *mu meson*) through the successive decay $\pi - \mu - e$. This particle had the properties predicted by Yukawa in 1936, i.e. a mass of $274 m_e$ and with strong interactions with nucleons [15].

Few more particles were discovered in cosmic rays in the early 1950s. They were the Ξ particle, discovered in 1952, and the Σ particle in 1953. Since then the study of elementary particles was taken over by accelerators. The density and energy of the artificial beams of particles could be precisely measured and controlled. Table 1.1 is a compilation of the early discoveries in elementary particle physics.

1.1.3 The extensive air showers

Another important discovery in cosmic ray studies is the existence of the *extensive air shower*.

The showers of secondary particles produced when cosmic rays pass through matter, for example a lead plate, had been investigated with cloud chambers in the early 1930s by numerous observers [17–21]. Ref. [22] reviewed the experimental studies and theoretical deductions of these types of local showers up to 1938.

In 1938, Pierre Auger observed coincidence signals with three detectors which were separated up to 300 m at sea level, as well as at altitudes of 2900 m and 3500 m in the Alps (in particular at the Jungfrauoch) [23–25]. In contrast to the local showers which were produced in material placed above the detectors, coincident particles over large distances must be produced at high altitude in the atmosphere. Auger named this phenomenon *Extensive Atmospheric Showers* or *EAS*. The largest energies of the primary particles were estimated to be about 10^{15} eV.

In 1946, Bruno Rossi in the USA and Georgi Zatsepin in Russia started experiments on the structure of Auger showers [26]. In 1962, John Linsley discovered the first primary cosmic-ray particle with an energy of about 10^{20} eV with the Volcano Ranch array in New Mexico [27]. The most energetic cosmic ray shower with an energy of 3×10^{20} eV was detected in 1991 by the Fly's Eye experiment when operating in the monocular mode [28].

Today, observing extensive air showers (with different techniques) is, due to the very low flux, still the only possible method to study ultrahigh-energy cosmic rays. A new project named after Pierre Auger began in 1995 to explore ultrahigh-energy cosmic-ray particles exceeding 10^{19} eV [29].

Table 1.1: Early discoveries in elementary particle physics. This table is a modified version of the one from Ref. [16].

Particle	Year	Discoverer (Nobel Prize)	Method
X-ray	1895	W. Röntgen (1901)	Cathode rays, emulsion plates
e^-	1897	J. J. Thomson (1906)	Cathode rays, deflection in E-M field
α -, β -particle	1899	E. Rutherford (1908)	Natural radioactivity
γ -ray	1900	P. Villard	Natural radioactivity
nucleus	1911	E. Rutherford	α -particle scattering
p	1919	E. Rutherford	Natural radioactivity
n	1932	J. Chadwick (1935)	Natural radioactivity
e^+	1932	C. D. Anderson (1936)	Cosmic rays, cloud chamber
μ^\pm	1937	S. Neddermeyer C. D. Anderson	Cosmic rays, cloud chamber
π^\pm	1947	C. F. Powell (1950)	Cosmic rays, nuclear emulsion
K^\pm	1949	C. F. Powell (1950)	Cosmic rays, cloud chamber
π^0	1950	R. Bjorklund W. K. H. Panofsky	Accelerator
K^0	1951	R. Armenteros	Cosmic rays, cloud chamber
Λ^0	1951	R. Armenteros	Cosmic rays, cloud chamber
Δ	1952	C. D. Anderson	Cosmic rays
Ξ	1952	R. Armenteros	Cosmic rays
Σ^\pm	1953	A. Bonetti	Cosmic rays
\bar{p}	1955	O. Chamberlain (1959) E. Segré (1959)	Accelerators
ν	1955	F. Reines (1995)	Nuclear power plant
Anything else	>1955	Various groups	Accelerators
ν oscillations	1998	Super Kamiokande	Cosmic rays

1.2 The primary cosmic ray flux

The energy spectra and the chemical composition of the primary cosmic ray flux have been extensively investigated for several decades. By convention, the term “cosmic rays” refers to galactic cosmic rays unless otherwise explicitly specified.

1.2.1 Energy spectra of primary cosmic rays

Extensive measurements performed with instruments on board of balloons and satellites showed that the charged primary cosmic ray flux is composed of $\sim 98\%$ nuclei and $\sim 2\%$ electrons and positrons at energies between 10^7 and 10^{12} eV/nucleon. The nuclear component consists of $\sim 87\%$ protons, $\sim 12\%$ helium nuclei, and $\sim 1\%$ heavier nuclei in the energy range $10^8 - 10^{10}$ eV/nucleon where they have the highest flux [30]. Figure 1.1 shows the differential energy spectra of the major components of the primary cosmic radiation obtained from direct measurements and for energies between 10^6 and 10^{12} eV/nucleon.

Below a few GeV/nucleon, the shape of the energy spectrum depends on the phase of the solar cycle. During the periods of high solar activity, the larger and unstable Interplanetary Magnetic Field (IMF) influences the propagation of particles. Therefore, the flux reaches a maximum during phases of low solar activity. This is the well-known phenomenon of the *solar modulation* of the primary cosmic ray flux.

Above 10 GeV/nucleon, the spectra can be well represented by a power law $J_i(E) \propto E^{-\gamma}$, where $J_i(E)$ is the differential flux of nuclear species i with a kinetic energy per nucleon of E and a $\gamma_i = 2.5 - 2.7$. From Figure 1.1 we see that the spectral indices of the three elements with low atomic numbers are nearly identical and steeper than that of Iron nuclei.

At higher energies ($> 10^{14}$ eV), the data are indirectly derived from studies of extensive air showers and normally only the total energy of the primary can be obtained. Figure 1.2 shows a compilation of selected data for energies per nucleus above 10^8 eV. The all-particle energy spectrum roughly follows the same power-law as those of the low energy elements over many orders of magnitude. However, the slope of the spectrum changes from about -2.7 to about -3.0 between 10^{15} eV and 10^{16} eV, and apparently flattens again to -2.5 at several 10^{18} eV. These structures of the spectrum are referred as the *knee* and the *ankle* respectively.

The *knee* region of the cosmic-ray spectrum has been observed with many air shower experiments. Figure 1.3 (from [32]) presents a compilation of results from different experiments in this region. To show the detailed features of the *knee*, a useful practise is to multiply the spectrum by $E^{2.5}$. The actual positions of the *knee* from different experiments and even the same experiment but interpreted with different methods are not in good agreement. A 15% uncertainty in the energy calibration can explain the shift of the *knee* position [32].

The origin of the *knee* is an outstanding problem in cosmic-ray physics and related fields. Currently, it is believed that at least a large fraction of cosmic rays are accelerated in supernova remnants up to energies of $Z \cdot (0.1 - 5) \times 10^{15}$ eV [33]. Higher energies may be provided by other sources. In such mechanisms, the *knee* reflects the cutoff energies for different elements, according to the *leaky box model* for the containment of nuclei inside of the Galaxy. There are many other models attempting to explain the structure. However, none of them can

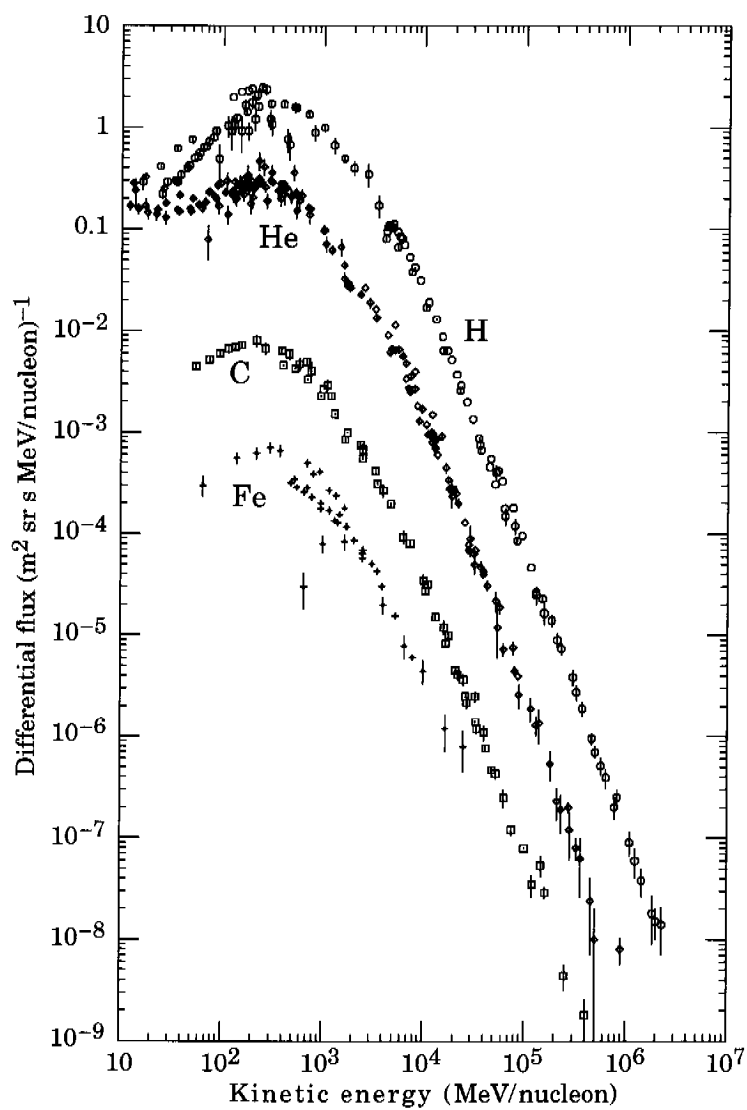


Figure 1.1: The differential energy spectra of the major components of the primary cosmic radiation (reprinted from [30]).

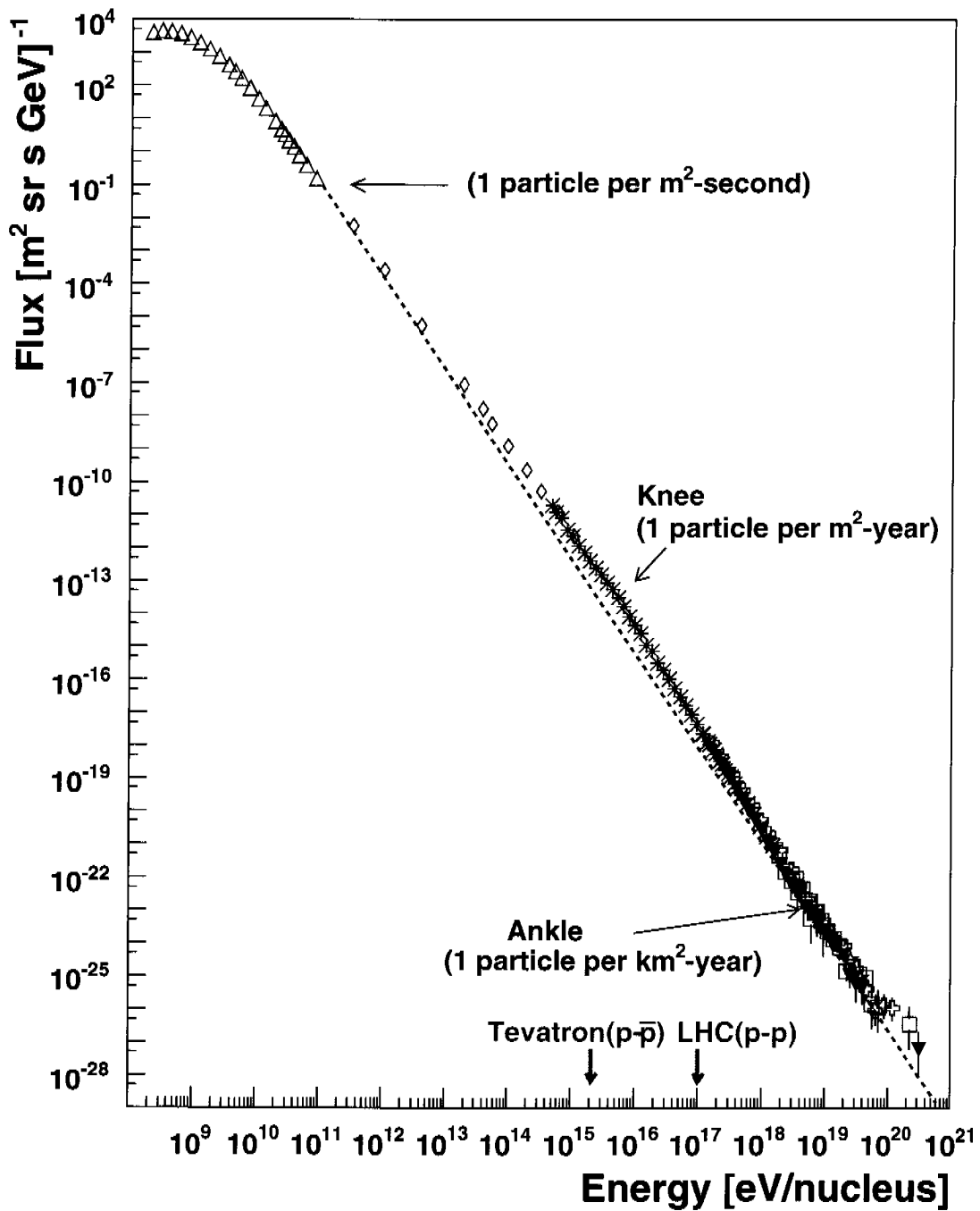


Figure 1.2: The all-particle spectrum of cosmic rays. The dashed line shows an E^{-3} power-law for comparison. The equivalent stationary-target energies of the Tevatron and the LHC are indicated. This plot is a modified version of that from [31].

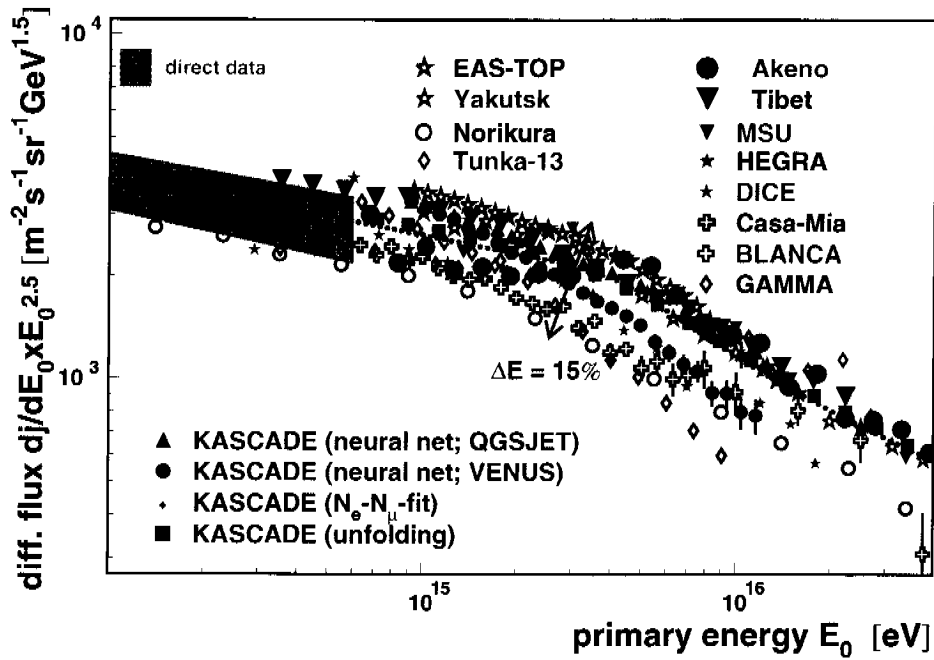


Figure 1.3: Compilation of different experimental results on the cosmic ray all-particle energy spectrum around the *knee* region. The grey band represents direct data measured outside of the Earth atmosphere. The effect of a 15% uncertainty in energy is indicated (see text for explanation). (Reprinted from [32].)

be proved or disproved definitely nowadays. To solve this mystery more measurements are needed, especially the mass composition in this region. The interpretation of the air shower data heavily relies on the hadronic interaction models which had been calibrated with accelerator data at low energies only. Progresses in elementary particle physics with the next generation of accelerators, like the Large Hadron Collider (LHC), which has an equivalent stationary-target energy above the knee region (see Figure 1.2), may boost the understanding on cosmic-ray interactions. The TOTEM experiment [34] at LHC has a capability of measuring forward particles in a pseudorapidity range of $3.1 \leq \eta \leq 6.6$. Another new experiment LHCf [35] to study very forward particles has been approved recently.

Figure 1.4 presents the highest energy portion of the cosmic-ray spectrum. In 1966, Greisen [36], Zatsepin and Kuzmin [37] figured out that the ultrahigh energy cosmic rays, which may originate from outside of our galaxy, could interact with the nowadays well-known 2.7 K microwave background radiation, therefore lose energy before they reach the Earth from cosmological distances. The cosmic ray flux would therefore vanish above a critical energy, referred as the GZK cutoff (a few 10^{19} GeV). The shape of the observed spectrum in this region is still under debate due to low event statistics and difficulties on the energy calibration.

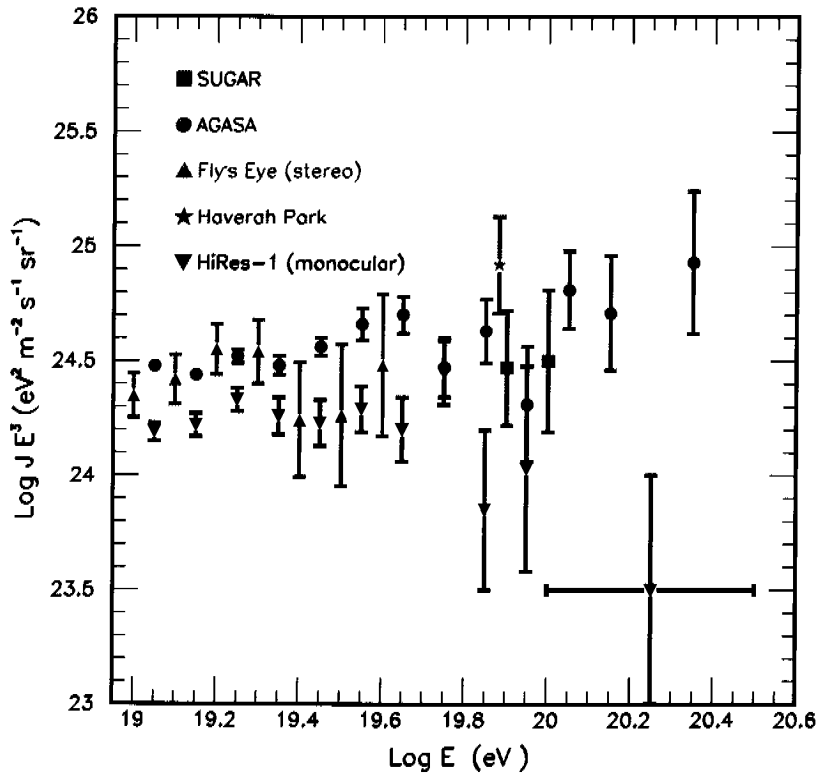


Figure 1.4: Upper end of the cosmic-ray spectrum (reprinted from [38]).

The absence of the GZK cutoff would indicate that the acceleration site must be relatively nearby. However, no candidate source has been found.

1.2.2 The composition of cosmic rays

Precise data on the chemical composition of cosmic rays are only available below 100 TeV, where the elements can be identified through direct measurements performed outside of the atmosphere. Figure 1.5 presents a summary of composition measurements for different energy ranges compared with the Solar system composition. Roughly speaking, they are quite similar, however, significant differences exist.

The odd-even effect, which represents the fact that nuclei with even Z and A are more stable than other combinations, is observed in both, the cosmic-ray and the Solar System composition. In addition, peaks occur simultaneously at C, N, O and Fe. These facts suggest a stellar origin for many of the cosmic rays [39].

The relative abundances of the light elements Li, Be and B in the Solar system are very small because they have low Coulomb barriers and therefore are weakly bound and rapidly consumed in the nuclear reactions. Their comparative abundances in cosmic rays are due to *spallation* of carbon and oxygen nuclei as they traverse the interstellar medium. Similarly,

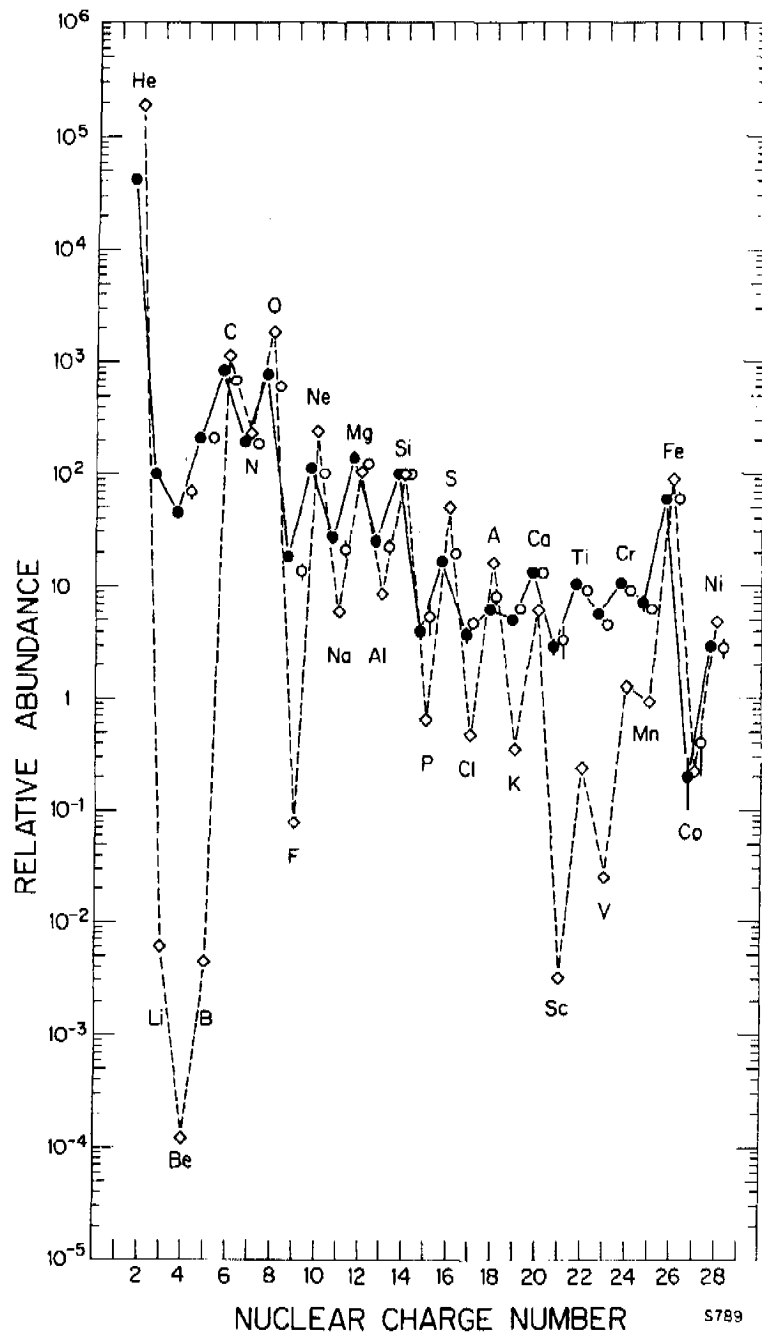


Figure 1.5: The cosmic ray element abundances (He-Ni) measured at Earth compared to the Solar system abundances, all relative to silicon. The solid circles are low energy data (70 – 280 MeV/nucleon), the open circles present a compilation of high energy measurements (1000 – 2000 MeV/nucleon), and the diamonds describe the abundances of the Solar system. (Reprinted from [30])

the abundances of Sc, Ti, V and Mn in cosmic rays are due to *spallation* of the Fe and Ni nuclei.

For higher energies, the composition can only be investigated with indirect method, i.e. from observables of air showers. The derived results are quite problematic.

The composition of cosmic rays (in particular specific isotopes) provides important information of their origin and of the propagation from their source to the Earth.

1.3 Direct measurements

Thanks to the large flux the low energy portion of the cosmic-ray spectrum can be measured with relatively small detectors outside of the Earth atmosphere. Various types of instruments have been conducted on board of scientific balloons as well as satellites orbiting around the Earth or travelling across interplanetary space.

1.3.1 Passive instruments

Nuclear emulsions have been extensively used for studies of primary cosmic-ray spectra and the chemical composition and further development is still under progress now. With this technique an *emulsion chamber* with relative light weight but high positional precision and large acceptance can be build. The simple control and telemetry requirements make this technique ideal for a long duration balloon flight.

Two recent experiments in this category are JACEE [40, 41] and RUNJOB [42, 43]. For example, the JACEE emulsion chamber is a stack of 1) emulsion plates and CR39 plastic for charge determination; 2) fifty thin emulsion plates interleaved with low- Z material as a target to maximise the nuclear interaction probability; 3) a drift space allows gamma rays from neutral pion decays to separate from each other before inducing an electromagnetic cascade; 4) a calorimeter section with lead plates sandwiched with emulsion plates and x-ray films.

Similar to EAS experiments (see next section), the analysis of calorimeter data requires an accurate model of hadronic interactions which still lacks experimental support at high energies.

1.3.2 Active instruments

A modern active instrument consists of a complex of various detectors for energy measurement and particle identification. Some typical detectors used in balloon- and satellite-borne experiments include [44–46]:

Magnetic spectrometer: The track of a charged particle is sampled with position sensitive detectors, e.g. drift chambers, silicon trackers etc, in a magnetic field B . The momentum p measured perpendicular to the magnet field B determines the radius of the track curvature ρ with the relation $p = Ze\rho B$, where Ze is the particle charge. Since the charge number Z needs to be measured with other method, it is convenient to introduce

the so called *magnetic rigidity* $R \equiv pc/Ze$, which is normally measured in GV. The uncertainty of the magnetic rigidity (momentum) is determined by the finite resolution of the tracking detector and the length of the sampled track. The Maximum Detectable Rigidity (MDR) is reached when the relative error is 100%.

Calorimeter: The incident particle is stopped by a high atomic-number material, such as lead, tungsten, etc, where the three-dimensional cascade development is sampled with buried-in sensitive cells or plates. An alternative configuration is to use high-density scintillators like Bismuth-Germanium-Oxyde (BGO) etc, as both absorber and sensitive material. The shower type (hadronic or electromagnetic) can be identified, and the total energy and incident direction of the particle can be reconstructed.

Time-Of-Flight (TOF): A TOF detector normally consists of several fast plastic scintillator plates placed above, below or in between other detectors to: 1) provide the main trigger signal; 2) measure the velocity and incoming direction (up or down) of the particle; 3) determine the particle charge with dE/dx measurements.

Aerogel Cherenkov detector: Silica aerogel is a unique material for threshold-type Cherenkov counters, which is widely used for particle identifications.

Ring Imaging Cherenkov Counter (RICH): In a RICH, particles pass through a radiator, and the radiated photons are usually focused onto a position-sensitive photon detector by a focusing device (mirror) [7]. The velocity β is determined with accuracy up to 0.1% by a measurement of the radius r of the formed ring image, on which the photons are detected.

Transition Radiation Detector (TRD): Transition radiation detectors are used to determine the Lorentz factor γ and for the identification of highly relativistic particles when a Cherenkov counter is not applicable.

Anticoincidence detector: To reduce background, particles not passing through the acceptance window can be actively rejected with signals from plastic scintillators which surround the detector system.

1.3.3 New experiments

Table 1.2 summarises the main characteristics of three new space-borne instruments. The BESS-Polar [46] had been flown above the Antarctica in Dec. 2004. PAMELA [44] and AMS-02 [45] are scheduled to be launched end 2005 and in 2008 respectively for missions lasting for at least three years.

1.4 Indirect measurements

For many practical reasons, space-borne detectors can not have sufficient sensitive volume to detect cosmic rays with energies above about 10^{14} eV. Fortunately, one can use the Earth

Table 1.2: Properties of next generations of magnetic spectrometers (adapted from [16]).

	MDR (TV)	Exposure (days)	Aperture (cm ² sr) ⁻¹	Sensitivity/ # of events	Range (GeV/n)
BESS Polar [46] (2004-2007)	0.2	10 + 20	3000		
			p	3×10^9	0.2 – 200
			\bar{p}	3×10^4	0.1 – 4.2
			He	4×10^7	0.2 – 200
			\bar{D}/D	10^{-5}	0.1 – 0.7
			\bar{He}/He	3×10^{-8}	
Pamela [44] (2005-2008)	0.74	1000	20.5		
			p	3×10^8	0.08 – 700
			\bar{p}	3×10^4	0.08 – 190
			e ⁻	6×10^6	0.05 – 2000
			e ⁺	3×10^5	0.05 – 270
			He – C		up to 700
			\bar{He}/He	10^{-7}	up to 30
AMS-02 [45] (2008-2011)	2.5	1000	5000		
			p	2×10^{10}	0.5 – 2500
			\bar{p}	3×10^6	0.5 – 400
			e ⁻	6×10^8	0.5 – 5000
			e ⁺	3×10^7	1.0 – 400
			He – Fe		0.5 – 1400
			γ		2.0 – 300
			\bar{D}/D	3×10^{-7}	
			\bar{He}/He	10^{-9}	

atmosphere as a calorimeter to measure the total energy of an incident cosmic-ray particle.

1.4.1 The atmosphere

The Earth atmosphere consists of a mixture of gases, primarily nitrogen, oxygen and argon with volume fractions of 78.1%, 20.9% and 0.9%, and many less abundant elements [47]. For a rough estimation, ignoring the temperature dependence on altitude, the density of the atmosphere can be approximated by a simple exponential function $\rho(h) \approx \rho_0 e^{-h/h_0}$ (with uncertainties amount to 30% over the range of 0 – 100 km), where h is the altitude above sea level, $\rho_0 = 1.225 \text{ kg/m}^3$, and $h_0 \approx 8.4 \text{ km}$ is known as the scale-height of the atmosphere [48].

To describe the air shower development, the more relevant quantity is the vertical atmospheric depth $X_{\text{vertical}}(h) = \int_h^{\infty} \rho(z) dz = \rho_0 h_0 e^{-h/h_0}$. Generally, the total amount of the air medium traversed by the shower, the *slant depth* at zenith angle θ , is $X(h, \theta) = X_{\text{vertical}}(h) / \cos \theta$ for $\theta < 70^\circ$ where the curvature of the Earth can be safely ignored.

Many atmosphere models have been developed to describe the altitude dependence of the atmospheric density or even its very complicated time dependence. In the well-known air shower simulation program CORSIKA (see Section 1.4.4) the U.S. standard atmosphere (1976) [47] is approximated with five layers, in which the densities of the first four layers from sea level exponentially depend on the altitudes, while the highest layer has a linear density function.

1.4.2 Air shower development

When a cosmic ray hits a molecule in the upper atmosphere a jet of hadrons (pions, kaons, nucleons and nuclear fragments) is created through nucleus-nucleus interactions. The neutral pions ($\tau = 8.4 \times 10^{-17} \text{ s}$) immediately decay into photons. Each high energy photon initiates an electromagnetic sub-shower through alternated pair production and bremsstrahlung processes. Nucleons and other high energy hadrons in the jet continue to interact with the atmosphere through a hadronic cascade which results in a core, the hadronic air shower component. At each hadronic interaction, slightly more than 1/3 of the energy contributes to the electromagnetic component [2]. Charged pions and kaons with relatively low energies may decay into muons and neutrinos before interacting. The decay probability of energetic hadrons in the first few generations is rather small.

Figure 1.6 sketches the cascade process of the air shower development. As the shower develops, the secondary particles form a curved thin layer called the *shower front*.

The electromagnetic component

The electromagnetic processes have been well understood within the quantum electrodynamics (QED). The most general properties of the electromagnetic cascade can be described with a very simple model developed by Heitler, Bhabha and Oppenheimer. Only processes of pair production and bremsstrahlung are considered in this model. In each step, one particle is converted to two new ones with equal energies. Therefore, the number of particles N grows

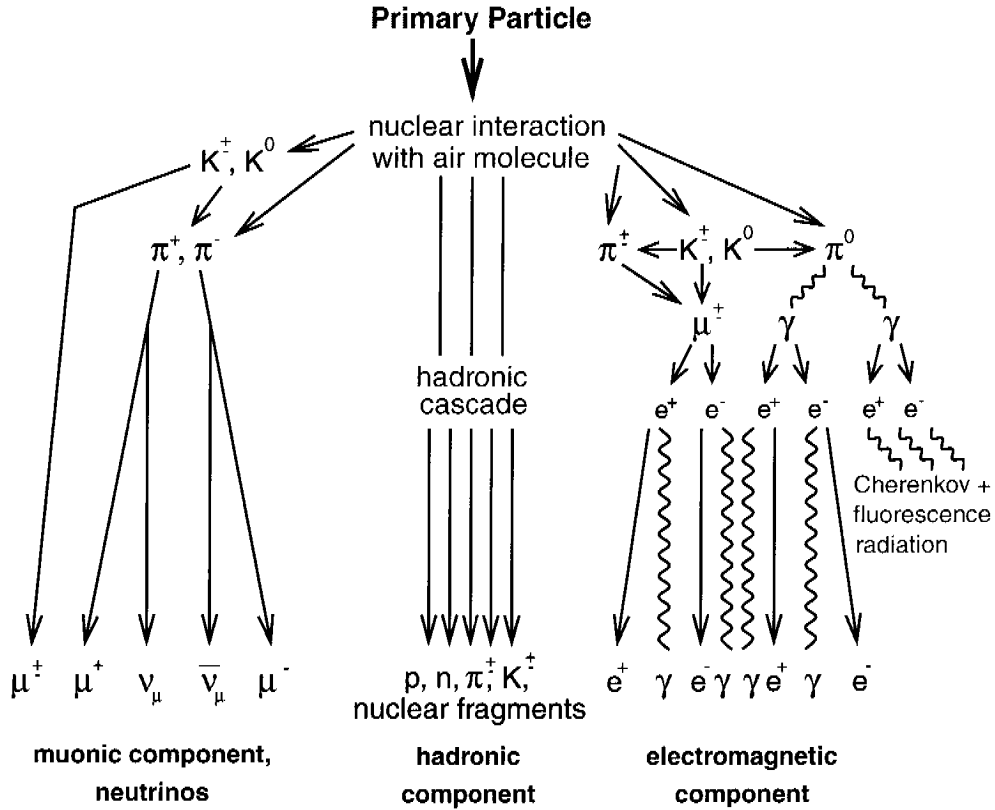


Figure 1.6: A schematic view of the air shower development (reprinted from [49]).

geometrically to $N \approx 2^{X/X_0}$ at an atmospheric depth X , where $X_0 = 36.7\text{g/cm}^2$ is the radiation length. When the energies of the cascade products $E(X) = E_0/N$ decrease down to the *critical energy* $E_c \approx 86\text{ MeV}$ (defined as the energy where $\frac{dE}{dx}|_{\text{radiation}} = \frac{dE}{dx}|_{\text{ionisation}}$), the number of particles approaches the maximum value at

$$X_{\text{max}} = X_0 \frac{\ln(E_0/E_c)}{\ln 2},$$

where E_0 is the energy of the first gamma photon. Below E_c the energy is mainly lost through ionisation. We can conclude that X_{max} is logarithmically proportional to the primary energy, while N_{max} depends linearly. A more elaborate simulation indicates that this simple estimation roughly lies within the uncertainties due to the Landau-Pomeranchuk-Migdal (LPM) effect, which suppresses the cross sections for pair production and bremsstrahlung above about 10^{10} GeV , and the geomagnetic effects [48].

The relation between the total number of electrons and positrons and the primary energy is given by the Greisen formula,

$$N_e(E_0, X) = \frac{0.31}{[\ln(E_0/E_c)]^{0.5}} \exp\left[\frac{X}{X_0}\left(1 - \frac{3}{2} \ln s\right)\right],$$

where $s = 3 \left[1 + \frac{2 \ln(E_0/E_c)}{X/X_0} \right]^{-1}$ is the so-called *age parameter*.

The lateral distribution of the electromagnetic component in the shower front is dominated by multiple Coulomb scattering, while a small fraction contributes via the opening angles in pair production and bremsstrahlung. The Molière radius r_M , which determines the transverse development due to Coulomb scattering, is

$$r_M = X_0 E_s / E_c \approx 9.3 \text{ g/cm}^2,$$

where $E_s = \sqrt{4\pi/\alpha} m_e c^2 \approx 21 \text{ MeV}$ is the scale energy. On average, about 90% of the energy lies inside a cylinder with radius r_M , and 99% inside of $3.5 r_M$ [50].

The three-dimensional electromagnetic cascade distribution can be approximated by the well-known NKG (Nishimura-Kamata-Greisen) formula. The number density $\rho(r)$ is given by

$$\rho(r) = C \frac{N_e}{r_M^2} \left(\frac{r}{r_M} \right)^{s-2} \left(1 + \frac{r}{r_M} \right)^{s-4.5}, \quad (1.1)$$

where N_e is the total number of electrons, r is the distance from the shower axis, and $C = \frac{\Gamma(4.5-s)}{2\pi\Gamma(s)\Gamma(4.5-2s)}$ is a constant determined from the normalisation $2\pi \int_0^\infty r \rho(r) dr = N_e$.

The muon component

Most muons in air showers are produced through the decay of charged pions (kaons),

$$\pi^+ (\text{K}^+) \rightarrow \mu^+ + \nu_\mu,$$

$$\pi^- (\text{K}^-) \rightarrow \mu^- + \bar{\nu}_\mu.$$

At high energies ($> 10^{14} \text{ eV}$) also D-meson decays contribute.

According to QED theory, the direct $\mu^+\mu^-$ pair production (resulting from gammas from π^0 decays or from hard bremsstrahlung) is suppressed by a factor $(m_e/m_\mu)^2$ compared to the e^+e^- production. Therefore, this process normally can be ignored in baryon induced air showers.

Since there is no “muonic cascade”, the number of muons produced in the air shower is much smaller than the number of electrons. At sea level, the air shower is dominated by the electromagnetic component up to zenith angles $\theta \lesssim 70^\circ$. Beyond that, the number of electrons and photons decreases significantly due to the absorption in the thick atmosphere.

Besides the continuous *ionisation*, muons may lose energy through *bremsstrahlung*, *muon-nucleus* interaction, direct *pair* (e^+e^-) *production*, and *knock-on* electrons (δ -rays) production [51]. The cross section for individual interaction is represented by the mean free path in Figure 1.7. Above a TeV, the muon energy loss is dominated by the electron pair production which is illustrated in Figure 1.8. The knock-on production has a short mean free path, and thus can be considered as a continuous process. However, because of the very small inelasticity, its contribution to the energy loss is comparable to that from hard processes [48].

Consequently, due to the relatively long life time ($\tau_\mu \approx 2.2 \mu\text{s}$) and the small interaction cross sections, the number of muons decreases slowly when the air shower approaches the ground level. High energy muons can even penetrate deep underground.

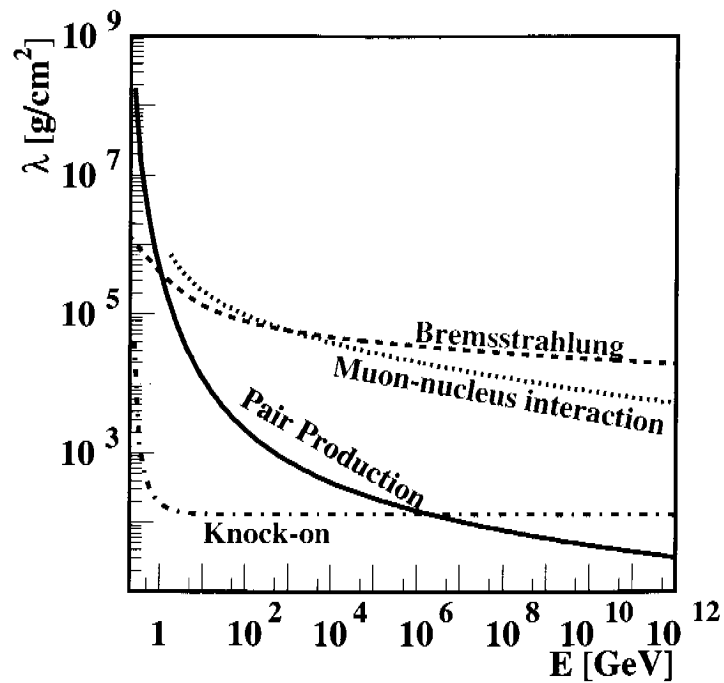


Figure 1.7: Mean free path λ in air for different muonic interactions as a function of the initial kinetic energy (reprinted from [52]).

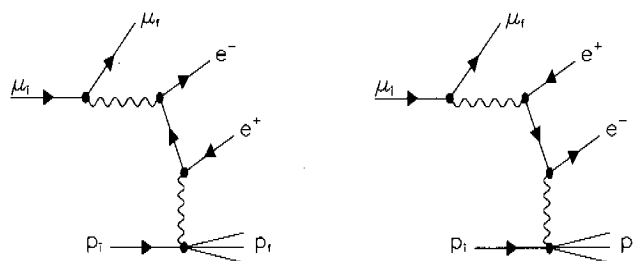


Figure 1.8: Feynman diagrams for pair production of muon interactions with nuclei (reprinted from [53]).

Because high energy muons are only little affected by multiple Coulomb scattering, their lateral distribution at sea level is determined mainly by their transverse momenta inherited in the hadronic interactions and the decay process of charged pions (kaons). The lateral distribution function has been investigated extensively in literatures. The classical treatment due to Greisen [54] is still widely used [2, 48]. In this model, the lateral density distribution of muons is expressed in an NKG-like form,

$$\rho_{\mu}(r) = \frac{\Gamma(2.5)}{2\pi\Gamma(1.5)\Gamma(1.5)} \left(\frac{1}{r_G}\right)^{0.5} \left(\frac{r}{r_G}\right)^{-0.75} \left(1 + \frac{r}{r_G}\right)^{-2.5},$$

where $r_G = 320$ m is analogous to the Molière radius.

1.4.3 Observation techniques

A typical air shower induced by a high energetic cosmic-ray particle spreads over a large distance up to several kilometers. The properties of the primary particle, i.e. the total energy, incident direction and composition can be estimated through sampling few or all types of the secondary particles with an array of detectors. The Cherenkov light, fluorescence light and radio emission produced during the shower development supply additional information, e.g. for the determination of the primary energy.

Extensive air shower arrays

The shower front is sampled with an array of small detectors ($1 - 10$ m²) spread over a large area ($10^4 - 10^9$ m²) on ground or on top of a mountain. A classical scintillator array samples the electromagnetic component which is referred as N_e (for example, HEGRA, Tibet AS γ , and the L3+C scintillator array), or the total number of charged particles N_{ch} (for example, KASCADE and AGASA). AGASA is presently the largest of this type covering an area of 100 km².

An array of water Cherenkov detectors can measure N_e and N_{μ} separately. For example, the surface detector of the Auger Observatory consists of 1600 water-tanks covering an area of 3000 km² in Argentina. Data taking has been started with 750 of them since January 2004. An array of the same size is planned to be built in America for a full-sky coverage [55].

RPCs (Resistive Plate Counters) displayed as a large “carpet” have also been used for the measurement of N_{ch} of air showers in Tibet [56].

The sampled particle density is fitted to a lateral distribution to estimate the total energy of the primary cosmic ray. The incident direction is determined with the arrival time of the shower front, measured over the whole detector area.

Muon tracking detectors

Tracking detectors allow for an improved muon identification and a direct measurement of the muon direction. Ignoring the marginal effects of multiple Coulomb scattering, the muon

production height can be determined from the relative muon direction with respect to the shower axis [49]. An example is the muon tracking detector of the KASCADE experiment.

Deep underground muon detectors like MACRO and SOUDAN detected very high energy muons which are most likely generated in the first interactions of the air shower and therefore carry information about the primary cosmic ray [49].

In contrast to other muon tracking detectors, L3+C was located at a shallow depth (30 m underground in the LEP ring at CERN) and employed a high precision muon chamber system in a large volume magnetic field. Therefore, the muon momentum could be determined with high accuracy (see Chapter 3 and Ref. [57, 58]).

Cherenkov light observation

High-energy charged particles emit Cherenkov radiation when travelling in a medium with speed larger than that of light in the same medium. Cherenkov light photons are generated throughout the cascade development and are strongly forward peaked. It provides a possibility of estimating the total energy of the shower and of spying the shower development with “Cherenkov telescopes” on ground. Examples are Whipple, Cangaroo, MAGIC, H.E.S.S., etc.

Fluorescence light observation

The N_2 molecules in the atmosphere can be excited by ionising particles and emit fluorescence photons between 3000 and 4000Å. The emission is isotropic and therefore can be measured far away from the shower axis. Examples are Fly’s Eye, Hires Fly’s Eye, and the fluorescence telescopes of the Auger observatory. In addition, the EUSO, a space-borne 2.5 m telescope which can observe the fluorescence light over a very large area from above the atmosphere, has been proposed [59].

Radio emission

The mechanism of the radio emission produced in cosmic-ray air showers was not well understood for a long time since it was discovered [60] over 30 years ago. In a new approach, the pulsed radio signal is interpreted as *coherent geosynchrotron radiation* [61, 62]: secondary electrons and positrons are deflected and separated by the Earth’s magnetic field and therefore produce dipole radiation. The coherence effect due to the thin shower front (comparing to the wavelength of the radio emission) significantly amplifies the signal. Radio emissions from very high energy cosmic rays can provide calorimetric and high precision directional measurements with relative low cost antenna arrays and digital electronics. One of the advantages of this technique is the high duty cycle compared to the typical duty cycle of 10% of the fluorescence light observation (due to atmospheric conditions and day/night).

1.4.4 Air shower simulations

CORSIKA (COsmic Ray SIMulation for KAScade) [63–65] is a program for detailed simulation of extensive air showers initiated by high energy cosmic ray particles. It has become a standard for general usage, though it was designed for the KASCADE experiment at the beginning.

The simulation framework includes a description of the Earth atmosphere, electromagnetic interactions, particle transport in the atmosphere (effect of multiple scattering and Earth magnetic field) and interfaces to hadronic interaction models. All decay branches down to the 1% level are taken into account in particle decays.

The characteristic of the hadronic interactions involved in the extensive air shower development is the low momentum transfer known as “soft” hadronic interactions. Several models based on the Gribov-Regge theory of multi-Pomeron exchange can be chosen for hadronic interaction description at high energies (> 80 GeV): the QGSJET (Quark-Gluon String model with JETs) [66, 67], the VENUS model for Very Energetic Nuclear Scattering [68], the DP-MJET (Dual Parton Model) [69], and the neXus [70]. The minijet model SIBYLL [71] is also implemented in CORSIKA. A pure phenomenological Monte Carlo (M. C.) generator HDPM [72] is also provided. Large uncertainties exist presently due to the lack of accelerator data at the cosmic-ray energies and the very forward region. (A comparison of the models is available from [73].)

On the other hand for hadronic interactions at low energies, the FLUKA¹ code can be used. Alternative choices are the very slow ultra relativistic quantum molecular dynamics program UrQMD, and the GHEISHA interaction routines which is now considered out-of-date.

The electromagnetic interactions are described by the shower program EGS4 or the analytical NKG formulae.

An alternative code for more or less the same purpose is the AIRES (AIRshower Extended Simulations) [75]. In addition, the TARGET 2.2 transport code [76] can be used for muon and neutrino fluxes prediction.

1.5 Astrophysics and astronomy with cosmic rays

According to the *Encyclopædia Britannica* [77], astronomy is the science that deals with the origin, evolution, composition, distance, and motion of all bodies and scattered matter in the universe. It includes astrophysics, which discusses the physical properties, the interactions, and structure of all cosmic matter.

Before 1945, optical telescopes were the sole instruments for astronomical observations. Hereafter, thanks to the new experimental techniques and the space technology, new disciplines of radio, millimetre, infrared, ultraviolet, X- and γ -ray astronomies have been carried

¹The standalone FLUKA [74] is a generic M. C. simulation package for particle physics and related fields capable of handling hadronic and electromagnetic interactions and particle transport in any material over a wide energy range. It is only used to describe low-energy hadronic interaction in CORSIKA.

out. Therefore, we can explore the universe at all electromagnetic wavelengths deep into space and time. In addition, charged cosmic rays and neutrinos are also important messengers of astronomical objects and interstellar media. With particle detectors, which have already been used in X- and γ -ray astronomies, various topics in astronomy and astrophysics can be studied with cosmic rays. Some hot topics in this new interdisciplinary area are:

- Origin of ultrahigh energy cosmic rays.
- Antimatter in space.
- Dark matter search.
- Neutrino astronomy.

1.6 Summary

Cosmic rays provide a unique opportunity for elementary particle physics, astrophysics and cosmological studies. The origin of high energy cosmic rays, and several other fundamental questions are still under investigation.

Chapter 2

Antiprotons in space

The first antimatter particle, the positron, was discovered in cosmic rays in 1932. Later it was realised that positrons observed at ground level are purely secondary products of air showers induced by high energy cosmic rays. Antiproton, the second antiparticle with long life time was discovered at the Berkeley Bevatron in 1955 [78]. Antimatter is a fascinating topic in many research fields and is also one of the most attractive words in science fictions.

The most frequently asked question concerning antimatter is: “*is the universe symmetric with respect to matter and antimatter?*” This long-standing fundamental question was first argued by Dirac when he predicted the existence of a positively charged electron.

“If we accept the view of complete symmetry between positive and negative electric charge so far as concerns the fundamental laws of Nature, we must regard it rather as an accident that the Earth (and presumably the whole Solar system), contains a preponderance of negative electrons and positive protons. It is quite possible that for some of the stars it is the other way about, these stars being built up mainly of positrons and negative protons. In fact, there may be half the stars of each kind. The two kinds of stars would both show exactly the same spectra, and there would be no way of distinguishing them by present astronomical methods.” (P. A. M. Dirac, Nobel Lecture, 1933)

Extensive observations have confirmed that antimatter (antiprotons and positrons) exists in the primary cosmic ray flux measured near the Earth, however at a very low flux level. Studies on the production mechanisms, the propagation from their source to the Earth, and the existence of heavier antinuclei may eventually answer the exciting questions and provide a further understanding on various astrophysical and cosmological topics, such as the origin of the Universe, the existence of dark matter, etc.

This chapter contains a general discussion on the puzzle of the baryon asymmetry of the Universe, as well as observations and theoretical interpretations about the presence of antiprotons in the cosmic ray flux.

2.1 Antimatter in the Universe

According to the present cosmological model, the Universe is believed to have originated from a singularity in an explosion called the “Big Bang”. Symmetry between matter and antimatter should have existed if this explosion was initiated by a fluctuation of the vacuum. But the present known part of the world consists of matter only. In 1967 Sakharov established three necessary conditions for the evolution of the universe in order to arrive at this asymmetric situation [79]:

1. An epoch must have existed during which no thermodynamical equilibrium governed the interactions of particles and radiation.
2. Some CP violating reactions must exist.
3. The conservation of the baryon number should be violated in some elementary reactions.

The two first conditions may indeed have been fulfilled, since non thermodynamical conditions may very well have reigned during the expansion and cooling of the early universe, and CP violating reactions are known to exist (in the $\bar{K}^0 K^0$ and $\bar{B}^0 B^0$ systems). The third point is not yet established, since the baryon number violating process predicted by many grand unification theories (GUTs), like for instance the proton decay, has not been observed. Along these line one can e.g. mention the proposed heavy GUT Leptoquarks (X, Y) and Anti-Leptoquarks (\bar{X}, \bar{Y}): At early times ($t \approx 10^{-35}$ s) X and \bar{X} were being produced or annihilated in thermal equilibrium. At a later time these particles started to decay to quarks and leptons. The probability for certain decay channels being slightly different, due to the CP violation, results in a slightly different number of quarks and antiquarks:

$$\Gamma(X \rightarrow q\bar{l}) \leq \Gamma(\bar{X} \rightarrow q\bar{l}) \quad \text{and} \quad \Gamma(X \rightarrow q\bar{l}) > \Gamma(\bar{X} \rightarrow \bar{q}q)$$

As the Universe further cooled down with the expansion, quarks/anti-quarks and leptons/anti-lepton annihilated to photons, and only a small number of quarks and leptons remained to create ordinary matter [80].

However, the origin of the baryon asymmetry is still one of the fundamental questions in modern cosmology. To completely solve this problem precise observations are essential. Basically, there are two experimental categories:

Indirect evidence: If antimatter exists in the Universe, it may find a way to meet ordinary matter. The main products of a nucleon-antinucleon annihilation are pions (exactly equal numbers of π^\pm and approximately equal numbers of π^0). A typical interaction-decay scheme is [81]

$$N + \bar{N} \rightarrow \begin{cases} \pi^0 \rightarrow \gamma + \gamma \\ \pi^\pm \rightarrow \mu^\pm + \nu_\mu(\bar{\nu}_\mu); \quad \mu^\pm \rightarrow e^\pm + \nu_e(\bar{\nu}_e) + \nu_\mu(\bar{\nu}_\mu) \end{cases}$$

All the final products of an annihilation at rest have very similar spectra, extending from several tens of MeV to several hundred MeV with average energies between 100 MeV and 200 MeV. Due to deflections in the magnetic field and high background, the positron component of the primary flux at top of the atmosphere cannot be used for observing a far distant region, where antimatter exists, while the 0.51 MeV Gamma line may hint to a region where matter-antimatter annihilation exists. The use of ν_e is also not easy, because low-energy ($\lesssim 1$ GeV) ν_e detectors have difficulties to provide directional information. The γ -ray component is the most useful probe for this purpose, while ν_μ also eventually provides useful information [81].

Direct search: The detection of a single antihelium nucleus can almost confirm the existence of an antimatter source, because such a nucleus is not likely to be produced by ordinary cosmic rays interacting with interstellar matter. Despite extensive searches, no antinucleus with atomic number $A \geq 2$ has been observed till now [82, 83].

But antiprotons have been observed in the cosmic ray flux. However, current data at low energies (< 50 GeV) are in agreement with a secondary production through the interaction $p + p \rightarrow 3p + \bar{p}$ and other similar reactions. Furthermore, antiprotons can be produced by various exotic sources. This topic will be discussed in the following sections.

While electrons and positrons are produced at known sources and deliver information through the synchrotron radiation and inverse Compton scattering about the conditions near the source, they can not travel through interstellar medium without losing energy and directional information. Therefore, primary electron and positron observations can not answer questions related to sources at cosmological distances.

2.2 Antiprotons in cosmic rays: Investigations

Conventionally, a ratio of antiproton to proton flux is reported. In this way various theoretical and experimental systematic uncertainties can be ignored: 1) the normalisation uncertainty of the proton flux; 2) the uncertainty of the detector acceptance; 3) the uncertainty due to the solar modulation [84].

2.2.1 Direct measurement

Various techniques for direct cosmic ray measurements have been described in Section 1.3. Table 2.1 summarises some direct antiproton observations of the last 30 years.

Cosmic-ray antiprotons were first searched for in nuclear emulsions exposed in balloon flights from the 1960s to the early 1980s. No candidate had been found with this technique [107].

The first antiproton events (in the kinetic energy range 4.7 – 11.3 GeV) in cosmic rays were observed by Golden *et al.* with a balloon-borne magnetic spectrometer [85, 86] in 1979. One year later, Buffington *et al.* made a successful observation with a low energy calorimeter

Table 2.1: Summary of past cosmic-ray antiproton experiments. Each experiment consisted of a magnetic spectrometer, a TOF system and other subdetectors (if applicable) listed below.

Experiment	Flight date	Technique (Besides spectrometer and TOF)	E_{kin} [GeV]	# of \bar{p} 's
Golden <i>et al.</i> [85, 86]	1979	gas Č, CAL	4.4 – 13.4	41.5
Buffington <i>et al.</i> [87]	1980	plastic Č, image CAL	0.13 – 0.32	14
LEAP [88]	1987	-	0.12 – 0.36	0
PBAR [89, 90]	1987	-	0.1 – 1.58	0
MASS91 [91, 92]	1991	gas Č, image CAL	3.70 – 24	23.6
IMAX [93]	1992	aerogel Č	0.25 – 3.2	16
BESS [94, 95]	1993	-	0.2 – 0.6	6
CAPRICE [96]	1994	RICH, image CAL	0.6 – 3.2	9
BESS [97]	1995	-	0.175 – 1.4	43
BESS [98]	1997	aerogel Č	0.175 – 3.5	415
BESS [99]	1998	aerogel Č	0.175 – 4.2	384
CAPRICE2 [100, 101]	1998	RICH, image CAL	3 – 49	31
AMS-01 [102]	1998	TRD, aerogel Č	0.1 – 5	122
BESS [103]	1999, 2000	aerogel Č	0.18 – 4.2	1226
HEATE-pbar [104]	2000	-	4 – 50	78
BESS-TeV [105]	2002	aerogel Č	0.18 – 4.2	147
BESS-Polar [106]	2004	aerogel Č	0.1 – 4.2	TBD

(0.13 – 0.32 GeV) also at the top of the atmosphere [87]. However, various uncertainties put this low energy measurement in doubt [107]. The other two low energy experiments LEAP [88] and PBAR [89, 90] performed in 1987 did not detect antiprotons. The upper limits on the antiproton flux derived from these two experiments contradicted the previous ones.

Since the 1990s, the application of improved magnetic spectrometers, with qualities comparable to accelerator experiments, made more data available and extended the kinetic energy range up to 50 GeV. The key parameters of these experiments are tabulated in Table. 2.1.

With the next generation of space-borne magnetic spectrometers (see Section 1.3), the antiproton spectrum may be explored up to about 400 GeV.

2.2.2 An “indirect” measurement

As mentioned in Section 1.4, high energy cosmic rays can only be detected through EAS. In the present work, the ratio of antiprotons to protons is estimated from the shadowing of cosmic rays by the Moon. The Earth-Moon system is used as a magnetic spectrometer, and the Earth atmosphere as part of the detector. The method and the results are discussed in Chapter 6.

2.2.3 Estimation of the \bar{p}/p ratio from the muon charge ratio

The muon charge ratio at sea level reflects the mass composition and the charge sign of the primary cosmic rays. The ratio of μ^+ to μ^- has been measured by many experiments from a few GeV to a few TeV. The average charge ratio for vertical incident muons between 20 and 500 GeV, measured by the L3+C experiment is $1.285 \pm 0.003(\text{stat.}) \pm 0.019(\text{syst.})$ [58]. This value mainly corresponds to primary protons and helium nuclei. The μ^+/μ^- charge ratio induced by primary antiprotons (and antihelium) is expected to have an inversed value of $\sim 1/1.3$. Therefore, the fraction of the antiprotons in the primary cosmic ray flux can be derived from a comparison between data and calculations.

This has been examined in [108]. The derived upper limits (at 67% confidence level, but with large systematic uncertainties) for the \bar{p}/p ratio are 7%, 17%, 10% and 14% respectively for the energy ranges 0.1 to 0.2 TeV, 1.0 to 1.5 TeV, 10 to 15 TeV, and > 30 TeV. Large uncertainties are unavoidable even with nowadays more precise measurements of the μ^+/μ^- value. The uncertainties are due to the difficult cascade calculations: 1) the input primary composition is quite uncertain at high energies; 2) the high energy hadronic interactions are not well known. At present, all the hadronic models even failed to reproduce correctly the muon spectrum measured by the L3+C experiment [109] and the Cosmo-ALEPH experiment [110].

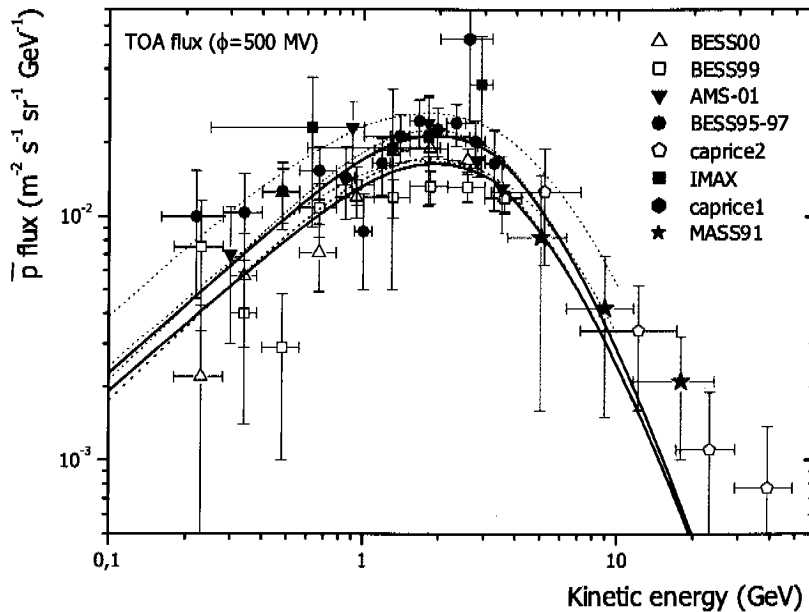
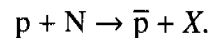


Figure 2.1: Modulated antiproton flux at the top of the atmosphere (reprinted from [115]). The solid (dashed) lines correspond to the single $p p \rightarrow \bar{p} X$ without (with) the NAR contribution [115]. Dotted lines represent calculations with the DTUNUC program [113]. (See Table 2.1 for references of the experiments.)

2.3 Antiprotons in cosmic rays: Interpretations

The antiproton flux from direct measurements can be well explained as being composed by secondaries produced in interactions of cosmic rays with the interstellar medium. This process is dominated by cosmic-ray protons colliding with interstellar atoms [111, 112],



Due to baryon number conservation, at least three other nucleons should be produced as well, and therefore the energy threshold of this process is $7m_p$. This determines the spectrum of secondary antiprotons peaking at about 2 GeV and decreasing sharply toward lower energies. This is a unique characteristic, distinguishing it from other cosmic-ray elements [113]. In the low energy region, large uncertainties exist in predictions due to the complexity of production and propagation. At high energies, the secondary flux can be predicted precisely. Current models agree well with each other. But some uncertainties can be attributed to [114]: 1) different models of the cosmic-ray spectrum at the production site; 2) propagation of cosmic rays in the Galaxy; 3) incomplete knowledge of the interaction and the scattering of high energy particles; 4) solar modulation. Figure 2.1 presents the antiproton flux at the top of the atmosphere (TOA) as measured by experiments since 1990 and compared with the predicted secondary antiproton fluxes from two recent calculations.

In addition to secondary production and to a potential extra-Galactic origin, there are two

other possible (exotic) sources of primary antiprotons to be mentioned:

- Neutralino annihilations, a possible signature of dark matter. Equal amounts of matter and antimatter is produced in Neutralino annihilations. In some scenarios, such as a clumpy halo distribution of dark matter [116], these annihilations can provide a \bar{p}/p ratio up to the % level in the TeV range [112, 117]. This fact represents the main physics motivation of the present work!
- Evaporation of Primordial Black Holes (PBH). Small black holes could have formed in the early universe and should still continue to evaporate and produce all kinds of particles. However, the predicted antiproton flux at high energies is much too low [118] to be observed by L3+C within the two years of data taking and its acceptance.

2.4 Previous L3+C result and the present work

The L3+C collaboration has performed and published an antiproton search using the Moon shadow method [119, 120]. My main contribution to this first analysis was on the angular resolution determination and the M.C. simulation with CORSIKA [117, 121].

No evidence was found of antiprotons around 1 TeV and an upper limit of the antiproton to proton ratio of 0.11 (90% C.L.) was set. Figure 2.2 shows the first result and compares the L3+C result to direct measurements from other “low” energy experiments. In this analysis however, only 1/3 of the collected data, which were considered to have better quality than the rest, were used. Since the statistics is very critical, an independent analysis has been undertaken in this present work, with the whole data set as well as with a lower muon momentum threshold.

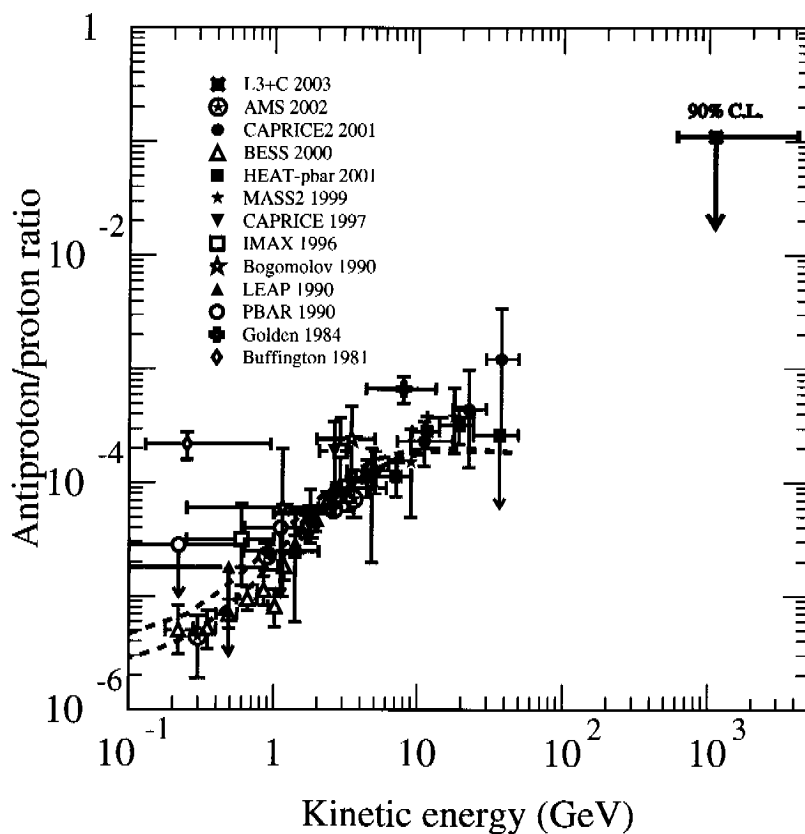


Figure 2.2: Measurements of the ratio of the antiproton and proton fluxes as function of the nucleon energy, including the previous L3+C limit around 1 TeV [120]. The dashed lines show the theoretical expectations [114].

Chapter 3

The L3+C experiment

L3 [122] was one of the four large detectors installed at the Large Electron Positron collider (LEP) at CERN, Geneva, which was designed to perform precision measurements of electrons, photons, hadrons and muons produced in electron positron collisions at centre-of-mass energies up to 209 GeV.

Like all other ground level or under ground particle detectors, the L3 detector was exposed to the cosmic muon flux during its entire life time. Cosmic ray events were of no interest for accelerator particle physics studies, except for detector calibrations, and were efficiently rejected by the tight time window of the beam crossing signal and by a requested particular track pattern. However, these “background” events could also well be collected, thanks to a different trigger, to study various topics on astroparticle physics [123–125].

The cosmic ray version of L3, the L3+C experiment (proposed in 1987) came into operation just two years before the LEP shutdown in November 2000.

During the yearly LEP maintenance time between 1997 and 1998, some additional detectors and an independent data acquisition (DAQ) system were installed (phase I). Data collected during 1998 were only used for detector performance studies and optimisations [126]. Just before LEP started the physics run again in April 1999, L3+C was able to upgrade to phase II and start to collect cosmic muons with the fully integrated DAQ system.

The experimental setup of the L3+C experiment, as well as the event reconstruction and the simulation principle will be described in this chapter. A short list of different physics topics will also be included.

3.1 Location and environment

The L3+C detector was located near Geneva airport at the foot of the Jura Mountains. The longitude and latitude were $6^{\circ}01'17''$ E and $46^{\circ}15'06''$ N, respectively. The surface altitude was 449 m above sea level. Figure 3.1 shows the location of L3 as well as other detectors at LEP. The L3 coordinate system is also indicated in this figure. The L3 axis (z -direction) is inclined by 1.39% with respect to the ground level.

The L3 detector was installed 51 m underground, covered by molasse with a minimum

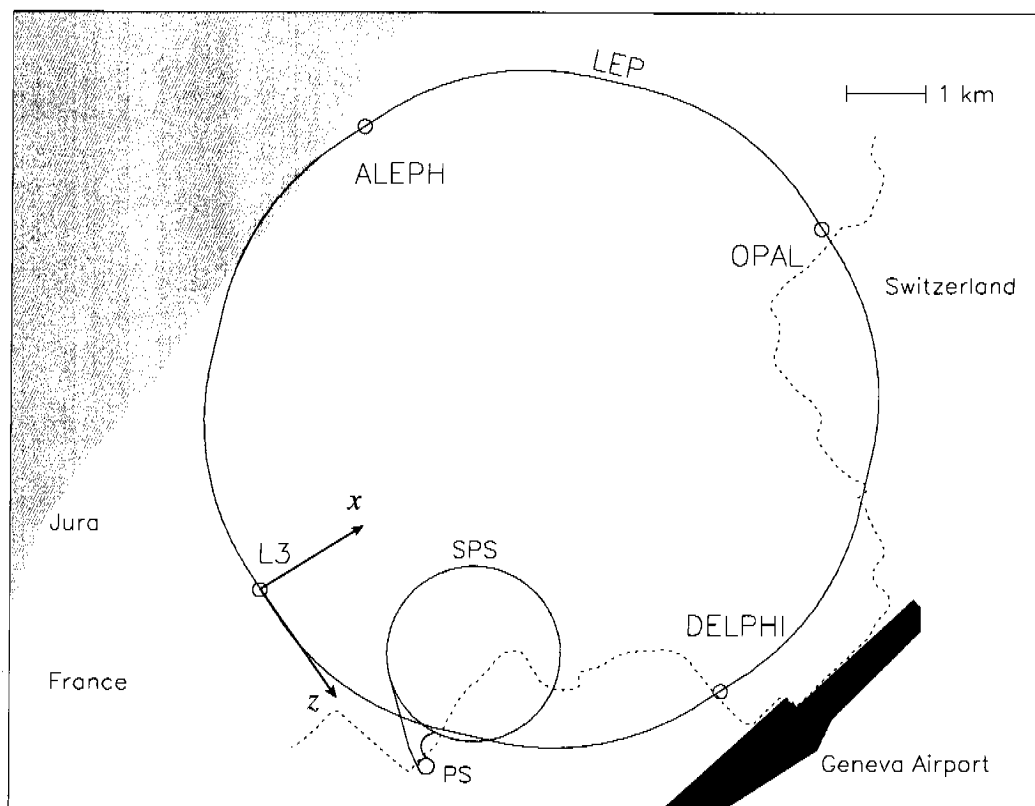


Figure 3.1: Location of L3 and other detectors at LEP. x, z are the two components of the L3 coordinate system within the LEP plane. The y -axis (not shown) is perpendicular to the $x - z$ plane.

thickness of 28.75 m. Three access shafts were established around the detector for installation and maintenance. Figure 3.2 shows the detector and its environment.

3.2 The experimental setup

As shown in Figure 3.3, from the centre point outwards, the L3 detector consisted of a silicon microvertex detector, a time expansion chamber, an electromagnetic calorimeter, scintillator counters, active leads rings, luminosity monitor, very small angle tagger, hadronic calorimeter, barrel and forward-backward muon chambers. The outermost layer was a 7800 t magnet coil and return yoke. The magnet current was 30 kA which provided a 0.5 T field parallel to the detector axis (z -axis).

For L3+C, only the barrel muon chambers were used, all the inner detectors representing passive absorbers. In addition, 202 m² plastic scintillator modules (called SCNT in the following) were installed outside of the magnet to provide precise timing information for the TDCs of the drift chambers to record the time of the randomly arriving cosmic-ray muons. To estimate the energy and the core position of the air shower associated with the detected

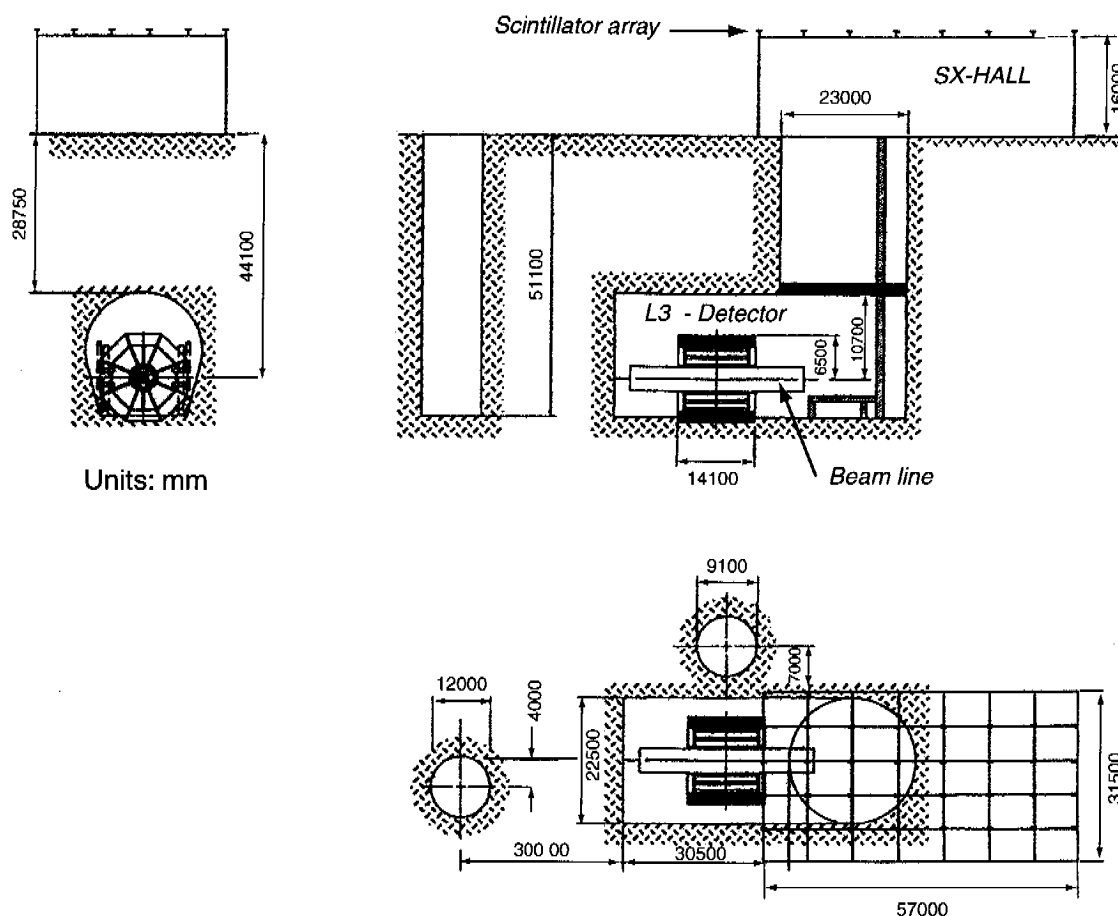


Figure 3.2: The L3+C detector and its environment including the cavern, the surface building and the three access shafts.

muons, an air shower array was mounted on the roof of the surface building.

3.2.1 The L3 muon detector

The L3 muon detector [122, 127–130] was designed to measure particularly well muons produced in e^+e^- collisions. The basic concept was to sample the muon tracks with drift chambers at three levels in a magnetic field and then to calculate their momentum from the curvature. For an ideal circular motion with a small deflection, the problem could be simplified to

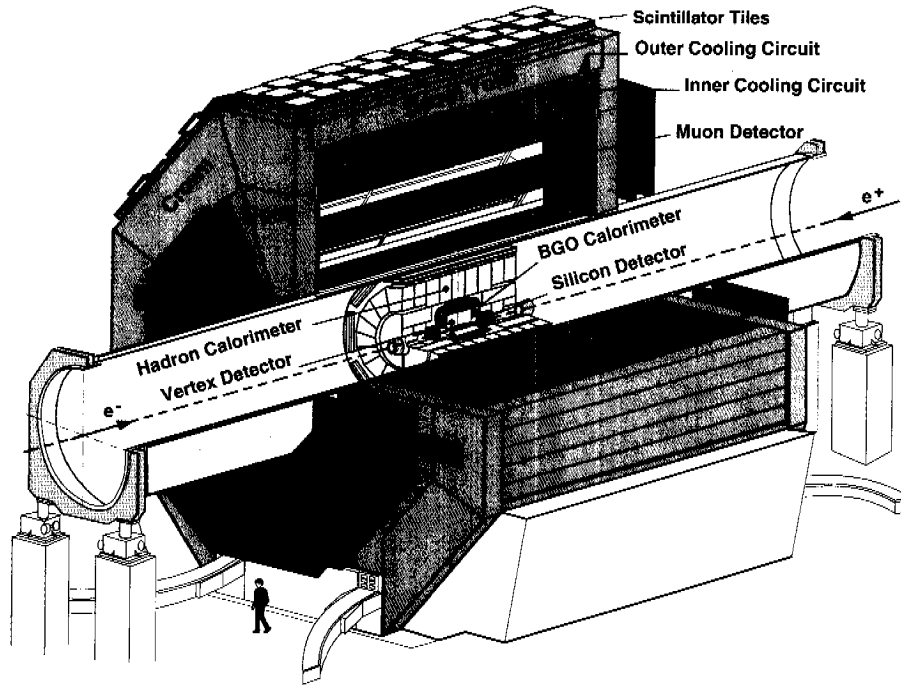


Figure 3.3: The L3 detector and the t_0 -scintillator of L3+C covering the 3 upper sides of the magnet.

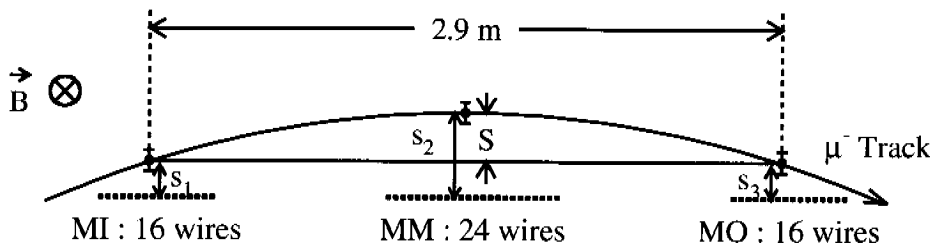


Figure 3.4: The principle of the momentum measurement (Sagitta S).

the measurement of the sagitta s , which is illustrated in Figure 3.4:

$$s = \frac{eBL^2}{8p}, \quad (3.1)$$

where e is the unit elementary charge, p is the muon momentum component perpendicular to the magnetic field, L is the length of the interconnecting line (the lever arm) and B is the magnetic field. To achieve a good momentum resolution with a given precision of the sagitta measurement, a large BL^2 is required.

L3 chose to use a B field of 0.5 T with a long bending path (2.9 m). This is obviously more efficient than a strong B field and a small length L .

The L3 muon detector was made up of two Ferris wheels (Figure 3.5), each of them

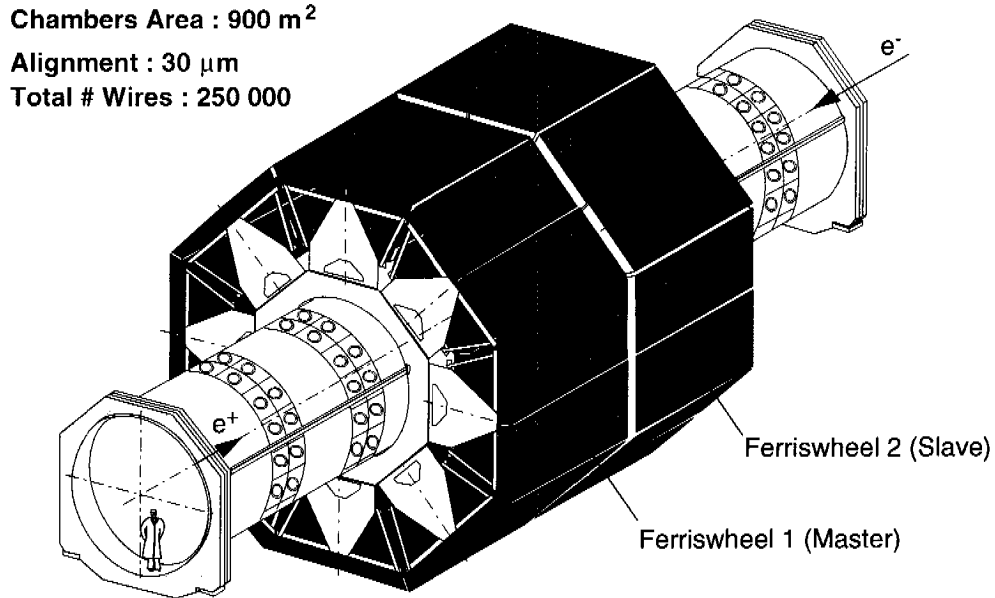


Figure 3.5: Schematic view of the structure of the L3 muon detector.

consisted of eight independent muon chamber units (octants) which were arranged in an octagon. Each octant, consisted of three chamber layers with wires parallel to the beam line: the outer chambers (MO), middle chambers (MM) and inner chambers (MI). These chambers were used to measure the muon track coordinates in the bending plane, and are therefore named *P*-chambers. The top and bottom sides of MO and MI were covered by other drift chambers (called *Z*-chambers) with wires perpendicular to the beam line in order to measure the coordinates in the *z* direction. All chambers were covered with aluminium honeycomb planes to reduce multiple scattering.

Figure 3.6 shows the end view of the *P*-chamber layers of one octant. The single wire resolution was designed to be $\sigma = 250 \mu\text{m}$. The total measurement uncertainty was reduced thanks to the multiple sampling with 16, 24 and 16 signal wires in MI, MM, and MO respectively. The uncertainty of the sagitta *s* was therefore calculated to be

$$\Delta s = (\epsilon_1^2/4 + \epsilon_2^2 + \epsilon_3^2/4)^{1/2} = 0.27\sigma,$$

where $\epsilon_3 = \epsilon_1 = \sigma/\sqrt{16}$, $\epsilon_2 = \sigma/\sqrt{24}$.

The single wire resolution had been verified with cosmic ray muon tracks to be $220 \mu\text{m}$. Therefore, the intrinsic sagitta resolution was

$$\Delta s_c = 60 \mu\text{m}.$$

Each *Z*-chamber unit which covered the top and the bottom of a MO or MI *P*-chamber had two layers of single-wire cells offset by one half of a cell with respect to each other in

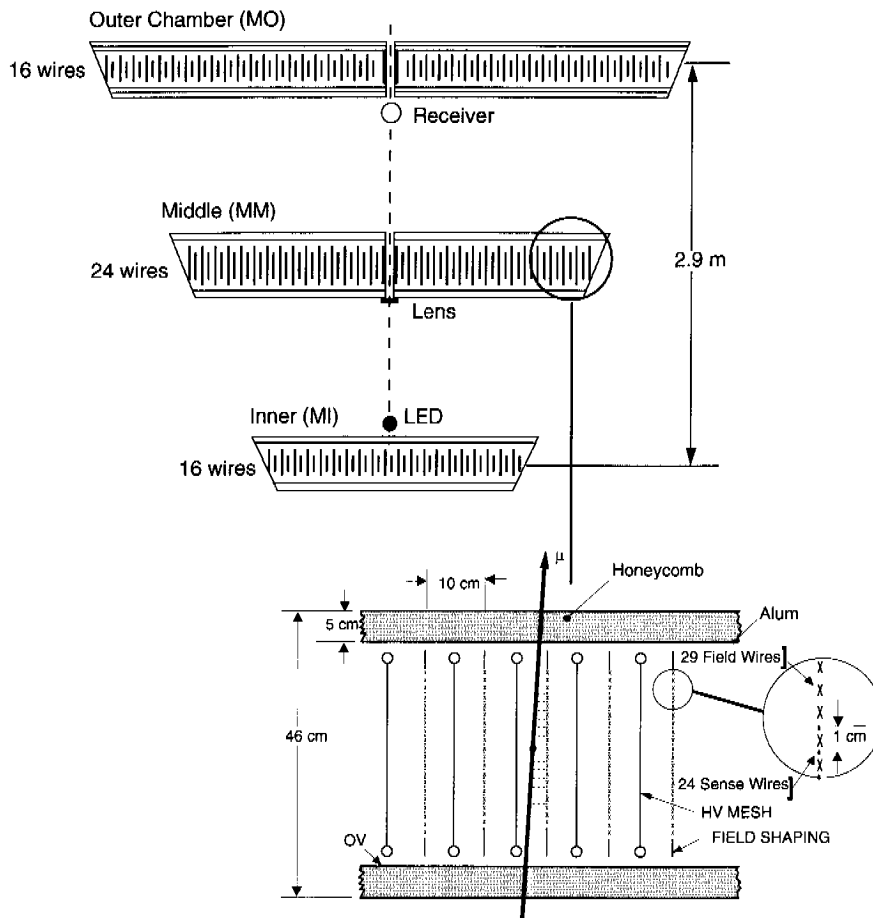


Figure 3.6: End view of the three P -chamber layers and wires in one octant, with a schematic view of the alignment system and a detail of the middle chamber.

order to resolve left-right ambiguities. The measured single wire resolution in this case was $\sim 670 \mu\text{m}$ [131].

Besides of the intrinsic resolution of the drift chamber TDCs and the multiple scattering, another major contribution to the uncertainty of the sagitta measurement is the alignment of the chambers. Very careful alignments were performed for chambers within one octant with a complex optical and mechanical system. The achieved alignment was of the order of $30 \mu\text{m}$.

The alignment between octants was not critical for the L3 experiment, since most muons produced in the e^+e^- collisions emerged from the vertex point were confined within one octant only. Therefore, the positioning accuracy of an octant relative to the beam line (of the order 2 mm) was not essential (the impact on L3+C, will be discussed in the next chapter).

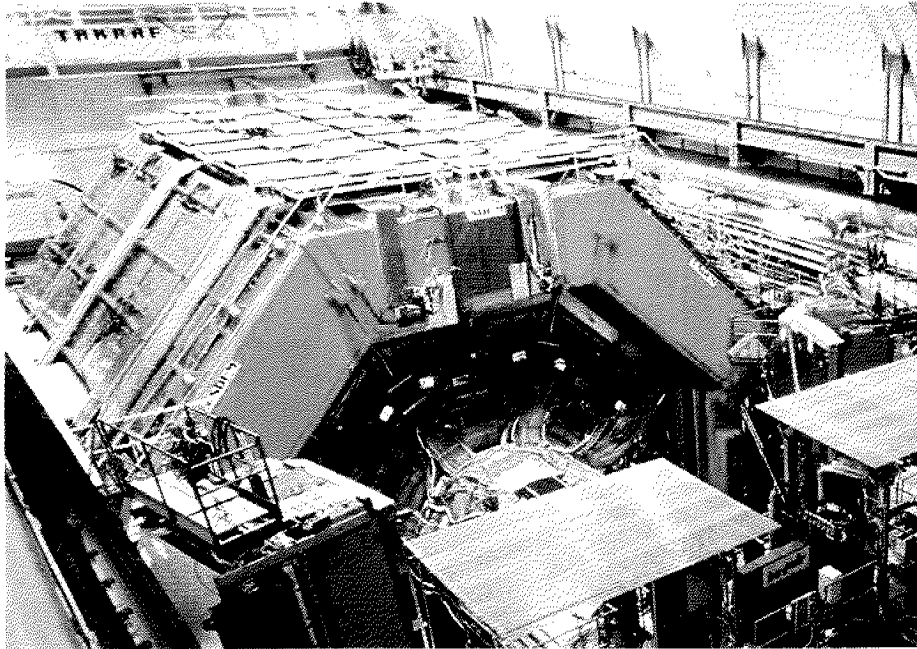


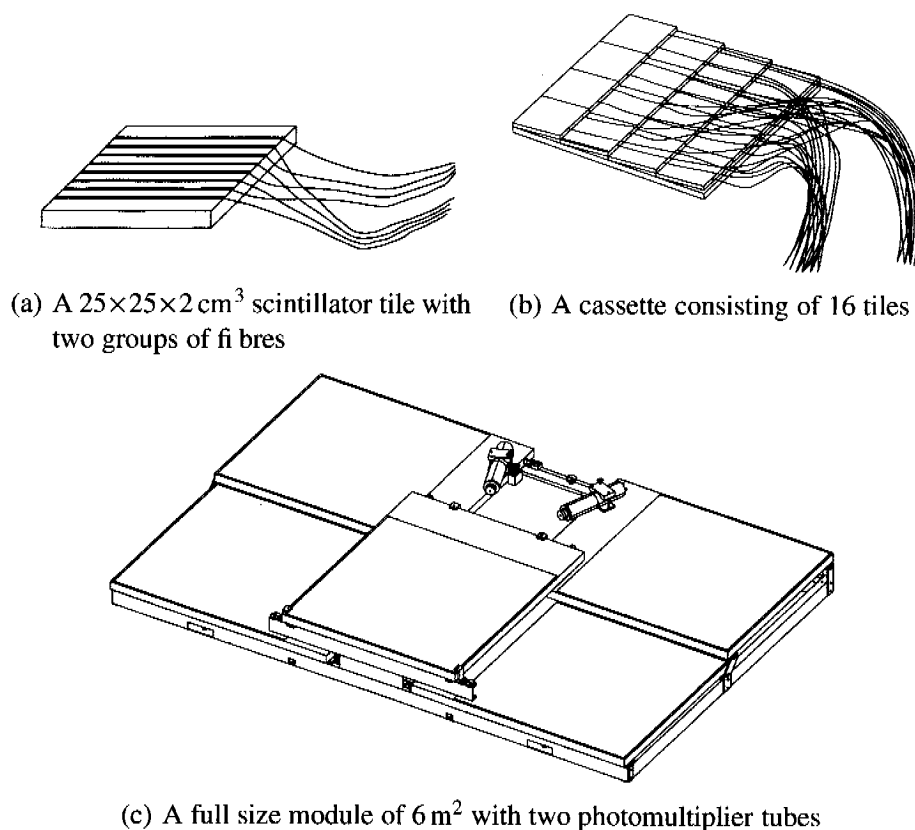
Figure 3.7: Picture of the L3+C detector system. The scintillator modules on top of the magnet were organised in different ways because of the existing environmental conditions. The muon chambers also can be seen from the opened iron doors in the foreground of the picture.

3.2.2 The t_0 detector

To provide a precise measurement of the muon arrival time (t_0) for the drift chambers, a scintillation detector system based on small plastic scintillator pieces and fast photomultiplier tubes (PMT) was developed [132]. As shown in Figure 3.7 the upper three octants were covered with 202 m^2 plastic scintillators (48 m^2 of them were old, reused NE102 tiles, while the rest consisted of new material from Ukraine).

Figure 3.8 demonstrates the concept of the scintillator modules. Each tile of size $25 \times 25 \times 2 \text{ cm}^3$ was machined with eight grooves. A wavelength shifting fibre of 1.5 mm diameter and 30 cm length was glued in each of them. These fibres were connected by a 1.8 m clear optical fibre at one end while the other ends were clad with aluminium to reflect the collected photons. After being sealed in black paper, 16 tiles were packed together and covered by a 1 mm aluminium foil creating a cassette measuring 1.0 m by 1.2 m. The additional space ($0.2 \times 1.0 \text{ m}^2$) was reserved to arrange the fibres. The fibres were divided into two groups and fed out from the cassette. The two bunches of fibres, called “left” and “right” respectively, were glued together at the end and put into a small plastic tube with a shape of one-sixth of a cylinder. Six cassettes formed a scintillator module with dimension of 3 m by 2 m. The cassettes were carefully aligned to make sure that the effective area did not overlap. Finally, the left bunch and right bunch fibres were connected separately to two fast PMTs.

Such a configuration improves the time resolution of the total detector which only depends

Figure 3.8: The t_0 -detector.

on the size of the tile and the quality of the fibres. A coincidence window of 15 ns between the two PMTs significantly reduced the thermal noise and allowed for an operation with very low-amplitude light signals.

The selected PMT (Philips XP2020, 5 cm diameter) is a 12 stage high performance tube with a rise time of about 1.5 ns and a signal transit time distribution of 0.25 ns [133]. The high voltage (HV) of each PMT was adjusted individually around the nominal value of 2500 V, compromising between efficiency and noise level. The output signals were transmitted to the electronics room, amplified and discriminated to provide inputs for the trigger decision. The PMTs were shielded by iron tubes with μ -metal layers inside, since the PMTs are very sensitive to magnetic fields, even to the geomagnetic field (47 μ T at the L3+C site [134]). The leakage B field of the solenoid near the PMTs position was measured to be less than 150 Gauss.

All modules were tested with cosmic muons before installation, and quick tests were also performed after installation on top of the magnet. The average time resolution was found to be 1.8 ns, and the average efficiency to be 96.3% [132]. The performance was also continuously monitored during data taking, and this will be described briefly in Section 4.4.2.



Figure 3.9: Air shower array mounted on the roof of the surface building

3.2.3 The air shower array

The small air shower array, which consisted of 47 scintillator modules arranged in six rows, was located on the roof of the surface building above the L3+C muon detector (see Figure 3.2 and the photo in Figure 3.9). A module was made of two pieces of plastic of size $50 \times 50 \times 1 \text{ cm}^3$. Each piece was viewed by one or two PMTs through 16 grooved-in wavelength-shifting fibres. The second PMTs, which only equipped 12 modules, were operated at a lower gain to achieve a larger dynamic range.

An independent DAQ system was attached to the air shower array. A trigger signal fired when at least one module gave a signal above threshold in each of three adjacent rows. Random trigger signals were fired every 10 s from a local oscillator and every minute from the GPS clock for pedestal measurements. Both the PMT pulse height and the signal time were recorded with each trigger. Signals from the 12 low-gain PMTs were not included in the trigger decision, and only their arrival time were recorded.

The trigger signal was cross linked with the L3+C muon trigger system. A trigger time was recorded in the other system if it fell into the others trigger window. GPS time tags were also used for the time coincidence check.

The direction of the shower axis was reconstructed through the time distribution of scintillator signals and the shower size was estimated with a fit to the NKG function (1.1).

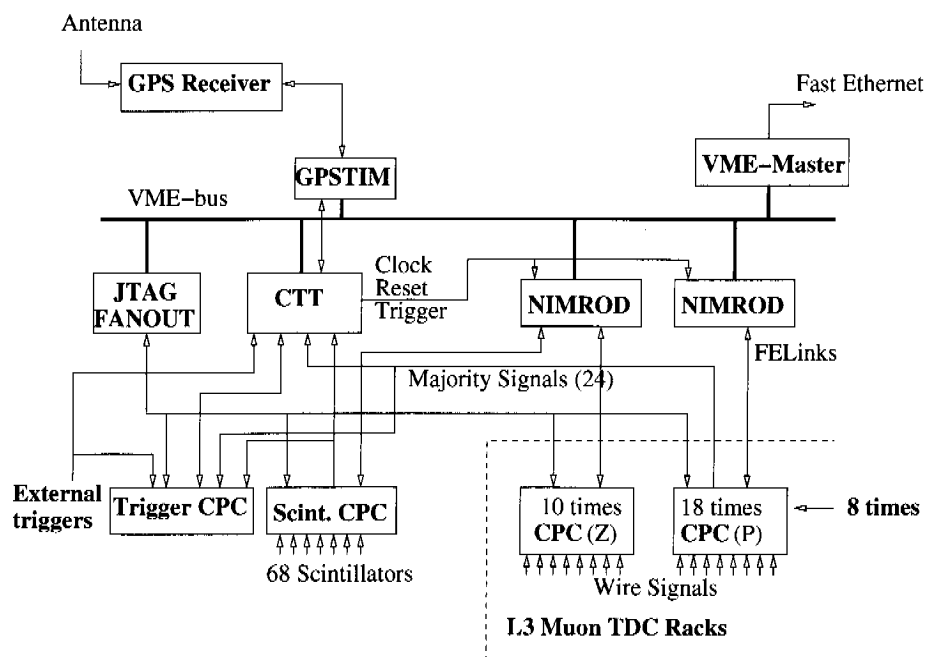


Figure 3.10: Scheme of the data acquisition system.

An analysis [135] shows that the shape of the observed shower size distribution agrees with known data. The multiplicity and pseudorapidity distributions of muons with energies above 15 GeV have been measured as function of the shower size.

The air shower array continued to run after the L3+C experiment was officially shutdown in November, 2000. The air shower data will not be used in this study and will be ignored from now on.

3.2.4 The data acquisition system

Obviously, the trigger criteria of L3+C should be different from L3. Therefore, in order to perform an independent data taking, a new DAQ system had to be developed [132]. Figure 3.10 shows a schematic view of the DAQ system.

In the L3 configuration, the 25×10^3 channels of drift chamber signals were carried to amplifiers, installed in the gap between master and slave chambers. After discrimination, the signals were sent to FASTBUS TDC modules for digitisation. The same signals were also guided to a muon personality card (MPC) installed at the rear side of the FASTBUS crate to transmit the signals to the L3 muon trigger. The MPC cards were replaced with a cosmic personality card (CPC) [136], in which the original MPC logic was kept, while a new logic was inserted.

On each CPC card, 96 input channels were distributed to three 32-channel, 21-bit TDC chips [137] running at 40 MHz external clock frequency. The time resolution was further

Table 3.1: The 12 CTT trigger classes. Triplet, doublet and singlet represent three, two or one chamber layers in the same octant having majority signals. The definition of class 8 and 9 were changed in 2000, so that the trigger efficiency could be measured directly.

Class	Description
1	Triplet in any octant with a scintillator hit
2	Triplet in octant 0 or 4 without scintillator hit
3	Triplet in octants 1, 2 or 3 without scintillator hit
4	Triplet in octants 5, 6 or 7 without scintillator hit
5	Three singlets in adjacent octants with a scintillator hit
6	Two doublets with a scintillator hit
7	Doublet and two singlets with a scintillator hit
8	Doublet and singlet with a scintillator hit (1999) Two or more <i>P</i> -chamber planes (2000)
9	Doublet with scintillator hit (1999) Three or more <i>P</i> -chamber planes (2000)
10	Triplet and at least one singlet (no scintillator requirement)
11	Five <i>P</i> -chambers (no scintillator requirement)
12	Six or more <i>P</i> -chambers (no scintillator requirement)

improved by a 32-element delay locked loop (DLL) to $\frac{25}{32}$ ns bin size.

The relative time of all signals appearing at the input of the TDCs were automatically converted to 32-bit (21 bits for the time, 5 bits for the channel number, and 6 bits reserved) data-words and stored in the corresponding channel's on-chip 256-word deep event-buffer. Events which matched the external trigger were read out through a 32-word FIFO by the CPC readout controller and sent to the NIMROD (see below) via two pairs of low voltage differential signal (LVDS) drivers.

In addition, a majority-logic was integrated to the CPC card. Every 200 ns, the number of wire channels which had a signal longer than 15 ns in a moving 1.2 μ s time window was registered. If it exceeded the programmable threshold, which was set to 8 wires, a majority signal was fired. All the majority signals from the same muon chamber layer were 'OR'ed together. Therefore, there were 24 majority signals in total, which were used for the trigger decision.

Up to 16 CPC cards were connected to a readout module called NIMROD [138] via the FELinks (Front-End Links). A NIMROD combined the data from CPCs to a NIMROD block and made it available to the VME bus. The trigger and clock signals provided by the CTT (see below) module were also distributed to CPCs via the NIMRODs.

The 24 majority signals from the muon chambers together with the ORed scintillator hit signal were sent to the cosmic trigger and timing module (CTT) [139]. Twelve pre-scalable trigger classes were programmed in the trigger logic. Table 3.1 describes the requirement

for each class. Class 1 events were considered to be *golden events*, from which a good momentum measurement could be obtained out of muon hits within one octant and a precise t_0 time. Events fulfilling classes 5, 6, 7 and 8 crossed more than one octant. These events, with a reduced momentum resolution, were also reconstructed for physics topics demanding large statistics. With the classes 3, 4, 5, 6, 7, 8 and 9, the trigger-, muon chamber- and scintillator-efficiencies could be determined directly from the data. Moreover, special classes (10, 11 and 12) were implemented for the search of exotic events exhibiting a special topological pattern in the detector.

To provide absolute timing for the L3+C events, a GPS receiver was connected to the DAQ system through a VME module (GPSTIM). The GPSTIM module also provided a stable 40 MHz clock for the system.

The DAQ system was controlled by a VME controller (MVME 2600, Lynx OS). Events were created from NIMROD blocks and send to the online computer (HP B132 workstation) via a fast Ethernet connection. The HP workstation was the master controller of the system, where various run control-, database- and monitor-processes were executed. From there, the events were written to disk files and finally sent to the central data recording (CDR) system through the network for permanent storage. A typical *RUN* lasted about 20 minutes with a maximum file size of 500 MB. Runs could be stopped before reaching the set limit, if hardware problems, high background, crashing computer processes, or artificial interventions occurred. Figure 3.11 describes the L3+C network layout for data handling, in which the offline computing facility is also included. Figure 3.12 is a simplified schematic view of the data flow.

3.3 Event reconstruction

In principle the reconstructed momenta and directions, the recorded arrival time of muons, as well as the efficiency and acceptance of the detector are sufficient for most of the physics topics listed in Section 3.5. However, in the raw data, only the relative time of a series of discrete muon ‘hits’ along the muon trajectory were recorded as well as the absolute time of the occurrence of the event [140]. A muon may produce 30-100 ‘good’ hits in the drift chambers mixed with noise hits. In order to reconstruct good tracks from the raw hits, a sophisticated software package was developed which took the material and geometry of the detector, various calibrations, backgrounds etc. into account.

An Ntuple¹ file for each raw data file is produced after the event reconstruction. Besides the necessary physics information, a set of variables representing the quality of each event is also included in these Ntuple files. Therefore, ‘good’ events can be selected according to different aspects.

The data production was started with a preliminary version of the program as soon as the raw data were available. During the extensive development of the offline software, several

¹According to Ref. [141], an Ntuple is a set of events, where for each event the value of a number of variables is recorded. An Ntuple can be viewed as a table with each row corresponding to one event and each column corresponding to given variable.

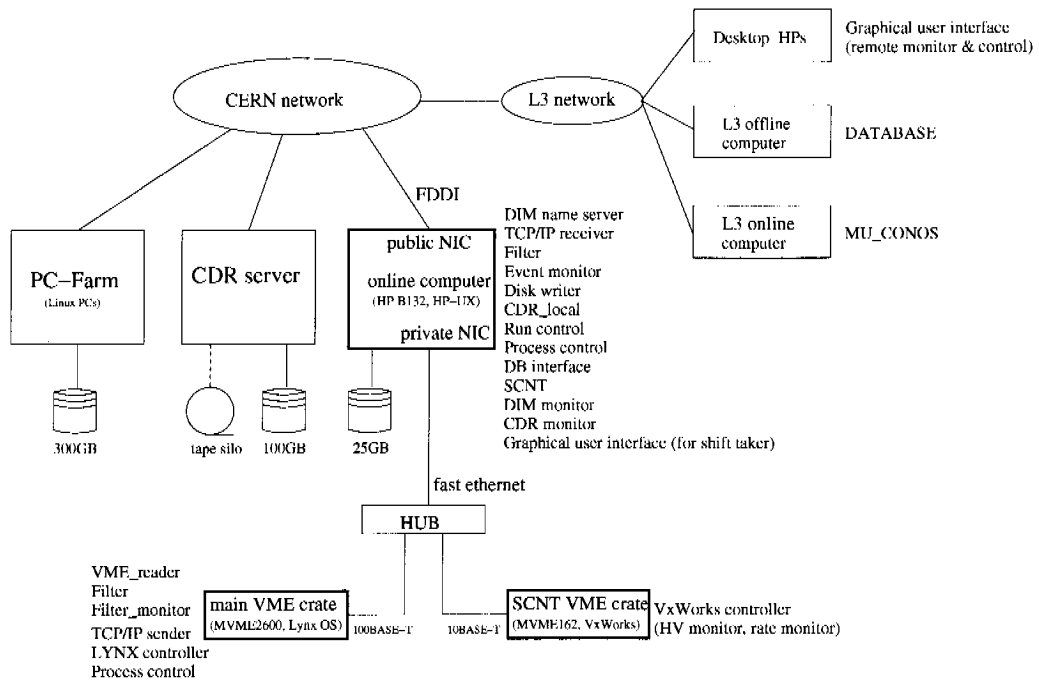


Figure 3.11: L3+C network configuration. All online processes listed in the figure (except the HV and rate monitor running in the SCNT VME controller) communicated via the distributed information management system (DIM).

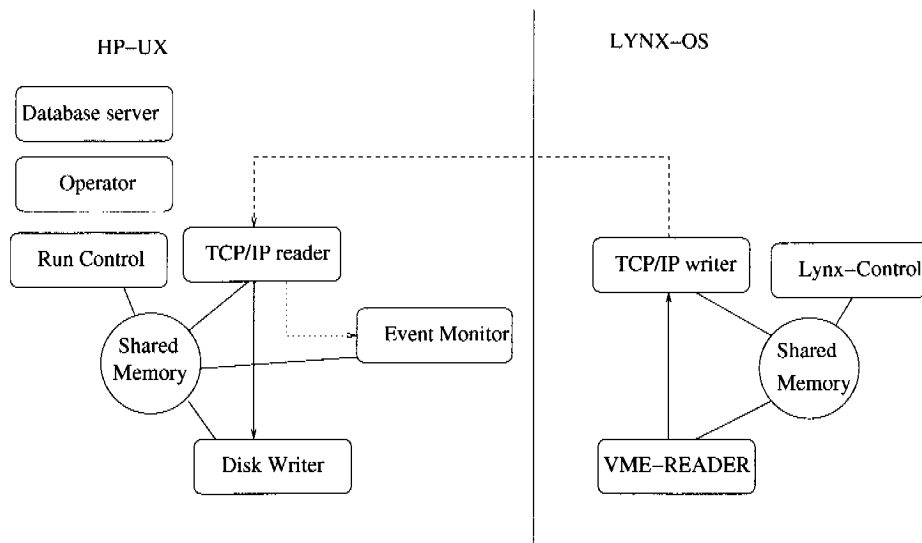


Figure 3.12: Schematic view of the data collection and monitoring software.

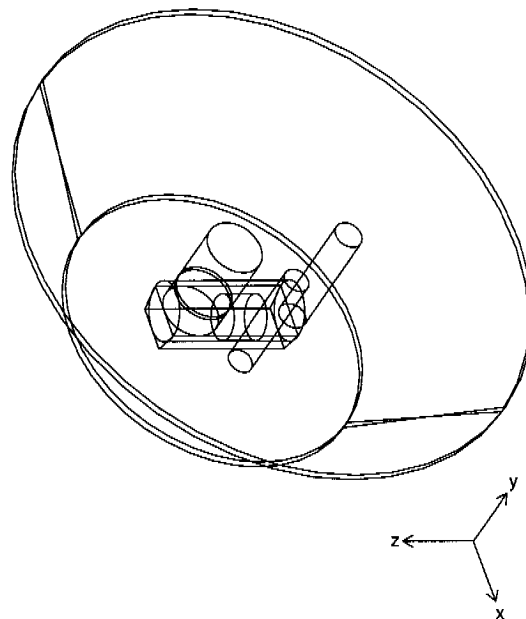


Figure 3.13: Modelling of the L3+C detector and its surroundings with GEANT3.

versions of Ntuple data were produced. There are two major branches of the software, one is called the “standard version” which reconstructs only events of class 1 ($\sim 1/3$ of all events) with the best momentum resolution, while the other one is named “cross octant version” including as many events as possible.

3.3.1 Modelling of the detector and its surroundings

The detector and its overburden is implemented in the form of the GEANT [142] structure as shown in Figure 3.13. The main volumes used in the reconstruction program as well as the simulation program (see Section 3.4) are [143, 144]:

MBAR: The MBAR volume contains the barrel part of the L3 muon chamber system. It is an octagonally shaped cylinder with a coaxial octagonally shaped hole, where the z -axis is the symmetry axis. The outside boundary is located between the MO chamber and the cooling circuit of the coil, while the inside boundary is between the MI chamber and the support tube. The two ends are flat and located between the chambers and the magnet doors.

LEP3: The LEP3 volume contains the entire detector. It is also an octagonally shaped cylinder. Its radius was increased to allow for the scintillator volumes on top of the magnet.

MOMO: The molasse layer with shafts. The composition of the overburden above L3 is well known. The overall average density and radiation length are 2.4 gcm^{-3} and 26.5 gcm^{-2} respectively.

SURF: The surface layer.

3.3.2 The “standard” reconstruction program

The reconstruction program was inherited from the L3 muon reconstruction program with a new TOF calculation and many other modifications [57, 131, 143, 145].

The main steps to reconstruct muon tracks from the raw data are:

Pre-selection: Only events labelled as class 1 are selected in this approach. The time differences between signals from the two PMTs are also required to be less than 15 ns.

Hit position determination: All TDC times are corrected for time offsets induced by different read out cable lengths and internal delays of the electronics. The drift time is obtained by subtracting the scintillator time from the wire-signal time. The hit positions are determined according to the cell map [146]. As shown in Figure 3.14, each hit position comes with an ambiguous hit, since the sense wires have no means to determine whether the hits are from the left or right side. For the *Z*-chambers, this problem is solved thanks to the relative position of the two layers of *Z*-chambers, shifted horizontally by 1/2 cell. For the *P*-chambers, however, the same problem can only be solved in the further three-dimensional (3D) fit phase.

Pattern recognition (2D segment fits within a chamber): In the *xy*-plane, all possible hit pairs are connected by straight lines. Then these lines are grouped together according to their angles and distances to form *P*-segment candidates. The candidates with more than five hits are fitted with a fast nonlinear least-square based circle-fit algorithm [147] and good combinations are recognised as segments for further processing. In this phase, each *P*-segment is accompanied with an ambiguous segment. Meanwhile, in the *yz*-plane, all hit combinations with more than two hits inside a *Z*-chamber are fitted with a straight line and the combination with the best χ^2 and largest number of hits is accepted as a *Z*-segment.

Sub-track finding (3D fits within an octant): The *P*-segments and *Z*-segments survived the pattern recognition phase are combined to form a 3D sub-track within one octant and fitted with a circle. An iterative fit is required to take into account the corrections based on the position of the scintillator hit, the time of flight from the scintillator to the muon chambers, the alignment corrections, the gravitational force induced bending of the *P*-chamber sense wires and the pulse propagation time of the *P*-chamber signal along the *z*-direction. Ambiguous *P*-segments are rejected on the reduced circle χ^2 -fit and the requirement of a maximum number of *P*-segments.

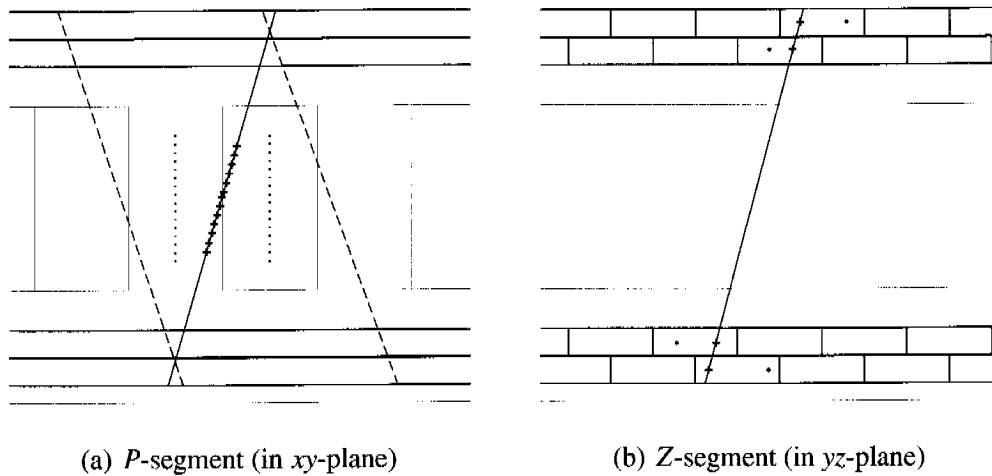


Figure 3.14: View of track segments in P -chamber and Z -chamber [57]. The segments are denoted by the solid line. In P -chambers, the dashed lines denote the ambiguous segments which can be identified only in the 3D fit phase. On the other hand, for the Z -chambers, ambiguous segments can be resolved directly.

Swimfit: In order to further improve the track accuracy, GEANE [148] is employed to trace the muons step by step (“swim”) through the inhomogeneous magnetic field and materials inside the detector. This is the so called “swimfit” phase, and the track is no longer an ideal helix.

Sub-track matching: Sub-tracks in the opposite octants are matched to a single muon track if the matching χ^2 is below a predefined threshold. Unmatched sub-tracks are also kept as tracks. The momenta and directions of all tracks are back-tracked to the boundary of the LEP3 volume and their values are stored in the Ntuple file. If the back-tracking failed, the values at the MBAR volume are calculated and stored.

Back-tracking to the surface: Again the GEANE code is used to back-track the reconstructed muon tracks to the surface level. The energy loss, multiple scattering and deflection in the magnetic field are taken into account within the MOMO volume.

3.3.3 Cross-octant reconstruction

In the “standard” version, a sub-track is limited to one octant to have better momentum resolution. Therefore, only class 1 events containing 1/3 of the total recorded data could be reconstructed. (For the precision measurement of the muon spectrum, the muon track has been fitted across two opposite octants in order to get an improved momentum determination)

Since the inter-octant alignment can be obtained directly from the L3+C data [149], muon

tracks crossing neighbouring octants can also be reconstructed. A dedicated cross-octant (XO) version of the reconstruction program has been developed [150–152]. The major differences compared to the standard version are:

- The pattern recognition is performed in the whole detector instead of only in one octant.
- The swimfit is also performed in the whole detector.
- Furthermore, the XO version is optimised for multi-muon event reconstruction.

3.4 Detector simulation

Nowadays, Monte Carlo (M.C.) techniques are essential tools for almost all experimental sciences. They play a key role in detector design, optimisation and performance studies, testing and verifying analysis programs as well as the interpretation of the experimental data. The simulation with the L3+C detector and its surroundings will be briefly described in this section.

The L3+C simulation program and the reconstruction program described in the previous section are major components of the L3+C offline computing package. The codes for detector and magnetic field description are shared between them.

3.4.1 Input interface

The input of muon events proceeds event by event via a binary data file which includes the directions, momenta and charges of muons at the surface level. The detailed data format can be found in [153]. A dedicated program used to produce such data file is usually called a generator. A generator can be very simple, for instance, generating single muon events with fixed direction and fixed momentum. On the other hand, a generator can also be very complicated, like for instance, when generating muons induced by primary particles.

L3+C has developed a general muon event generator called L3CGEN [144, 145]. It is a parameterisation of the output of a detailed air shower simulation with CORSIKA [63] which allows to efficiently generating muons at surface level.

To track the Moon along its trajectory and to study the shadowing effect, the latest CORSIKA version is directly used in this study with a customised primary event generator (see Section 6.3).

3.4.2 Muon tracking and simulation of interactions

In this simulation, GEANT3 [142] is used to track muons through the molasse layer (volume MOMO) and the detector itself (volume LEP3). Interactions with the active part of the detector are recorded in the same way as for the raw data.

3.4.3 The generic M.C. production

The simulated events are reconstructed by the same reconstruction program as used for the raw data and written to Ntuple files. Ten times the number of real events has been simulated with the L3CGEN. These M.C. data are mainly used to study the efficiency and the acceptance of the detector as well as the absolute atmospheric muon flux.

3.5 Physics topics

Besides of the antiproton search, which is the main topic of the present work, various physics topics have been or are being studied using the L3+C data set [154, 155]. A brief description is given in this section.

Atmospheric muon spectrum

The atmospheric muon flux (absolute or relative) has been measured with various experimental techniques for more than five decades. However, there were large discrepancies (up to 25% below 1 TeV [156]) between the results of different experiments.

The L3+C collaboration measured the absolute atmospheric muon flux between 20 and 3000 GeV for zenith angles ranging from 0° to 58° with a precision of 2.3% (total error) at 150 GeV in the vertical direction [57, 58]. Figure 3.15 shows the L3+C vertical muon spectrum and compares to previous direct measurements. In addition, the ratio of positive to negative muons was estimated to be $1.285 \pm 0.003(\text{stat.}) \pm 0.019(\text{syst.})$ also for vertical incidence and between 20 and 500 GeV.

This precise measurement provides constrains on the atmospheric neutrino flux calculation due to the fact that muon neutrinos and muons are the two decay products of mainly pions and kaons. The ν_μ - and $\bar{\nu}_\mu$ - flux is relevant for neutrino oscillation studies and for neutrino astronomy experiments.

Point sources

The high duty cycle allowed the L3+C collaboration to perform a sky survey of the northern hemisphere 24 hours a day by monitoring muon events, as well as from known sources of gamma rays and other neutral particles. Due to the short data taking period and the fact that primary γ 's produce much fewer muons than protons, no constant signal from sources was expected to be observed. However, flaring type sources were searched for in the data with different techniques [145, 157, 158]. A TeV gamma-ray source candidate signal (with characteristic properties different from statistical fluctuations) has been found at R.A. of $(172.53 \pm 0.17)^\circ$ and declination of $(-1.19 \pm 0.17)^\circ$ with a chance occurrence of $2.3 \cdot 10^{-3}$ [158, 159].

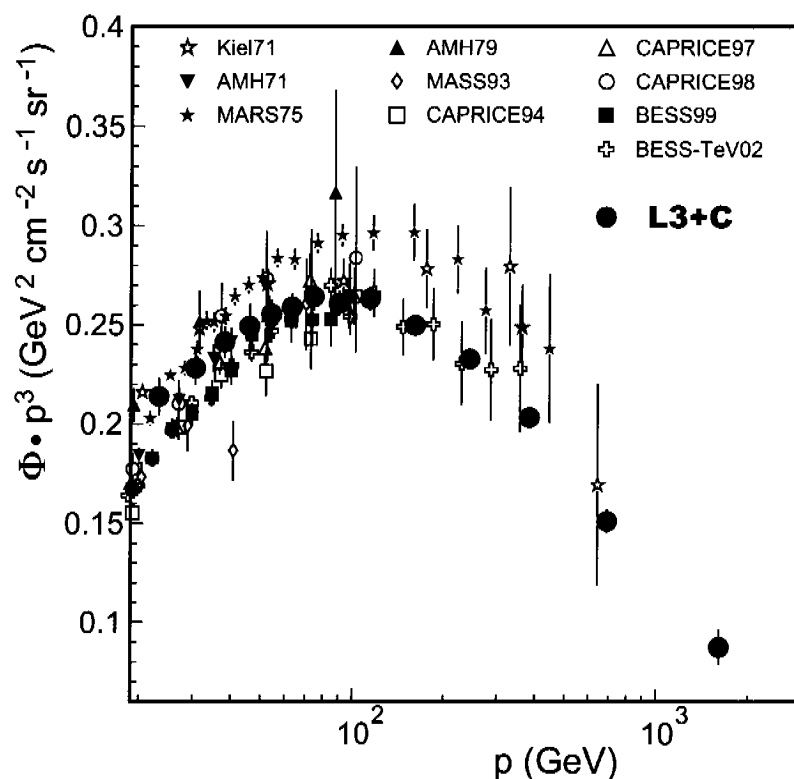


Figure 3.15: The L3+C vertical muon spectrum compared to previous direct measurements providing an absolute flux normalisation [58]. All data are extrapolated to sea level.

Gamma-ray bursts (GRB)

Eight GRBs from the BATSE catalogue, which fell into L3+C's time window and the field of view, have been investigated. No evidence of high energy signals from these GRBs was found [160].

Cosmic ray composition in the knee region

The cosmic ray composition in the knee region could be investigated by measuring the multiplicity as a function of the muon energy and the shower size thanks to the air shower scintillator array [161]. The "cross-octant" version of the L3+C reconstruction program is able to process multiple muon events with multiplicities up to 50 [162].

Solar flare signals

The solar flare of the 14th of July 2000 has been extensively studied with the L3+C muon data [163–165]. A 4.2σ excess of muons with energies between 15 and 25 GeV in a particular sky

region was observed within a time interval of 18 minutes starting from the time when the X-ray flux of the solar flare reached a maximum. Taking into account the trial numbers involved in the search, the probability of finding such an excess due to a background fluctuation is about 1%.

Exotic events

Some unusual events observed in the Kolar Gold Field experiment, the LVD detector in the Gran Sasso tunnel and the Yunnan cloud chamber could not be interpreted with present knowledges. The L3+C experiment is capable to search for “Kolar-like” events which have two or three tracks with large momenta, a large opening angle between them, and a vertex in the air near the detector [166]. Such events are likely to be explained as the observation of unstable particles with large mass and low velocities. Besides searching for patterns of the decay products, another on-going approach is to search for low velocity particles directly with a special TOF algorithm [167].

Chapter 4

Detector performance and data selection

As described in the previous chapter, L3+C is a complex detector. There were many interferences during data taking, such as LEP noise, various detector and electronics problems, and artificial interventions. The status of the data taking had been monitored and evaluated for different aspects, i.e. the online database [168], the online logbook [169], and offline data quality checks [170–173].

In this chapter, the performance of the L3+C detector and the stability of the data taking is discussed. The data selection is described at the run- and event-level respectively. The goal is to select muon events with good angular resolution while keeping as many events as possible. Both items are essential for the Moon shadow analysis.

4.1 Data taking

After the test runs taken in the year 1998, the data taking was performed between May 3 and November 9 in 1999, and between March 31 and November 13 in 2000. About 12 billion muon events corresponding to 12 TB of data were collected in parallel with the LEP physics runs during these two years (Figure 4.1).

A large amount of interventions and optimisations were performed to the detector and the DAQ system before the 15th of July 1999. Therefore, data collected during this period are not suitable for any physics study. A summary of the reconstructed runs in the stable period is listed in Table 4.1. The average experimental trigger rate was 436.4 Hz (418.0 Hz) in 1999 (2000). The difference was due to changes in the trigger class settings (see Table 3.1). The overall performance of the data taking was increased with less down time in the second year thanks to optimisations applied to the online system based on the experiences gained from the previous year.

There were gaps between runs with a typical length of a few tenths of seconds (see Figure 4.2). The recovery time was necessary to update the online database (i.e. status of the detector, DAQ system, environment, etc), and to initialise or reset the DAQ system. Since the data-taking had to be stopped when the L3 magnetic field was switched off during LEP maintenance, longer gaps, up to one or two days also existed.

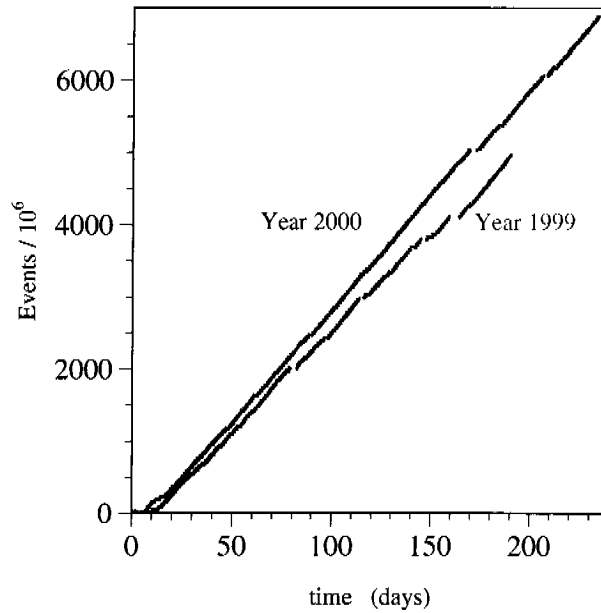


Figure 4.1: Number of collected events as a function of data taking days in the year 1999 and 2000. The data taking started on May 3 in 1999 and March 31 in 2000 respectively.

Table 4.1: The selected data taking periods.

Year	1999	2000
Period	15 Jul. – 9 Nov.	31 Mar. – 13 Nov.
Total run duration [days]	82.9	189.0
Total live time [days]	81.3	186.4
Time between runs (gaps) [days]	34.3	38.3
Number of runs	18321	16863
Number of events [$\times 10^9$]	3.125	6.825
Experimental trigger rate [Hz]	436.4	418.0
Corrected trigger rate [Hz]	445.0	423.8

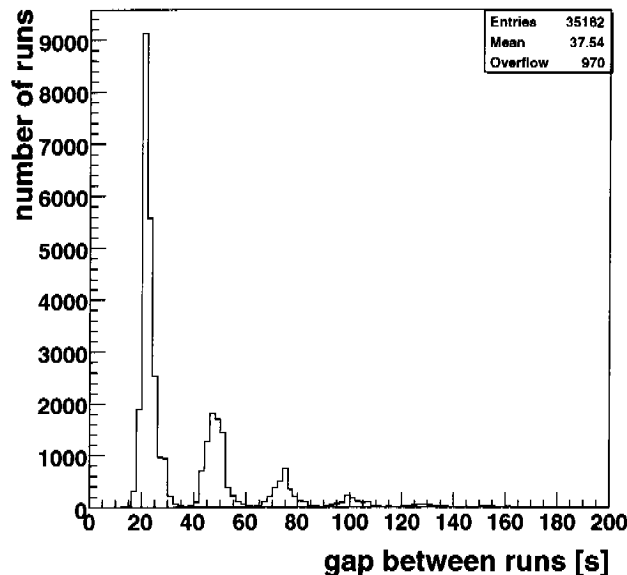


Figure 4.2: Distribution of time between runs during the 1999–2000 data taking period (see Table 4.1).

4.2 Run selection

In order to keep the statistics as large as possible, only very loose cuts are applied at the run level:

As described in Section 3.2.4, a typical run lasted about 20 minutes. However, many runs were stopped before reaching this limit due to different reasons. Normally, the data quality is not affected, for example, if it was caused by a crashed computer process. Therefore, only runs with live-time less than 20 s are excluded from the analysis.

During some runs, the magnet current was switched off or degraded. These runs are removed according to the list from [170].

As shown in Figure 4.3, the distributions of live-time to real-time ratio in both years are sharply peaked at about 98%. A small live/real ratio indicates more dead time which is an effect of high background. The ratio is required to be larger than 95% which corresponds to an average dead time of 100 μ s for a trigger rate of 500 Hz.

On the other hand, the trigger rate distribution is peaked at 446.8 Hz (418.8 Hz) in 1999 (2000) (Figure 4.4). Runs with abnormal rates (< 400 Hz or > 600 Hz) are removed.

Since double muon events are used for the angular resolution study (see Chapter 5), the ratio of double muon events to single muon events, which is expected to be a constant, is also used as a selection criterium. As shown in Figure 4.5 the distribution of the ratio has sharp peaks at 0.023 (0.026) respectively in 1999 (2000). The slightly better performance leads to increased efficiency for the double muon reconstruction in 2000. The deviation of the double muon to single muon ratio from the most probable value (MPV) is required to be less than

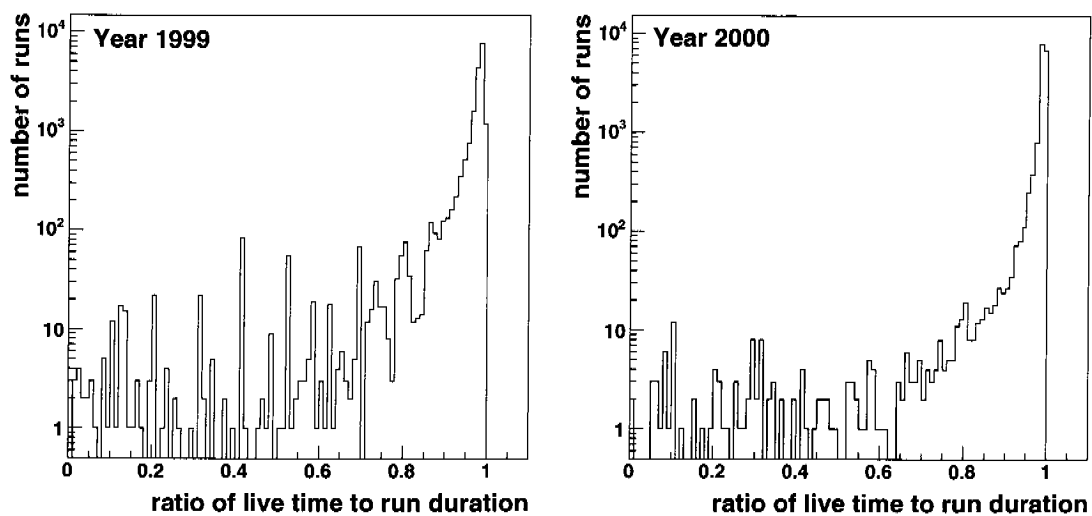


Figure 4.3: Ratio of the live time to the run duration.

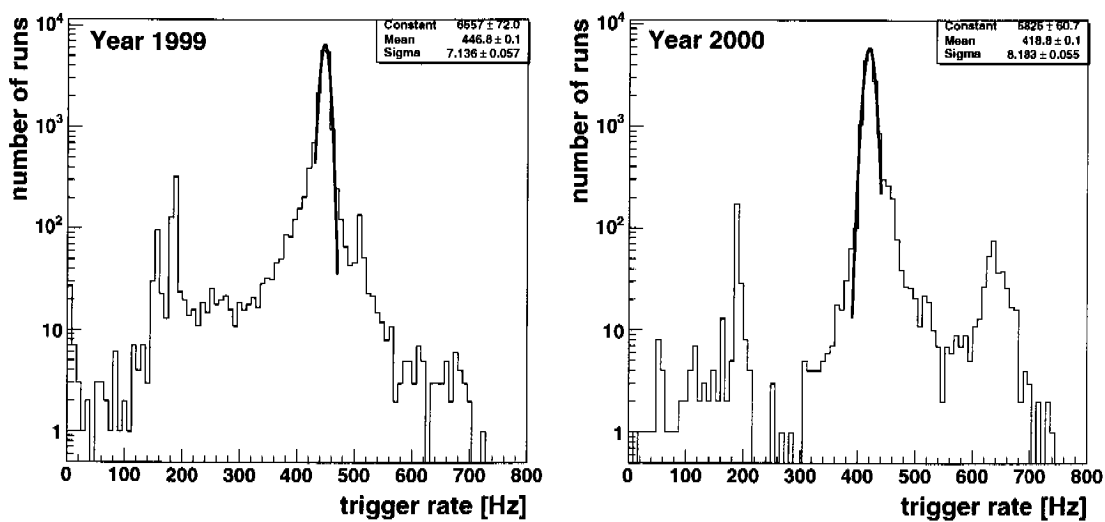


Figure 4.4: The trigger rate.

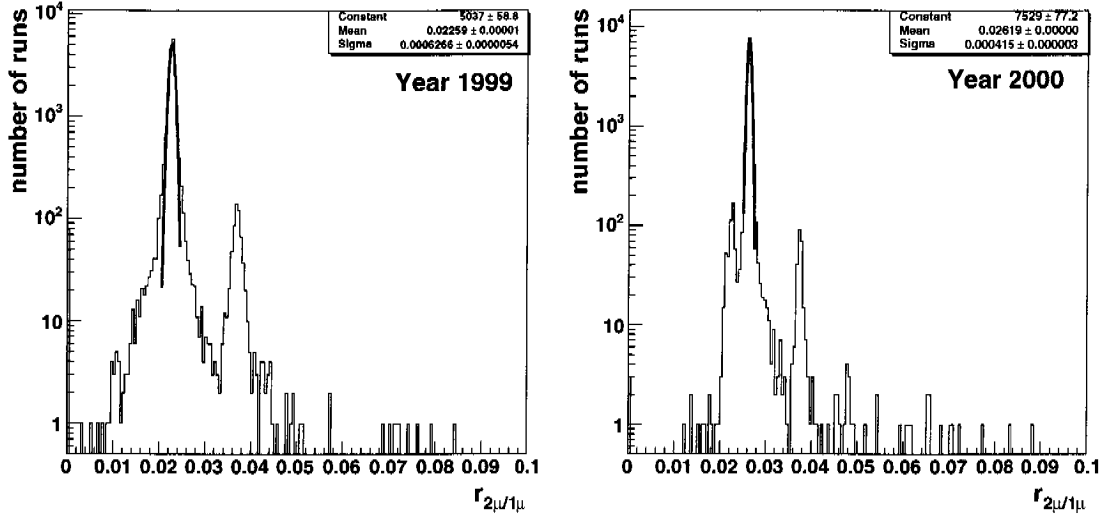


Figure 4.5: Ratio of double muon events to single muon events.

Table 4.2: Run-level selection criteria and the number (fraction) of runs, events and live-time days that satisfies the requirement. See the text for explanation.

Requirement	# runs	# events [$\times 10^9$]	Live-time [days]
$t_{\text{live}} > 20$ s	33916 (96.4%)	9.94 (99.9%)	267.5 (99.95%)
Stable magnetic field	35062 (99.7%)	9.92 (99.7%)	266.9 (99.7%)
$\frac{t_{\text{live}}}{t_{\text{real}}} > 0.95$	31838 (90.5%)	9.74 (97.9%)	263.2 (98.3%)
Trigger rate (400-600/s)	32715 (93.0%)	9.62 (96.7%)	255.1 (95.3%)
$r_{2\mu/1\mu} - r_{2\mu/1\mu}^{\text{MPV}} < 4\sigma$	33436 (95.0%)	9.50 (95.5%)	252.2 (94.2%)
All above requirements	30320 (86.2%)	9.34 (93.9%)	248.5 (92.8%)

four standard deviation.

The requirements and the selection results are summarised in Table 4.2. In total, 30320 runs corresponding to 9.34×10^9 triggers and 248.5 days of live-time passed all the cuts.

4.3 Event selection

The selection at the event level is based on a subset of the quality variables available in the Ntuples [174]. A good event must satisfy all the following requirements:

- Only one track (successfully back-tracked to surface). Events with two muon tracks are also selected separately for the DAQ status monitoring and angular resolution study.
- A hit should be recorded in the scintillator module traversed by the muon. This is essential to have a good timing information.
- Each muon track contains at least three *P*-segments. To obtain an accurate sagitta of a track for the momentum calculation, three segments are the minimum.
- Each muon track contains at least two *Z*-segments. One *Z*-segment alone could determine the direction component along the non-bending axis, however, with unacceptable uncertainties.
- The swimfit succeeded. The energy loss of a muon propagating through inhomogeneous material and magnetic field is taken into account in the swimfit. Therefore, better momentum and angular resolution are expected.
- The muon track does not go through the magnet door.
- The muon track does not go through vertically aligned cells.

The event selection criteria (except the last two requirements which most of events fulfilled) and the number of events that fulfilled the requirements, are summarised in Table 4.3. In total 2.88×10^9 events passed all the cuts.

Table 4.3: Event-level selection criteria and the number of events which fulfilled the requirements.

requirement	# of events [$\times 10^9$]
Back-tracked to surface	6.42
Swimfit succeeded	5.51
Crossed SCNT module with hit	5.84
≥ 3 <i>P</i> -segments	5.90
≥ 2 <i>Z</i> -segments	3.55
All above requirements	2.88

4.4 Detector performance

The main features of the detector and the DAQ system are described in this section. The “high-level” performances of the L3+C experiment are described elsewhere: The momentum resolution, which is a critical parameter for the muon spectrum study, has been investigated in [57]. While for topics dealing with astronomical objects, e.g. the Moon shadow analysis in the present work, the angular resolution, which is discussed in Chapter 5, is more important.

4.4.1 Timing accuracy

The absolute event time was measured with the GPSTIM module which is synchronised with a GPS receiver at the beginning of each run. The expected timing accuracy is 1 μ s. However, the serial connection (RS232) established between them was not very stable, therefore bit errors were observed in the GPS telegram in some runs ($\sim 10\%$). The error can be easily identified by comparing the GPS time and the Unix time in the run header, since the error is at least one second which is the minimum time unit of the GPS telegram. A thorough study showed that the wrong GPS time can be corrected with a precision of $\sim 10^{-4}$ s with the help of the Unix time attached to each event [175].

Inside a run, the event time offset is measured with two counters, one coarse time counter with a minimum resolution of 1 s and one fine time counter with a precision of 0.1 μ s. Figure 4.6 (a) and (b) show the distribution of the time difference between consecutive events (Δt) in a subset of the data sample. The dead time of the data taking is observed to be $\sim 6 \mu$ s, which corresponds to the trigger time window (4.4 μ s) and additional trigger hold off time introduced by the CTT module and the NIMROD modules, as well as the GPSTIM module.

The time of randomly arriving cosmic-ray muons is expected to follow the Gamma distribution of order M [176]:

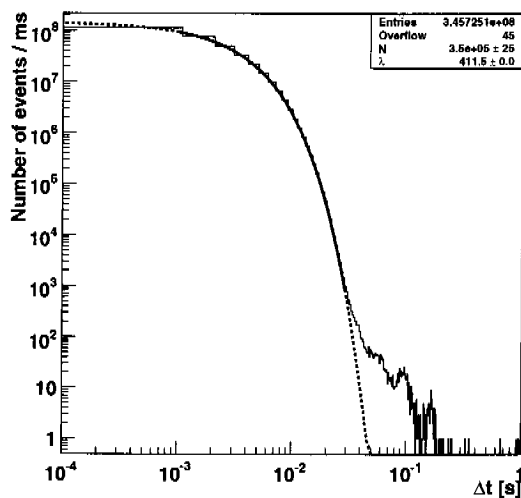
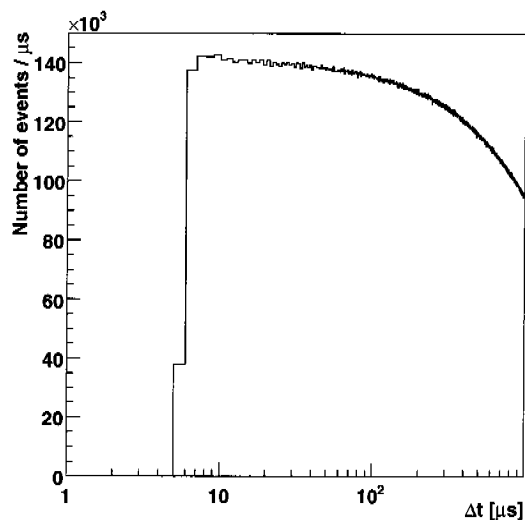
$$G(\Delta t; \lambda, M) = N\lambda \frac{(\lambda \Delta t)^{M-1} e^{-\lambda \Delta t}}{(M-1)!}, \quad (4.1)$$

where λ is the average event-rate in live-time and N is a normalisation factor. For $M = 1$, equation (4.1) reduces to an exponential function:

$$G(\Delta t; \lambda, M = 1) = N\lambda e^{-\lambda \Delta t}. \quad (4.2)$$

The time distribution can be well fitted to equation (4.2) between 10^{-3} s and 3×10^{-2} s (Figure 4.6(a)). Large deviations to the expected distribution with long gaps were caused by the hold-off of the readout system. The trigger would be inhibited when the number of event piped in the readout buffer approached the threshold of 8 (see Figure 4.6(c)). Big gaps (1 – 10 s) are also observed before the first event and/or after six events at the beginning of the run. This is attributable to the delayed initialisation process.

The two-counter ‘clock’ caused some errors too. Occasionally, the carry digit was lost during the clock readout. This error appeared in the event chain as a time jump back and forth at an interval slightly less than 1 s. This error is corrected during the event selection.

(a) Δt distribution ($M = 1$).

(b) Zoom in of (a)

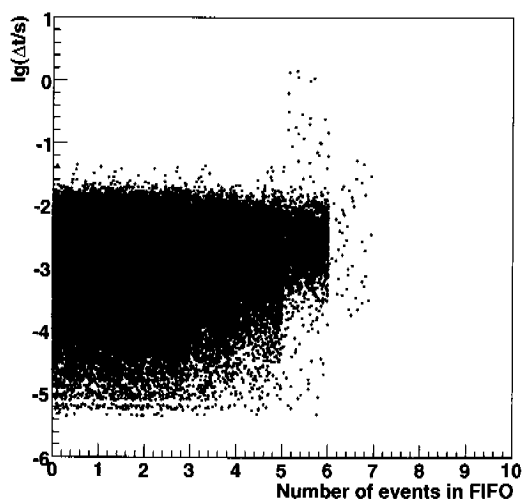
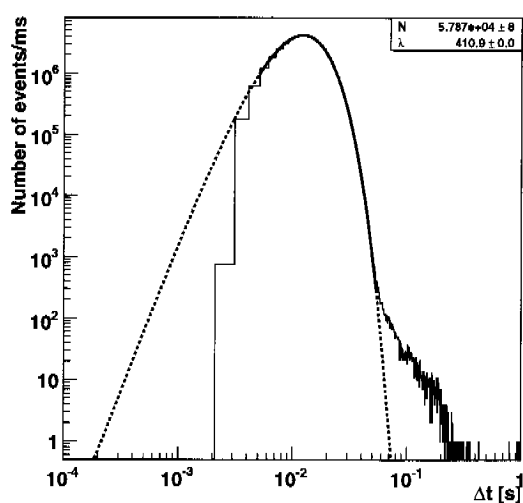
(c) Δt as a function of the number of events waiting in the FIFO of the CTT module.(d) Δt distribution ($M = 6$).

Figure 4.6: Event time distributions for data recorded during the last 10 days in the data taking period of year 2000 when LEP has been shut down.

Besides of all these explicitly “unusual” event delays, only one very long delay (46 s) was found in the “good” run list. The online logbook indicates that the DAQ system was not operational at the end of the run. Consequently, this run has been flagged manually to be “bad”.

4.4.2 Scintillator efficiency

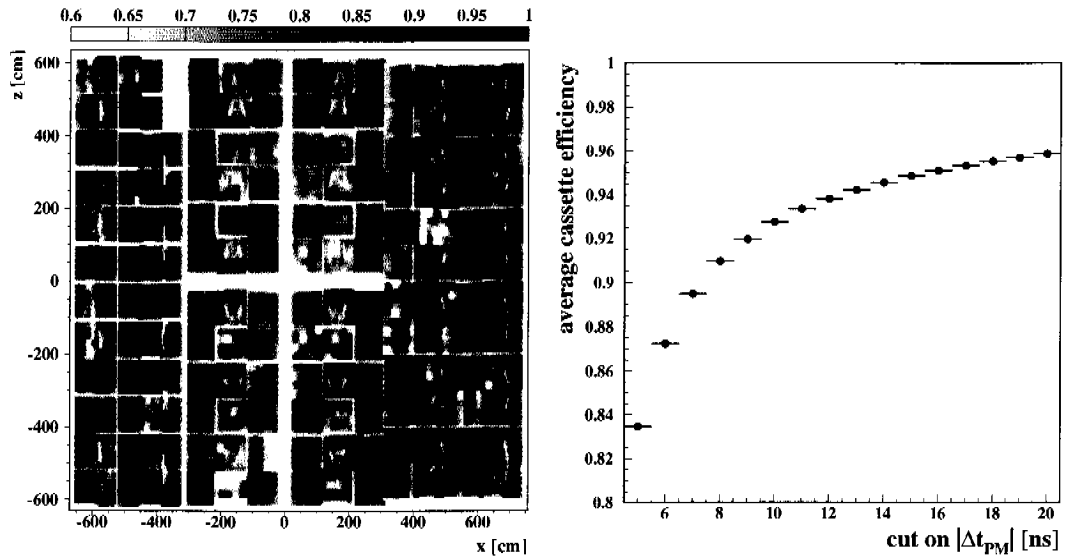
As mentioned in Section 3.2.2, the efficiencies of all scintillator tiles, and cassettes had been measured before the start of the data taking. As usual, the plastic scintillators are expected to suffer from the so called ageing problem which reduces the light yield and therefore decreases the efficiency. The radiation induced by LEP further speeds up this process. Another problem arose from the over-bending of the light-guiding fibres, due to the limited installation space for some modules. The flexing fatigue causes cracks and even breakages in the fibres, and eventually diminishes their transparency.

The time and position dependent scintillator efficiency has been investigated with a special event reconstruction algorithm [57]. There are about 42% of events having muon tracks crossing at least one of the chamber wire planes. The muon arriving time in these events can be determined by interpolating hit times in muon chambers when it crosses the wire plane. Then the reconstructed muon track is back-tracked to the scintillator layer where the scintillator hit is checked. Figure 4.7 presents the measured efficiency and its dependencies.

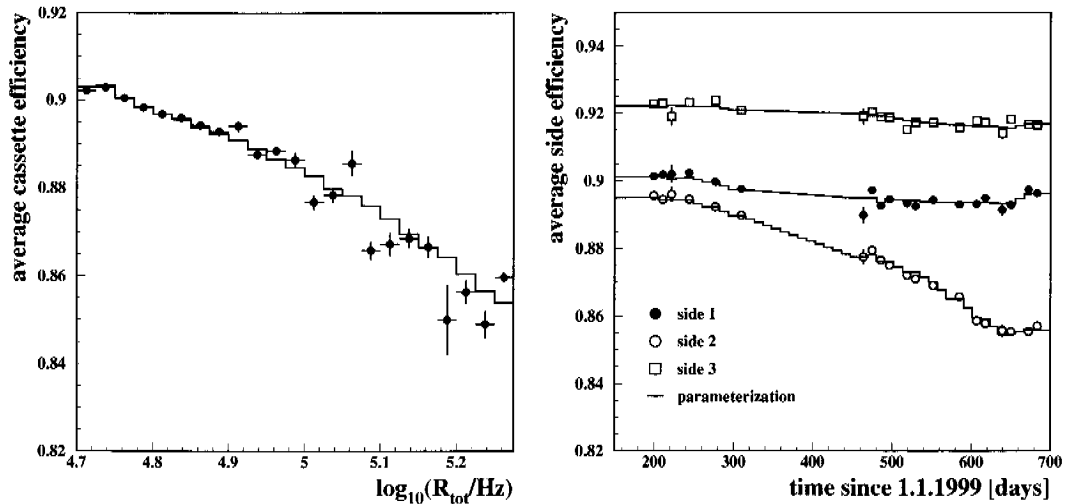
The structure of the scintillator modules and their layout on the magnet (see Figure 3.7) and even the lower efficiency caused by the PMT shielding tubes are clearly visible in Figure 4.7(a). The two large gaps were reserved for maintenance. Figure 4.7(b) shows that the efficiency depends on the offline adjustable width of the coincidence window between the two PMTs. A tight cut tends to decrease the efficiency. In Figure 4.7(c), anti-correlation is observed between the scintillator efficiency and the noise induced by the LEP beam. Finally, the time dependence of the efficiency is shown in Figure 4.7(d). As a consequence of the reuse of old scintillators, the efficiency of side 2 was decreased by about 4%, which is much higher than that of side 1 and side 3 where new material was used. The slight increase in efficiency at the end of the data taking was due to the fact that LEP was already shut down (no accelerator induced noise).

4.4.3 Muon chamber efficiency and alignment

The properties of the muon drift chamber, i.e. the wire resolutions and efficiencies as well as the relative alignment inside an octant had been well monitored and investigated by L3 (see Section 3.2.1). For L3+C, cosmic-ray muons may cross two octants. To achieve a good momentum resolution, the alignment between octants must be well understood. This has been determined with the data of through going muons [57]. Events were firstly reconstructed within one octant, then subtracks belonging to the same muon were matched on average by shifting and rotating the coordinates of the corresponding octants. For each run, the alignment parameters were determined with the data recorded within ± 12 hours around the data taking time. The main features of the muon chambers are tabulated in Table 4.4.



- (a) The coordinate dependent average efficiency of the two years. The scintillator tiles are projected to a horizontal plane and efficiencies below 0.6 have been cut out.
- (b) Efficiency as a function of the width of the coincidence window between the two PMTs (Δt_{PM}) (data from July 1999).



- (c) Average cassette efficiency as a function of the counting rate ($\Delta t_{PM} \leq 8$ ns).
- (d) The time dependence. ($\Delta t_{PM} \leq 8$ ns)

Figure 4.7: Scintillator efficiency dependencies (reprinted from [57]).

Table 4.4: Muon chamber performance.

Parameter	Estimated value	Remarks
Wire resolution		see Section 3.2.1
<i>P</i> -chamber	220 μm	
<i>Z</i> -chamber	670 μm	
L3 alignment		within one octant
misalignment	30 μm	
sagitta uncertainty	60 μm	
absolute misalignment	2 mm	
L3+C alignment [57]		confirmed the L3 design value
single octant	$\leq 60 \mu\text{m}$	corrected in event reconstruction
inter-octant	$\leq 6 \text{ mm (1 mrad)}$	after alignment correction
effective sagitta uncertainty	0.15 mm	
Bad cells [57]		numbers at the end of the year
<i>P</i> -chamber (1999)	107 (7.3%)	
<i>Z</i> -chamber (1999)	570 (5.0%)	
<i>P</i> -chamber (2000)	57 (3.9%)	
<i>Z</i> -chamber (2000)	731 (6.4%)	
Efficiency [57]		bad cells excluded
<i>P</i> -chamber	98.7%	
<i>Z</i> -chamber	91.7%	

Chapter 5

Angular Resolution

The significance of observations of point-like sources or “anti-sources” like the shadowing effect cast by the Moon, or the Sun, is inversely proportional to the angular resolution and proportional to the square root of the number of events. Thus the angular resolution is the most important parameter for the present analysis and must be well understood.

In L3+C, only the directions of secondary muons are measured. We can only use this information to estimate the direction of the parent primary particle. Therefore, the uncertainty of the angular measurement includes the production angle within the air shower, the muon propagation through the atmosphere and the molasse above the detector, the detector performance and the precision of the reconstruction program. All effects can be studied by a detailed M.C. simulation and the main part of them can be verified by the double-muon events recorded.

Two (or more) muons can be produced in the upper atmosphere during the air shower development. These muons are expected to arrive at the Earth surface practically parallel if they fall within a relative small region, i.e. the size of the detector. Taking into account the multiple scattering effects in the overburden and the detector response, the measured tracks are no longer parallel. Therefore, the distribution of the opening angle between two muons is a good measurement of the angular resolution.

This subject has been studied at length with an earlier version of the Ntuple data (version ‘h’) [121]. The dependence of the resolution on the muon momentum and zenith angle had been determined separately. The M.C. simulation was found to agree with the data. However, discrepancies (of the order 2σ) were found between the values determined from double-muon data and the Moon shadow analysis.

To better understand the dependence of the resolution, a new technique based on an unbinned maximum likelihood method is developed with the Ntuple data of version ‘D’. The goal is to find a way to describe the angular distribution probability at the event level.

5.1 Muon propagation (multiple scattering)

There are mainly two types of physics processes involved in the propagation of muons through matter: the energy loss and the multiple coulomb scattering. The main energy-loss channels have been described briefly in Section 1.4.2 using the atmosphere as an example. This section discusses the effects of multiple scattering, which is the main contribution to the uncertainty of the L3+C directional measurement.

While muons (charged particles in general) lose energy continuously when passing through material, they also undergo a series of statistical independent or nearly independent scatterings which is dominated by Coulomb forces. The multiple scattering is well described analytically by the Molière theory [177, 178]. Briefly speaking, this theory is based on the Rutherford cross section with the screening effect by atomic electrons. It is well-known that the angular distribution is non-Gaussian, which includes a Gaussian peak due to the successive small angle scatterings, and a long tail caused by single scatterings at large angles.

A muon scattering experiment at 50 – 200 GeV/c demonstrated that the Molière theory is in good agreement with high energy muons for small deviation angles [179]. However, a more recent experiment with muons at 7.3 and 11.7 GeV/c indicates that the theoretical prediction overestimates the deflection at large angles [180]. Therefore, a modified Molière theory is suggested in [181] by taking into account the finite size of charge distribution in the nuclei, as well as the incoherent scattering on atomic electrons. This approach is necessary when dealing with thick matter layers, where the nuclear form factor plays a significant role for scattering at large angles.

For practical reasons, a single value is needed to quote the effect of the multiple scattering, for instance, its contributions to the angular resolution in this study. A root mean square (rms) value of the scattering angle and its dependence on the momentum of the incident particle and the thickness of the material was first estimated by Rossi and Greisen [182, 183], directly derived from Rutherford scattering. To account for the scattering of cosmic-ray particles in matter, the mean square value of the projected angle is given in the form

$$\langle \theta^2 \rangle_{\text{av}}(t) = \frac{1}{2} E_s^2 \int_0^t \frac{dt'}{(\beta c p)^2},$$

if the energy loss is negligible,

$$\theta^{\text{rms}} = \sqrt{\langle \theta^2 \rangle_{\text{av}}} = \frac{E_s}{\sqrt{2} \beta c p} \sqrt{t}, \quad (5.1)$$

where $E_s = 21$ MeV, t is the thickness of material in radiation lengths, p is the momentum, and βc is the velocity of the particle.

To improve the accuracy of the approximation, a correction factor with the logarithm of the number of radiation lengths was introduced by Highland [184]. Now the Particle Data Group (PDG) uses his formula to approximate the distribution as a simple Gaussian for 98% of the projected angles with a width [50]

$$\sigma = \frac{13.6 \text{ MeV}}{\beta c p} Z \sqrt{X/X_0} [1 + 0.038 \ln(X/X_0)], \quad (5.2)$$

where Z is the charge number of the incident particle, X and X_0 are the thickness and radiation length of the traversed material. Since this formula is a parameterisation of the Molière distribution, the PDG suggests to use this formula in one-go for applications dealing with different layers by finding the total material depth in radiation length ($\sum(X/X_0)$), rather than to add the contributions from individual layers in quadrature. The accuracy of this approximation is considered to be 11% or better for $10^{-3} < X/X_0 < 100$.

Another approach described in [185] claims to have an accuracy of 2% or better. A much better and simpler expression is given in function of the characteristic angles of the Molière theory. However, the computation of these angles is complicated with the mixed materials presented in this study.

The muon multiple scattering as well as all known physics process (energy losses, interactions, decays) could be simulated with Monte Carlo (M. C.) packages, such as GEANT3 and GEANT4, or some dedicated muon propagation codes [53], like MUM [51], MMC [186], etc. The accuracy and speed of the simulation depends on the actual selected model(s). For L3+C the Molière distribution integrated with the GEANT3 program is used. Therefore, the multiple scattering effect in the M.C. data is expected to be overestimated.

5.2 Resolution Function

The main contribution to the angular deviation is the multiple scattering effect in the molasse. For small deviation angles, the distribution of the non-projected (space) and projected (plane) angle can be well approximated by a two (one)-dimensional Gaussian distribution [50]:

$$\frac{dN}{d\Omega} \sim f(\theta_{\text{space}}) = \frac{1}{2\pi\sigma^2} e^{-\frac{\theta_{\text{space}}^2}{2\sigma^2}}, \quad (5.3)$$

$$\frac{dN}{d\theta_{\text{plane}}} \sim f(\theta_{\text{plane}}) = \frac{1}{\sqrt{2\pi}\sigma} e^{-\frac{\theta_{\text{plane}}^2}{2\sigma^2}}, \quad (5.4)$$

where σ is the width of the distribution of a certain data sample, and θ_{space} , θ_{plane} are the deflection angles in space or projected onto a plane. When θ is small, for instance $\theta < 5^\circ$, we can take the approximation, $\theta_{\text{space}}^2 \approx (\theta_{\text{plane},x}^2 + \theta_{\text{plane},y}^2)$, where the x and y axes are orthogonal to the direction of motion, and $d\Omega \approx \pi d\theta_{\text{space}}^2 \approx d\theta_{\text{plane},x} d\theta_{\text{plane},y}$. Deflections into $\theta_{\text{plane},x}$ and $\theta_{\text{plane},y}$ are independent and identically distributed. Replacing $d\Omega$ with $\pi d\theta_{\text{space}}^2$, we obtain,

$$\frac{dN}{d\theta_{\text{space}}^2} \sim f(\theta_{\text{space}}^2) = \frac{1}{2\sigma^2} e^{-\frac{\theta_{\text{space}}^2}{2\sigma^2}}. \quad (5.5)$$

Due to the non-Gaussian distribution of the multiple scattering and the reconstruction problems, the angular resolution distribution cannot practically be fitted to a simple Gaussian distribution. To get a good fit, a mixed double-Gaussian function can be used. The space and projected angular distributions are given by

$$\frac{dN}{d\Omega} \sim f(\theta_{\text{space}}) = f_1 \frac{1}{2\pi\sigma_1^2} e^{-\frac{\theta_{\text{space}}^2}{2\sigma_1^2}} + (1 - f_1) \frac{1}{2\pi\sigma_2^2} e^{-\frac{\theta_{\text{space}}^2}{2\sigma_2^2}}, \quad (5.6)$$

$$\frac{dN}{d\theta_{\text{plane}}} \sim f(\theta_{\text{plane}}) = f_1 \frac{1}{\sqrt{2\pi}\sigma_1} e^{-\frac{\theta_{\text{plane}}^2}{2\sigma_1^2}} + (1 - f_1) \frac{1}{\sqrt{2\pi}\sigma_2} e^{-\frac{\theta_{\text{plane}}^2}{2\sigma_2^2}}, \quad (5.7)$$

where σ_1 and σ_2 are the width of the first and the second Gaussian, and f_1 is the probability of the first Gaussian.

Usually a single value of the angular resolution is used to characterise the performance of a detector. Different definitions exist:

- The RMS value of the double-Gaussian distribution can be expressed by

$$\theta_{\text{plane}}^{\text{rms}} = \sqrt{f_1\sigma_1^2 + (1 - f_1)\sigma_2^2}. \quad (5.8)$$

It's a good value to represent the performance of the event selection criteria since the large tail of the distribution, which is sensitive to the selection, is included.

- The Half Width at Half Maximum (θ^{HWHM}) of the 1D projected angle distribution or the 2D space angle distribution. This definition is usually used in point-like source searches.
- The SOUDAN [187] experiment fitted the angular distribution ($dN/d\theta^2$) with a Gaussian in a small angular range and the long tail was simply ignored.
- MACRO [188] and PACT [189] choose the cone of angle $\theta_{68\%}$ that contains 68% of the events from a point-like source. This method could be independent from any fit function, but the result is sensitive to the tail of the distribution. Moreover, TIBET III [190] use $\theta_{50\%}$ and HEGRA [191] use $\theta_{63\%}$ instead of the more popular $\theta_{68\%}$.

For a single-Gaussian distribution, all the definitions are consistent.

$$\sigma = \theta_{\text{plane}}^{\text{rms}} = \frac{1}{\sqrt{2}}\theta_{\text{space}}^{\text{rms}} = \frac{1}{1.177}\theta_{\text{plane}}^{\text{HWHM}} = \frac{1}{1.177}\theta_{\text{space}}^{\text{HWHM}} = \frac{1}{\sqrt{2}}\theta_{63\%} = \frac{1}{1.2}\theta_{50\%}. \quad (5.9)$$

But for double-Gaussian or more complicated distributions, there are no simple relations between all these numbers. The choice depends on the application. When searching for a weak signal or anti-signal in a high background level, the tails of the angular distribution may be spread and hidden into the background. Therefore, in this case, the narrow Gaussian from the double-Gaussian fit, or the HWHM angle should be a good parameter to describe the angular resolution.

5.3 An unbinned maximum likelihood method

The angular resolution of muons depends on their momenta, arriving direction, thickness of matter traversed, and detector conditions. So an unbinned maximum likelihood analysis is

favoured to take into account all the effects as much as possible. Using the simple Gaussian approximation, the likelihood function can be constructed as:

$$\mathcal{L}(\sigma) = \prod_{i=1}^N \frac{\frac{dN}{d\theta_{\text{space}}^2}(\theta_i^2; \sigma)}{\int_0^{\theta_0} \frac{dN}{d\theta_{\text{space}}^2}(\theta_{\text{space}}^2; \sigma) d\theta_{\text{space}}^2},$$

where θ_i is a series of measured space angle in the data sample, θ_0 is the considered fit range, and σ is the trial value of the angular resolution which will be determined by maximising the function and can itself be a function of other quantities. When fitting a sample over a large energy range, etc, it's better to let θ_0 vary at the event level, depending on the properties of the muon, such as the momentum, thickness of matter traversed, etc. The log-likelihood function is thus,

$$\ln \mathcal{L}(\sigma) = - \sum_{i=1}^N \left[\frac{\theta_i^2}{2\sigma^2} + 2 \ln \sigma + \ln(1 - \exp(-\frac{\theta_{0,i}^2}{2\sigma^2})) \right], \quad (5.10)$$

where the terms independent of the free parameters have been dropped. The $-\ln \mathcal{L}(\sigma)$ is minimised numerically with the MINUIT minimisation package [192] integrated in the ROOT framework [193].

5.4 The detector's intrinsic resolution

According to the muon-chamber resolution described in Section 4.4.3, we can conclude that the main contribution from the detector is the inter-octant alignment (which is about 0.06°). In addition, the angular resolution also relies on the precision of the reconstruction, which depends on the quality of the track, i.e. total number of hits, the position in the detector, the background, etc.

Studies carried out with M.C. simulation at very high energies indicate that the overall angular resolution limited by the detector and the reconstruction is $\sigma = 0.1^\circ$ [121].

5.5 Angular distribution of secondary muons at surface level

5.5.1 Shower simulation with CORSIKA

CORSIKA (see Section 1.4.4 and [63]) is employed to simulate the air showers induced by protons and helium nuclei. Different high energy hadronic interaction models (VENUS, QGSJET, DPMJET, SIBYLL and HDPM) combined with low energy (< 80 GeV) models FLUKA or GHEISHA have been used. A variety of options allow to customising the simulation. All the none-default options are shown in Table 5.1. To understand the muon production angle and the multiple scattering effect, the Earth magnetic field is switched off for all simulations described in this section.

Figure 5.1 shows the comparison of simulated muon energy distributions from protons or helium nuclei induced air showers. Only a marginal difference can be seen at high energy. On

Table 5.1: Steering of the CORSIKA simulation (only the none-default options are given)

Keyword	Value	Comments
ESLOPE	-2.7	Slope of primary energy spectrum
ERANGE	1.E2, 1.E6	Energy range of primary particle [GeV/nucleon]
THETAP	0, 60	Range of zenith angle [degrees]
OBSLEV	449.E2	Observation level [cm]
MAGNET	0.0001, 0.0001	Magnetic field. (OFF)
ECUTS	30, 30, 30, 30	Energy cuts for secondary particles (hadrons, muons, electrons, photons) [GeV]

the other hand the energy distributions of primary particles for different muon energy ranges are shown in Figure 5.2. Again the differences are negligible.

Figure 5.3 presents a comparison of the angular distribution of muons originating from protons and helium nuclei in the momentum range of 70 – 80 GeV/c. The fitted results show no difference between protons and helium nuclei induced air showers. Therefore, I mainly use protons as primary particles for the angular resolution study. Anyhow, helium and heavier nuclei represent only 27% of the contribution to the muon flux at the energies of interest here (see Section 6.3.2).

5.5.2 Angle between muons and primaries

The simulations were performed with different high energy hadronic interaction models (HDPM, DPMJET, QGSJET, SIBYLL or VENUS) combined with the low energy interaction models FLUKA or GHEISHA.

To understand the dependence of the angular distribution, one of the simulated data samples is divided into small intervals of momentum or zenith angle of secondary muons at surface level. The rms value of the distribution in each interval is determined and presented in Figure 5.4. The momentum dependence plot (Figure 5.4(a)) can be fitted to the following function

$$\theta_{\text{plane}}^{\text{rms}}(p_{\mu}) = \sigma_0 \cdot \left(\frac{100 \text{ GeV}}{cp_{\mu} + \langle E_{\text{loss}} \rangle / 2} \right)^n. \quad (5.11)$$

The parameters obtained from the fit are $\sigma_0 = 0.175^{\circ} \pm 0.002^{\circ}$, the width of the angular distribution at 100 GeV/c, $\langle E_{\text{loss}} \rangle = 4.4 \pm 1.8 \text{ GeV}$, the average energy loss of muons, and $n = 0.91 \pm 0.02$ indicating the degree of the momentum dependence. Further analysis shows that an additional momentum-independent term is not necessary.

On the other hand, the dependence on the zenith angle is rather weak. Only in the lowest momentum interval, the width of the angular distribution is observed to decrease at large zenith angles. The inclined muons loose more energy than the vertical ones, therefore, they must have a higher momentum at the creation point and thus originate from earlier genera-

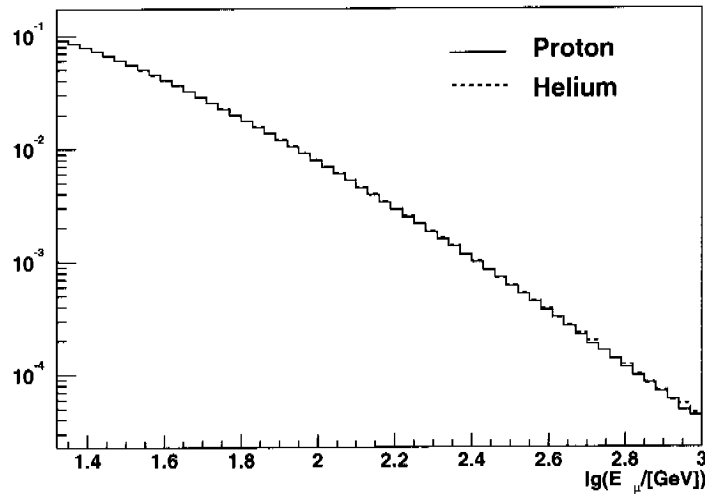


Figure 5.1: Muon energy distribution simulated with CORSIKA with the hadronic model VENUS. The energy range of primary particles is 0.1 – 1000 TeV per nucleon with a power law distribution of index -2.7. The slope of the distribution becomes steeper at high energies, ranging from -2.6 to -3.4.

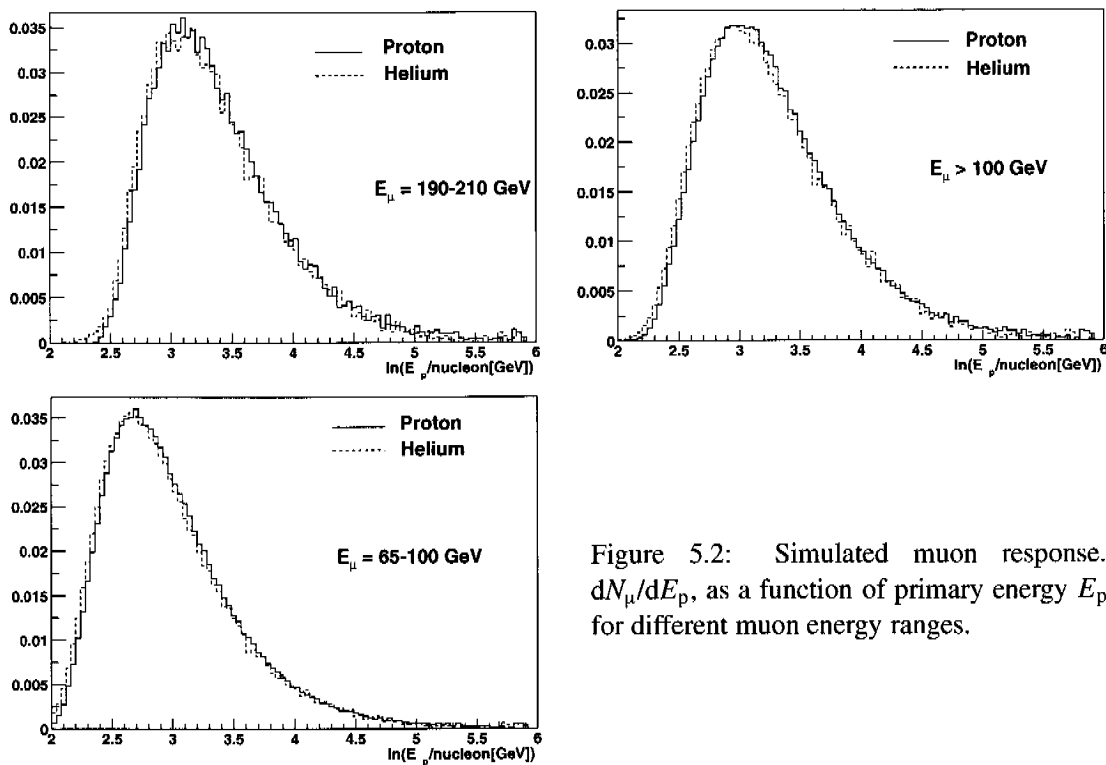


Figure 5.2: Simulated muon response. dN_{μ}/dE_p , as a function of primary energy E_p for different muon energy ranges.

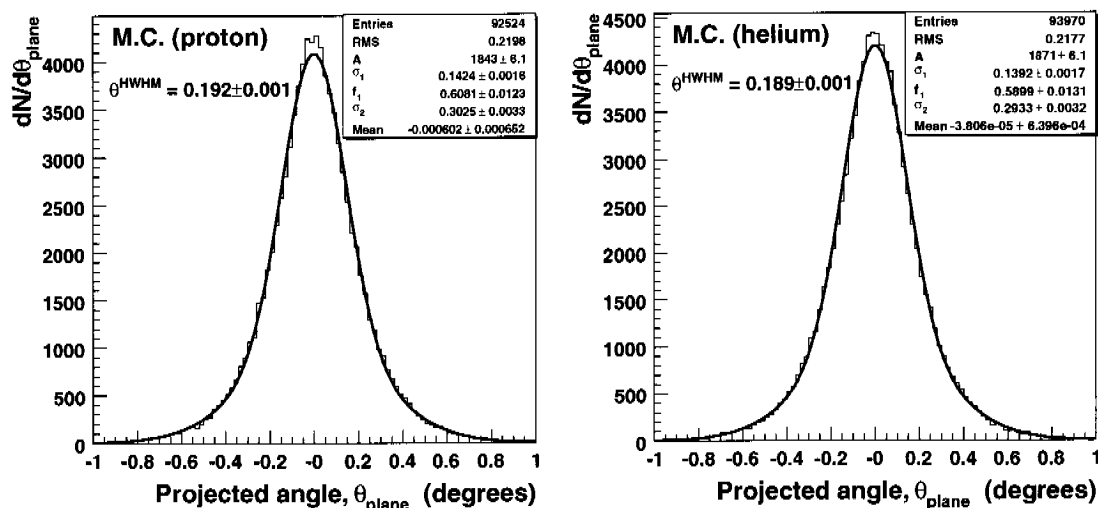


Figure 5.3: Distribution of the space angle between muons and their primary particles at surface level for M.C. events (CORSIKA Ver. 6.2 with QGSJET+FLUKA) with muon momenta between 70 and 80 GeV/c. The solid lines indicate the best-fit curves obtained by fitting to equation (5.6). The HWHM values are determined from the fit results.

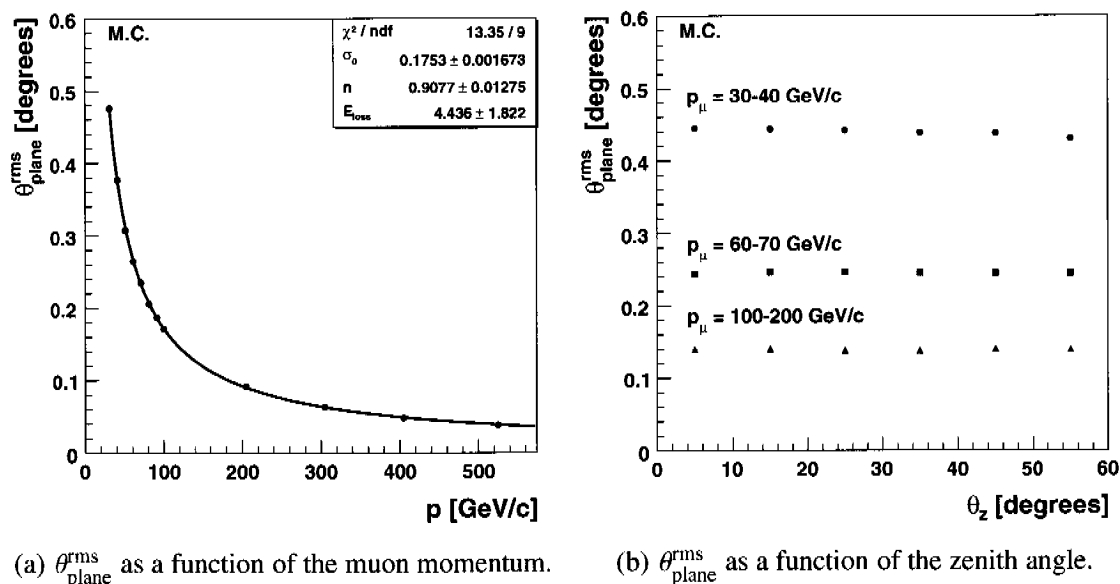


Figure 5.4: The width of the angular distribution of muons at surface level as a function of momentum and zenith angle. The M.C. data sample is produced with CORSIKA, using the hadronic model QGSJET. 8×10^6 primary protons with a spectral index of -2.7 and energy between $10^2 - 10^6$ GeV are generated uniformly.

tions of the cascade interactions with smaller production angles. Since the radiation length of the atmosphere is rather large ($\sim 36.6 \text{ g/cm}^2$), the influence of multiple scattering is surpassed by the higher initial momenta.

To take into account the effect of the zenith angle dependent energy loss, an unbinned maximum likelihood method is the best choice. The width of the distribution of muons with given momentum p and zenith angle θ_z can be written in the form

$$\sigma_{\text{trial}}(\sigma_0, n, E_{\text{loss}}) = \sigma_0 \cdot \left(\frac{100 \text{ GeV}}{cp_\mu + E_{\text{loss}} / \cos \theta_z / 2} \right)^n, \quad (5.12)$$

where σ_0 is the angular resolution for vertical muons with momenta of $100 \text{ GeV}/c$, E_{loss} is the total energy loss for vertical muons. Inserting this expression to equation (5.10) we obtain a log-likelihood function on σ_0 , n and E_{loss} ,

$$\ln \mathcal{L}(\sigma_0, n, E_{\text{loss}}) = - \sum_{i=1}^N \left[\frac{\theta_i^2}{2\sigma_{\text{trial}}^2} + 2 \ln \sigma_{\text{trial}} + \ln \left(1 - \exp \left(-\frac{\theta_{0,i}^2}{2\sigma_{\text{trial}}^2} \right) \right) \right],$$

where the event dependent fitting range is set to be $\theta_{0,i} = 5 \cdot \theta_{\text{plane}}^{\text{rms}}(p_\mu)$, which is determined from the expected value based on equation (5.11).

The unbinned distributions produced by CORSIKA with various interaction model configurations for different primary particles are fitted to this function. The results are summarised in Table 5.2 and exhibited in Figure 5.5. The obtained values of the energy loss for vertical muons are consistent with the expected value ($\sim 2.5 \text{ GeV}$).

Figure 5.5(a) shows the simulated results with the same interaction models (QGSJET + FLUKA) for primary protons with spectral index of -3.7, -3.2, -2.7, -2.2, and -1.7, as well as helium and iron nuclei with a spectral index of -2.7. Only a slight difference is observed. This fact indicates that the angular deviation with respect to the primary particle depends mainly on the muon momentum, but not on the type of the primary particle and its energy distribution. However, the muons produced by gammas behave differently (Table 5.2), having a smaller angular deviation than those initiated by charged particles.

Figure 5.5(b) indicates that there are large discrepancies between different interaction models ($\sim 20\%$ at $30 \text{ GeV}/c$). According to the test performed for the KASCADE experiment [194], the QGSJET model describes the muon lateral distribution best. The low energy model FLUKA is also considered to be better than GHEISHA [195]. Since the angular distribution has a close correlation with the lateral distribution, we can ‘trust’ the values obtained from the simulation with QGSJET and FLUKA models, and use the following parameterisation of the muon angular distribution for future analyses,

$$\sigma_{\text{EAS}} = \left(\frac{0.155 \text{ GeV}}{cp_\mu + 1.25 \text{ GeV} / \cos \theta_z} \right)^{0.9}. \quad (5.13)$$

This is about four times larger than the value of the multiple scattering estimated with equation(5.2). This manifests that the muon angular deviation in the atmosphere is dominated by the production angle determined by the hadronic interactions.

Table 5.2: Muon angular distribution parameters obtained from CORSIKA simulations. The M.C. data samples are fitted to function (5.12), using an unbinned maximum likelihood method.

Primary particle	Spectral index	Interaction models	#generated	#muon	σ_0 (degrees)	n	E_{loss} (GeV)
proton	-3.7	QGSJET+FLUKA	8×10^6	729896	0.170	0.898(3)	1.8(2)
proton	-3.2	QGSJET+FLUKA	8×10^6	1105489	0.171	0.895(2)	1.9(2)
proton	-2.7	QGSJET+FLUKA	8×10^6	1998425	0.170	0.903(1)	2.5(1)
proton	-2.2	QGSJET+FLUKA	8×10^6	5225849	0.170	0.905(1)	2.5(1)
proton	-1.7	QGSJET+FLUKA	8×10^5	3031721	0.170	0.910(1)	2.6(1)
helium	-2.7	QGSJET+FLUKA	2×10^6	2015263	0.169	0.899(1)	2.3(1)
iron	-2.7	QGSJET+FLUKA	3×10^5	4247060	0.167	0.894(1)	1.7(9)
proton	-2.7	QGSJET+GHEISHA	8×10^6	2023733	0.171	0.939(1)	2.5(1)
proton	-2.7	VENUS+FLUKA	8×10^6	2199489	0.179	0.930(1)	3.2(1)
proton	-2.7	SIBYLL+FLUKA	8×10^6	2244546	0.162	0.930(1)	2.1(1)
proton	-2.7	DPMJET+GHEISHA	8×10^6	2190360	0.187	0.918(1)	3.4(1)
proton	-2.7	HDPM+FLUKA	8×10^6	2105626	0.221	0.931(1)	4.6(1)
proton	-2.7	HDPM+GHEISHA	8×10^6	2135994	0.220	0.949(1)	4.3(1)
gamma	-2.7	QGSJET+FLUKA	4×10^7	93974	0.151	0.945(6)	2.7(5)

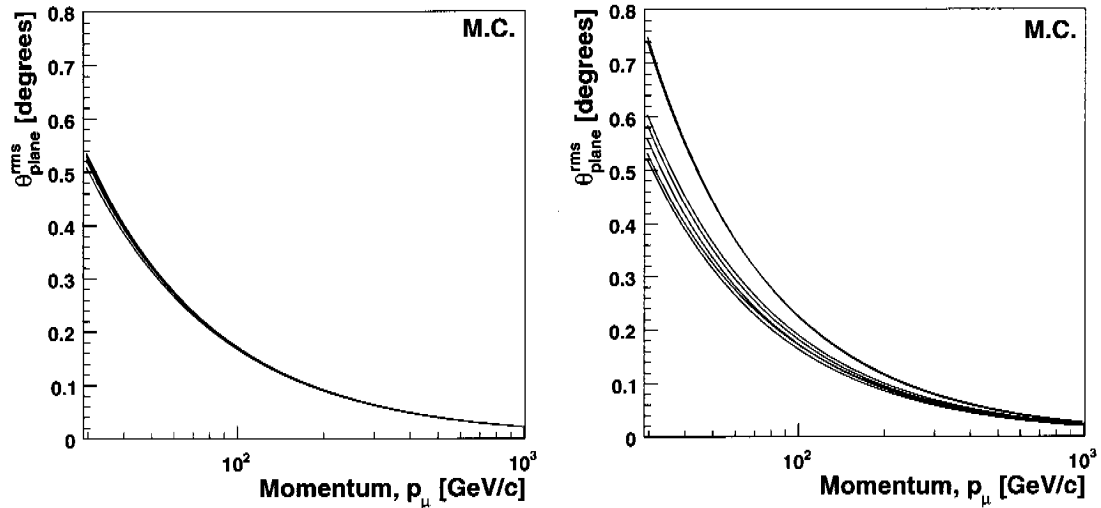
5.5.3 Angle between secondary muons

L3+C (without the surface scintillator array) has no means to determine the direction of the shower core, neither a bright source could be used to verify the detector's angular resolution. But the resolution can be determined in the Moon shadow analysis (see Chapter 6) with some uncertainty. Still another possibility is to measure the angular distributions between muons coming from the same air showers.

Figure 5.6(a) shows the distance between secondary muons at the surface and Figure 5.6(b) shows the relation between the angle and distance of secondary muons. The distance between secondary muons could reach 1000 meters or more with large opening angles. But the size of the L3+C detector is only 10 meters. Applying this distance cut, only a few of the multiple muons with small opening angles can be detected.

The two muons from the same shower are considered to be statistically independent and have identical distributions described by function (5.12). Therefore, the width of the distribution of the double-muon angle is simply the square root of the quadratic sum of the width of the individual distributions. A similar unbinned maximum likelihood method is applied on simulated showers with more than one muon. Table 5.3 summarises the results obtained from simulations performed with interaction models QGSJET and FLUKA.

The parameters (σ_0 , n , E_{loss}) determined from the double muon events without surface distance cut are consistent with the results obtained from the distribution between muons and primary particles. This verifies the assumption that the muons from same showers are statis-



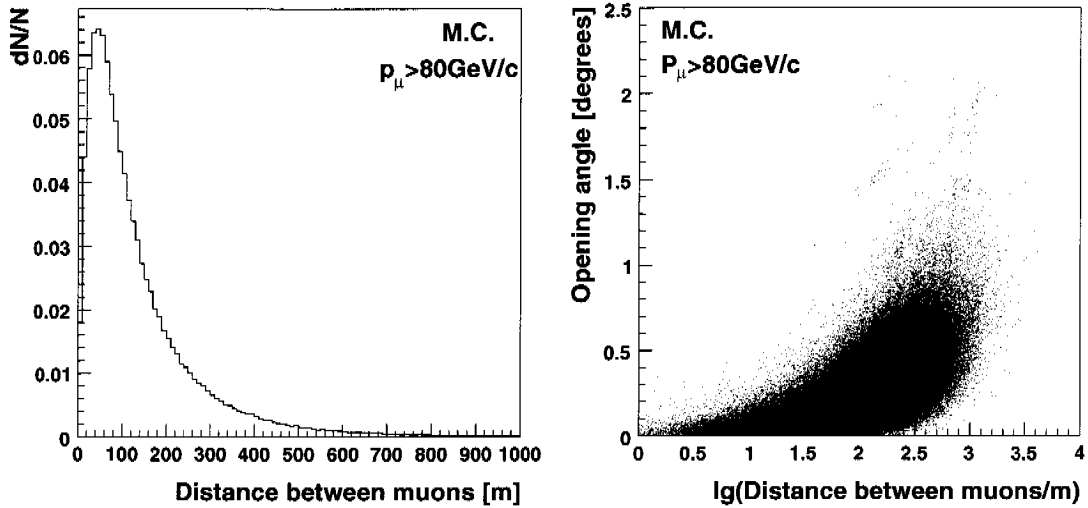
(a) Simulations with interaction models QGSJET and FLUKA for primary protons with different energy distributions, as well as helium and iron nuclei. (b) Simulations with different interaction models for primary protons with a spectral index of -2.7 . From top to bottom the model combinations are: HDPM+GHEISHA/FLUKA, DPMJET+GHEISHA, VENUS+FLUKA, QGSJET+GHEISHA, QGSJET+FLUKA, and SIBYLL+FLUKA.

Figure 5.5: The mean angular deviations for vertical muons. This is a graphical representation of the values listed in Table 5.2.

Table 5.3: Angular distribution parameters determined from double-muon events with or without distance cut. The parameter E_{loss} has been fixed to the expected value (2.5 GeV) for events with distance cut, because it becomes fragile due to the low statistics.

Primary particle	#generated	No distance cut				Distance < 10 m		
		#events	σ_0 (degrees)	n	E_{loss} (GeV)	#events	σ_0 (degrees)	n
p (-2.7)	8×10^7	8080096	0.179	0.904(1)	1.2(1)	169778	0.050	0.885(2)
p (-2.2)	8×10^6	2002673	0.177	0.909(2)	1.0(1)	257717	0.053	0.900(1)
p (-1.7)	8×10^6	28107230	0.177	0.913	1.1	6165746	0.055	0.896
He (-2.7)	8×10^6	1407382	0.178	0.899(1)	1.3(1)	51124	0.053	0.897(4)
Fe (-2.7)	3×10^6	42131580	0.175	0.887(1)	0.7	5225004	0.055	0.917

tically independent. It also indicates that the distribution parameters for single muons could be determined from double muon data directly. If we apply a distance cut of 10 m, the double



(a) Distribution of distances between secondary muons at the surface. (b) The space angle between secondary muons as a function of their distance.

Figure 5.6: Angle between secondary muons and its relation to their relative distance at the surface.

muon angle becomes much smaller. Due to the low statistics, the parameter E_{loss} becomes fragile, so it has to be fixed to the expected value (2.5 GeV) in the maximum likelihood fit. Comparing to the large deviation due to the multiple scattering in the molasse above the L3+C detector, the detectable double muons have nearly parallel paths at the surface.

5.6 Double-muon data

5.6.1 The double-muon data sample

There are 1.75×10^8 events in good data runs having more than one muon track reconstructed. This number amounts to 1.9% of the total number of events and corresponds to an average multi-muon event rate of 8.1 s^{-1} . The same selection criteria (see Sec. 4.3) are applied to each muon track. Besides the “real” double-muon events, there are several kinds of fake double-muon events. Therefore, additional requirements have to be considered.

Chance coincidence from different showers

The chance coincidence rate can be simply estimated from the width of the trigger window, the average trigger rate and the trigger rate corrected for the dead-time:

$$\text{Year 1999: } 436.4 \text{ s}^{-1} \times 4.4 \mu\text{s} \times 445.0 \text{ s}^{-1} = 0.85 \text{ s}^{-1} \quad (0.20\%),$$

$$\text{Year 2000: } 418.0 \text{ s}^{-1} \times 4.4 \mu\text{s} \times 423.8 \text{ s}^{-1} = 0.78 \text{ s}^{-1} \quad (0.19\%).$$

This concerns about 10% of the total double-muon events. The angle between them should be randomly distributed. Requiring the opening angle to be less than 5° , the ratio of the chance coincident double-muon events reduces to $\sim 2 \times 10^{-4}$. Such kind of events can therefore be neglected.

Mismatched subtracks

Occasionally, when a muon crossed two octants, the two sub-track may fail to be matched to one track. These events can be distinguished from their separation distance on the $x - z$ plane in the L3 coordinate system, or from the position of the vertex of the two tracks.

Figure 5.7 shows the distance distribution of a subset of the data. Comparing to Figure 5.6(a), one concludes that events with a separation less than 0.1 m must correspond to mismatched single muon events.

Practically the muon can not be back-tracked to the interaction point of the primary particle in the atmosphere. Here we define the place where the two tracks have the minimum distance as the *apparent vertex*. Figure 5.8(a) shows the distribution of the height of the apparent vertex. It is nearly symmetric about the centre of the detector. It can be well fitted to a Breit-Wigner function (the central part has been excluded from the fit). Somehow, the small positive mean value of the distribution weakly indicates that the muons are coming from the upper side of the detector. The central part of the distribution significantly deviates from the expected distribution. From Figure 5.8(b), we recognise that these events might be mismatched single muon events, because most of them have an apparent vertex inside of the detector. This leads to another additional cut: the apparent vertex is required to be located at least 10 m away from the centre of the detector.

In total 3.49×10^6 double-muon events with momenta larger than 30 GeV/c are selected.

5.6.2 Maximum likelihood analysis

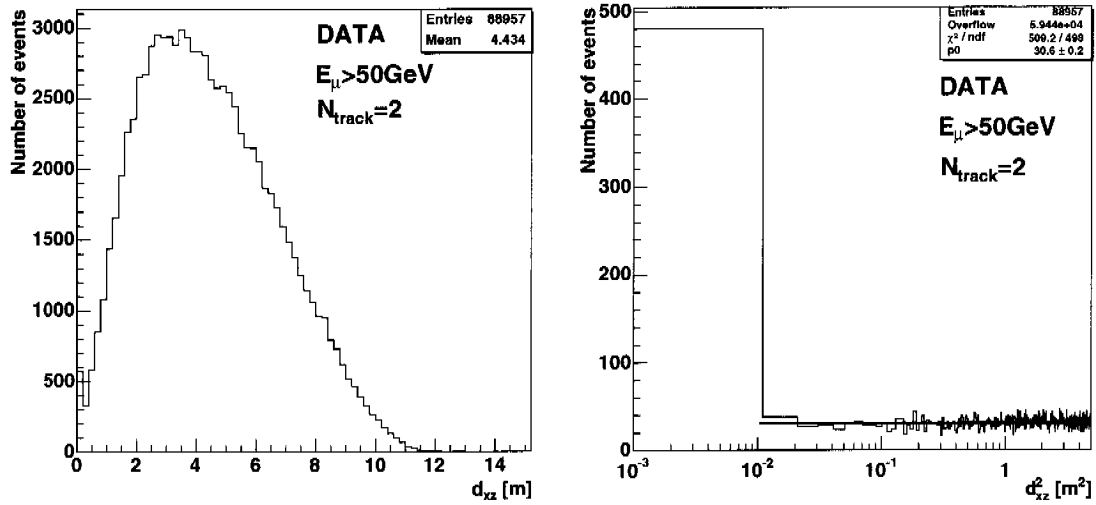
According to the discussion presented in the previous section, the experimental angular resolution is assumed to be a quadratic sum of two terms,

$$\sigma = \sqrt{\sigma_{\text{ms}}^2 + \sigma_{\text{in}}^2}, \quad (5.14)$$

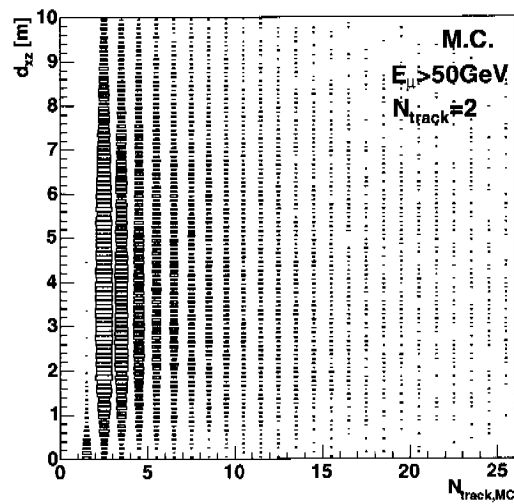
where σ_{ms} is the contribution from the multiple scattering effect having the shape of function (5.2) and depends on the muon momentum and the thickness of matter traversed. σ_{in} is the detector's intrinsic resolution which is momentum independent. Simulations suggest that muons from the same air shower are distributed independently and identically (see Section 5.5.3). Adding a free scale parameter k to the multiple scattering terms, the width of the double-muon distribution can be written in the form

$$\sigma_{\text{trial},\mu\mu} = \sqrt{k^2(\sigma_{1,\text{ms}}^2 + \sigma_{2,\text{ms}}^2) + 2 \cdot \sigma_{\text{in}}^2}, \quad (5.15)$$

where k and σ_{in} will be determined with the maximum likelihood analysis.

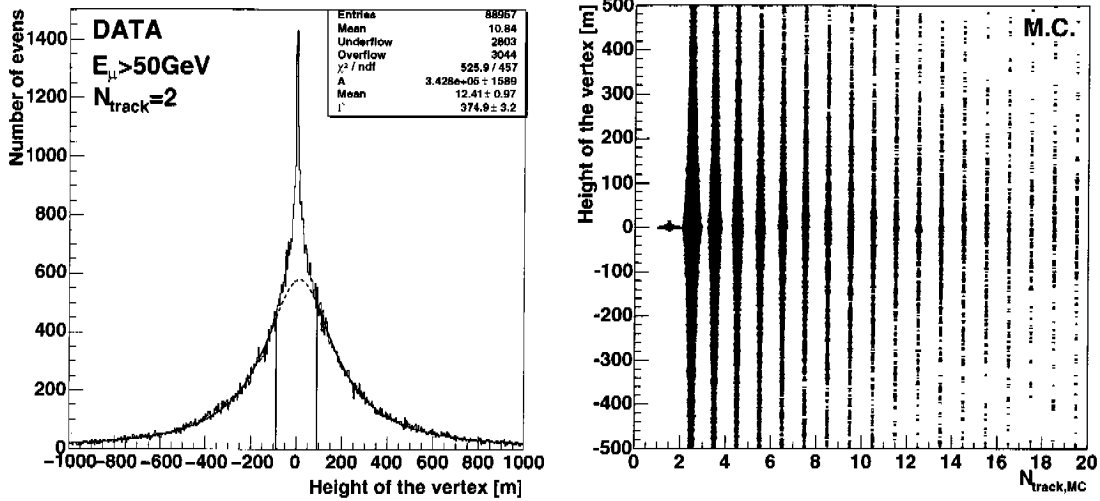
(a) The separation on the $x - z$ plane.

(b) Square of the separation.



(c) Separation as a function of the number of generated muons.

Figure 5.7: Distance between muons on the $x - z$ plane of the L3 coordinate system.



(a) Distribution of the height of the apparent vertex. (b) Vertex as a function of the number of generated muons

Figure 5.8: The height of the apparent vertex in the L3 coordinate system.

Taking the significant energy loss through the molasse into account, the multiple scattering term can be written in the form

$$\sigma_{i,ms} = \frac{13.6 \text{ MeV}/c}{(p_i^{\text{surf}} + p_i^{\text{det}})/2} \sqrt{x_i/X_0(1 + 0.038 \ln(x_i/X_0))},$$

where p_i^{det} is the measured muon momentum, p_i^{surf} is the momentum at the surface level determined with the back tracking algorithm (see Section 3.3), x_i is the total thickness of the matter traversed by the muon, and $X_0 = 26.5 \text{ g/cm}^2$ is the average radiation length of the molasse. Inserting these two expressions into equation (5.10), a log-likelihood function of k and σ_{in} is obtained,

$$\ln \mathcal{L}(k, \sigma_{\text{in}}) = - \sum_{i=1}^N \left[\frac{\theta_{i,\mu\mu}^2}{2\sigma_{\text{trial},\mu\mu}^2} + 2 \ln \sigma_{\text{trial},\mu\mu} + \ln(1 - \exp(-\frac{\theta_{0,i}^2}{2\sigma_{\text{trial},\mu\mu}^2})) \right], \quad (5.16)$$

where the fitting range $\theta_{0,i}$ is set to be 5 times the value determined from equation (5.15) with $k = 1$ and $\theta_{\text{in}} = 0.1^\circ$ for each event. The results obtained by fitting the double-muon data to this function are listed in Table 5.4.

The measured intrinsic resolution of the detector is comparable to the previously estimated value (see Section 5.2). The momentum and matter depth (direction) dependent term is slightly larger ($\sim 5\%$) than the value predicted by the Molière theory (see Section 5.1). Taking into account the uncertainty of the matter depth measurement due to the complex environment and the fact that the muons at surface level are not exactly parallel, the result

Table 5.4: The angular resolution determined from the double-muon data using the unbinned maximum likelihood method. Each individual muon has a momentum greater than 30 GeV/c at the surface level, and passes all the quality cuts described in Section 4.3 as well as the additional cuts for double muon events.

Year	Entries ($\times 10^6$)	The scale of the multiple scattering contribution, k	Detector's intrinsic resolution, σ_{in} [degrees]
1999	1.09	1.056 ± 0.001	0.090 ± 0.001
2000	2.40	1.056 ± 0.001	0.092 ± 0.001

is reasonable. The two resolution components determined from the double-muon data can therefore be parameterised as

$$\sigma_{\text{ms}} = \frac{28.7 \text{ MeV}/c}{p^{\text{surf}} + p^{\text{det}}} \sqrt{x/X_0} (1 + 0.038 \ln(x/X_0)), \quad (5.17)$$

and

$$\sigma_{\text{in}} = 0.091^\circ. \quad (5.18)$$

5.7 Summary

The angular resolution and its dependences have been studied with M.C. simulation and double-muon data. Considering the three main components of the resolution, the angular resolution can be parameterised as

$$\sigma_{\text{total}} = \sqrt{\sigma_{\text{EAS}}^2 + \sigma_{\text{ms}}^2 + \sigma_{\text{in}}^2}, \quad (5.19)$$

where σ_{EAS} , σ_{ms} and σ_{in} are given by equation (5.13), (5.17) and (5.18) respectively.

The individual components and the total angular resolution for vertical muons are presented in Figure 5.9. For low energy muons (less than 100 GeV), the resolution is dominated by the multiple scattering and the production angle in the parent hadronic interactions, while for high energy muons the resolution is limited by the detector's intrinsic resolution and the reconstruction precision.

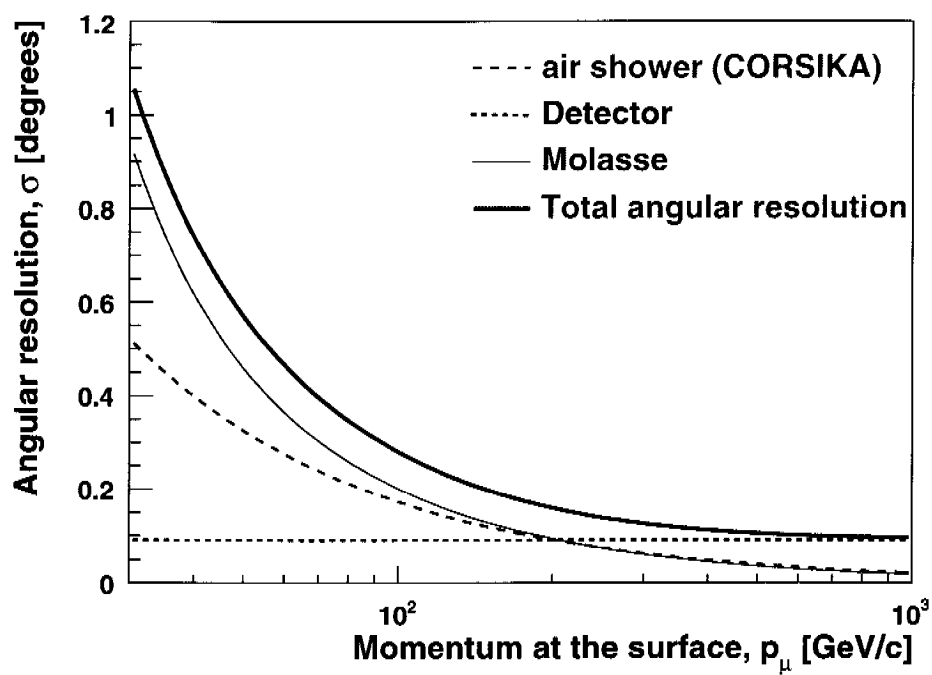


Figure 5.9: The angular resolution for vertical muons and its dependence on the value of momentum at the surface level.

Chapter 6

The Moon shadow analysis

In 1957, it was pointed out that the Moon and the Sun could cause shadows in the cosmic ray flux and the observation of the shadowing effects might provide information about the magnetic field near these bodies [196]. But at that time no experiment had the necessary good angular resolution to perform this measurement.

Before the first explicit Moon-shadow image was observed by the CYGNUS [197] collaboration in 1991, a method to search antimatter with the Moon shadow was proposed [198]. The shadow of cosmic rays (most are positively charged particles) is deflected by the Earth magnetic field, therefore the ratio of antimatter in cosmic flux can be estimated by comparing the number of deficit particles from the different sides of the Moon.

This chapter will give a summary of the past observations. A methodological description on the Moon shadow observation, the Monte Carlo study, the Moon shadow analysis, and an antiproton search follows.

6.1 The Moon shadow observations

Table 6.1 summarises the Moon (Sun) shadow observations performed by different experiments. The techniques used in these observations have been described briefly in Chapter 1.

In the early 1990s, three scintillator arrays CYGNUS [197], CASA-MIA [199] and HEGRA [191], which were designed mainly for high energy gamma-ray astronomy, observed the Moon and Sun shadowing effects in the primary cosmic ray flux at energies above 50 TeV. The deflection of primary cosmic rays by the Earth magnetic field and even the IMF field can be neglected at such high energies. Therefore, the angular resolution and the pointing precision of the detector can be directly derived from the sharpness and the shift of the shadow respectively.

Nearly at the same time, the Moon and Sun shadow were also observed at lower energies (~ 10 TeV) by the TIBET air shower array with data accumulated during 1991 to 1993 [200]. The Moon shadow was centred at the apparent position in the north-south direction, where the geomagnetic effect can be neglected. On the other hand, the shadow was shifted towards the west by 0.14° in the east-west direction. This deflection, which was comparable with

Table 6.1: Summary of Moon shadow observations.

Experiment	DAQ period	Detector	Primary energy [TeV]	Angular resolution ^a [degrees]	Significance ^b [s.d.]
CYGNUS	1986–1990	scnt. array	~ 50	$0.75^{+0.13}_{-0.09}$	4.9(M+S)
CASA	1990–1991	scnt. array	~ 100	$0.54^{+0.10}_{-0.07}$	4.7(M), 4.8(S)
HEGRA	1990–1993	scnt. array	~ 50	0.58 ± 0.07	6.0
TIBET AS γ	1990–1991	scnt. array	~ 10	$0.87^{+0.13}_{-0.10}$	5.8(M), 3.7(S)
TIBET III	1999–2004	scnt. array	~ 3	0.9	40
Milagrito	1997–1998	water-Č	~ 3	0.9	10
Milagro	1999–2003	water-Č	~ 0.7	0.75	33.5
ARTEMIS	1996–1997	IACT	> 3.7		
CLUE	1998–2000	IACT	~ 1	~ 0.8	
MACRO	1989–2000	μ -tracking	~ 20	0.55 ± 0.05	6.5(M), 4.6(S)
SOUDAN 2	1989–1998	μ -tracking	~ 15	~ 0.29	5
L3+C	1999–2000	μ -spectro.	(see the following chapters)		

^aDifferent definitions exist. All the numbers listed in this table have been converted to the standard deviation assuming a single Gaussian distribution with the help of Equation (5.9).

^bLegend: M: Moon, S: Sun.

the systematic pointing error of 0.2° and much smaller than the angular resolution, somewhat weakly indicated the effect of the geomagnetic field. The Sun shadow observed in the same period, was displaced 0.7° east and 0.4° south to the apparent position of the Sun. The influence of the solar and the interplanetary magnetic field and the difference from the “towards” and “away” sectors of the IMF were clearly shown [201]. By comparing the number of events at the symmetric position of the Sun shadow, an upper limit of the \bar{p}/p ratio was set to be 22% at 10 TeV [202].

With the upgraded TIBET air shower array, the TIBET-III, the significance of the Moon shadow has been observed to be 40σ [203]. Its energy threshold has been lowered to about 2 TeV, however, the angular resolution is still at the same level of 0.9° . The shift of the shadow due to the geomagnetic field is reported to be 0.23° west at a mean energy of ~ 3 TeV and the upper limit of the \bar{p}/p ratio is claimed to be 0.05 at 90% C.L., without giving details of the analysis.

The Milagro collaboration lowered the energy threshold of the EAS observation down to a few 10^2 GeV with a water-Cherenkov detector array, and achieved a slightly better angular

resolution ($\sim 0.75^\circ$) compared to the TIBET-III experiment. The shadowing effect of the Moon and the Sun as well as the effect of the magnetic fields have been observed with two years data of Milagrito [204, 205], the prototype of Milagro, and four years data of Milagro [206]. A 95% C.L. upper limit of the \bar{p}/p ratio of 0.17 was derived with the Moon shadow data of Milagrito at a median energy of 2.7 TeV [205].

Another technique which has been used for Moon shadow searches, is the Imaging Atmospheric Cherenkov Technique (IACT), which also has a low energy threshold. A dedicated antimatter searching experiment, the antimatter research through the earth moon ion spectrometer (ARTEMIS) had been established at the Whipple 10 m Imaging Atmospheric Cherenkov Telescope [207]. Due to the “strong” Moon light, the observation can only work in the UV band, so a special filter was developed to protect the Moon light. However, the observation failed because the imaging technique effectively could not be used in the UV band due to too few photons produced in this wave band. The CLUE experiment [208] which tried the same technique, also did not publish any reliable result due to the same reason.

The shadowing effect of the Moon and Sun has also been observed with deep underground muon experiments. Due to the low muon flux limited by the thick overburden, MACRO [188, 209] and SOUDAN-2 [187] had to accumulate about ten years data to obtain a clear shadow image with significance between 5 and 7. MACRO obtained an upper limit of the \bar{p}/p ratio of 52% (90% C.L.) using the Sun shadow data for primaries at a mean energy of about 20 TeV. In addition, a day-night effect to the Moon shadow was observed by the MACRO experiment: the shadow observed during the night is shaper and more significant. Probably the cause was due to the different configuration of the geomagnetic field in the two sides.

The L3+C experiment, as a precise muon spectrometer installed at a shallow depth underground, has the potential to observe a clear geomagnetic effect to the Moon shadow and to obtain a better limit on the \bar{p}/p ratio with an offline adjustable low energy threshold and a good angular resolution.

6.2 Method

6.2.1 Coordinate systems

The horizontal system (θ_z, ϕ_z): This is a fixed system (with respect to the Earth) centred on the detector. The *zenith* angle θ_z is measured from 0° to 180° from the geographical vertical (the zenith), and the *azimuth* angle ϕ_z is measured from 0° to 360° along the horizon plane from the North towards the East (See Figure 6.1).

The equatorial system ($\delta, \alpha/h$): To describe astronomical objects, an equatorial coordinate system is more convenient. Its reference plane, the celestial equator, is parallel to the equatorial plane, and the z -axis is parallel to the rotation axis of the Earth respectively (See Figure 6.2). The *declination* δ of a source is measured from the reference plane to the North ($0, 90^\circ$) or to the South ($0, -90^\circ$). The second coordinate, is measured along the celestial equator and there are two conventions to represent this angle. One

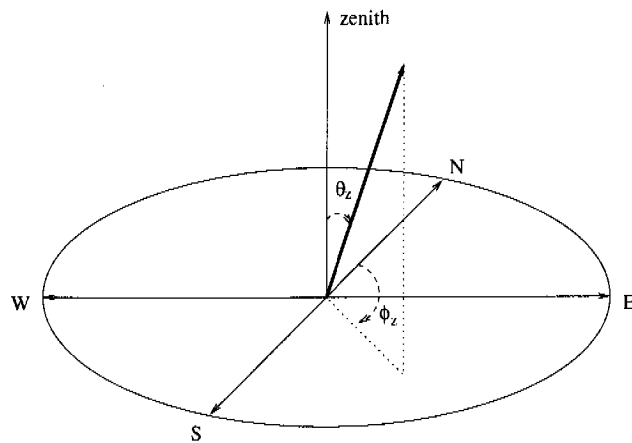


Figure 6.1: The horizontal system.

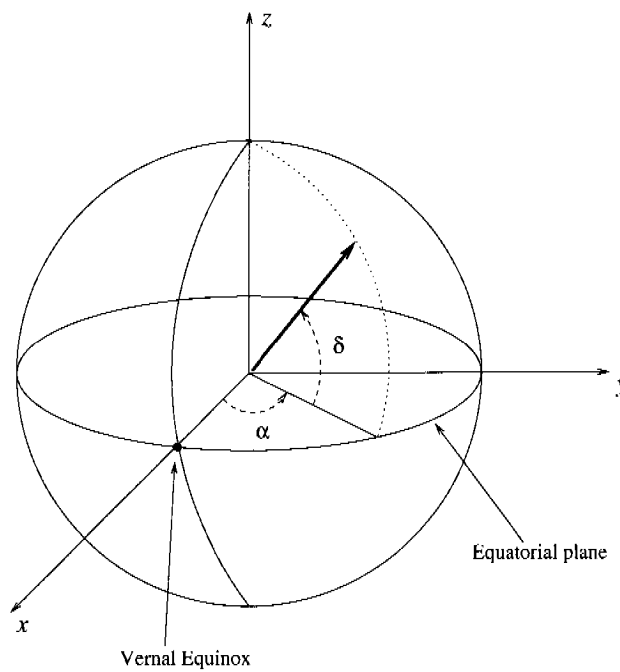


Figure 6.2: The equatorial system.

of them is called *hour angle* (h) representing the angle in hour, minute and second from 0 to 24 hour from the local meridian westward. The other one, called *Right Ascension* ($R.A.$, α), is measured from 0° to 360° from the First Point in Aries (the Vernal Equinox) towards the East.

In this work, the topocentric equatorial coordinate system with its origin at the detector is used.

Geocentric Solar Magnetospheric (GSM) coordinates: This is a Cartesian system only used in the Earth magnetic field calculation [210]. The x -axis points from the Earth centre to the Sun. The y -axis is defined to be perpendicular to the Earth's magnetic dipole, so that the $x - z$ plane contains the dipole axis. The positive z -axis is chosen to be in the same sense as the northern magnetic pole.

The distance (r) of the detector from the Earth centre will be used also. At the L3+C site this distance amounts to $r_0 = 6369.21$ km [211].

6.2.2 The Earth magnetic field

The Earth magnetic field supplies the bending power for the separation of the 'anti-signal' of antimatter in the primary cosmic ray flux. Therefore, precise information on the field is essential for the method used in this analysis.

The Earth magnetic field includes several components. In the near-Earth space ($< 4R_E$), the field is dominated by the geomagnetic field generated by the electric current in the Earth's outer core and influenced ($\sim 2\%$) by anomalous sources distributed in the crust. Further away from the Earth, the external field (the Magnetospheric Field) becomes important.

The geomagnetic field is relatively stable and the main field can be represented by a simple dipole model with moment $m_E = 8 \cdot 10^{22}$ Am² in the first order approximation. The radial and latitudinal components of the field at a point with distance r from the centre of the dipole and angular distance θ from the dipole axis can be written as

$$B_r = -\frac{2m_E}{r^3} \cos \theta, \quad \text{and} \quad B_\theta = -\frac{m_E}{r^3} \sin \theta. \quad (6.1)$$

It is well known that the geomagnetic field has a large time-scale and unpredictable variation (the secular variation). To describe this variation, the International Geomagnetic Reference Field (IGRF) model [212] is proposed by the International Association of Geomagnetism and Aeronomy (IAGA). In source-free regions at the Earth's surface and above, the main field can be represented as the negative gradient of a scalar potential V , expanded into spherical harmonics as

$$V(r, \theta, \lambda, t) = R \sum_{n=1}^{n_{\max}} \left(\frac{R}{r}\right)^{n+1} \sum_{m=0}^n [g_n^m(t) \cos m\lambda + h_n^m(t) \sin m\lambda] P_n^m(\theta), \quad (6.2)$$

where r, θ, λ are geocentric coordinates (r is the distance from the centre of the Earth, θ is the colatitude, i.e. 90° -latitude, and λ is the longitude), R is the magnetic reference radius (6371.2 km); $g_n^m(t)$ and $h_n^m(t)$ are the coefficients at time t , and $P_n^m(\theta)$ are the Schmidt semi-normalised associated Legendre functions of degree n and order m .

The coefficients are given at five-year intervals based on experimental measurements performed around the world and in the near Earth space. The change within five years is considered to be linear in the IGRF model. An extrapolation is also provided for the near future (~ 5 years). Before year 2000, the harmonics are truncated at $n_{\max} = 10$ with a precision of

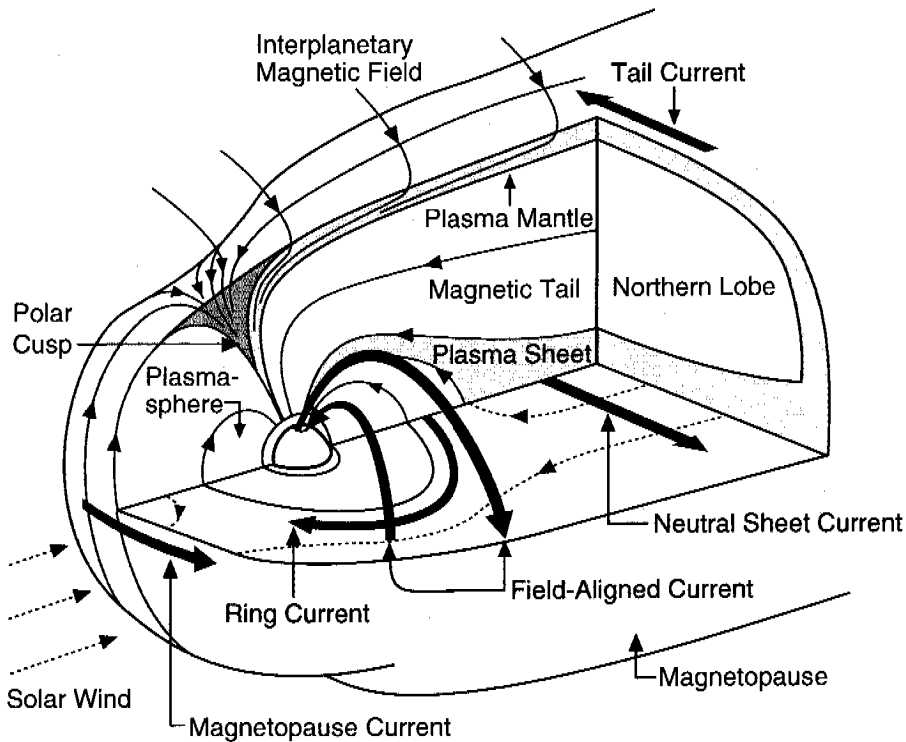


Figure 6.3: The main current system flowing in the Earth's magnetosphere (reprinted from [218]).

1 nT. Since 2000, highly accurate measurements are available, and therefore, the harmonics have been extended to degree $n_{\max} = 13$ with a precision of 0.1 nT [212].

In the outer space, the Earth's magnetic field interferes with the IMF carried along by the solar wind. The region controlled by the Earth is called magnetosphere. The outer boundary of the magnetosphere is called the magnetopause. And the inner side is connected to the ionosphere.

The Magnetospheric field is much more complicated compared to the Earth's internal field. It is a dynamic field, depending on the angle between the Earth's dipole axis and the Sun-Earth direction, and on the solar activity. As shown in Figure 6.3, the external field receives contributions from: (1) currents flowing on the magnetospheric boundary or magnetopause, confining B inside a cavity in the solar wind; (2) The ring current, carried by particles trapped in the Earth's magnetic field; (3) The current system associated with the long magnetospheric tail; (4) The system of the Birkeland currents associated with the polar aurora, flowing in and out of the polar region [213]. Several empirical and semi-empirical models have been developed from different aspects [214, 215]. The Tsyganenko T96 model [216] is used to calculate the magnetospheric field. The input parameters of solar wind observations (hourly mean values) are taken from the OMNI 2 [217] online database.

6.2.3 Tracing a charged particle through a magnetic field

The trajectory of a charged particle in a magnetic field is a helix. However, there is no analytical solutions for motions in a non-homogeneous field. Normally a numerical tracing scheme is used. Since the trajectories of particles with opposite charge and momentum are identical in a given magnetic field, we can use a back-tracing technique to trace a particle from the detector towards its incoming direction.

The motion equation of a particle with charge Ze travelling in a magnetic field B reads

$$\frac{d\mathbf{p}}{dt} = Ze\mathbf{v} \times \mathbf{B},$$

where \mathbf{p} and \mathbf{v} are the momentum and velocity vectors of the particle respectively. Practically, it is convenient to trace the particle in spatial steps. Therefore, the previous equation can be rewritten as

$$\Delta\hat{\mathbf{u}} = \frac{\Delta L}{R/c} \hat{\mathbf{u}} \times \mathbf{B},$$

where ΔL is the step length, $R \equiv pc/Ze$ is the rigidity, and $\hat{\mathbf{u}} = \mathbf{p}/|\mathbf{p}|$ is a unit vector parallel to the momentum \mathbf{p} . To make the tracing accurate and sufficient, a variational step length is used

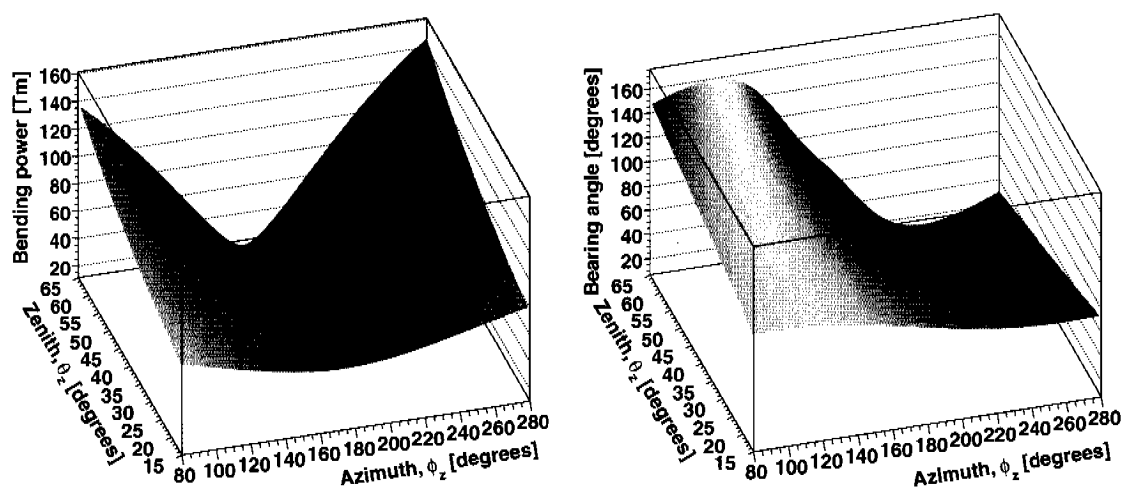
$$\Delta L = \frac{\eta R/c}{|\hat{\mathbf{u}} \times \mathbf{B}|},$$

where the factor η is determined by the required accuracy. Calculations show that setting $\eta = 10^{-5}$ is sufficient to trace a proton back to the Moon's orbit with an accuracy better than 0.01° , despite of the uncertainty of the magnetic field.

If the trajectory does not deviate too much from a straight line, i.e. less than a few degrees, the total deflection angle can be obtained by a numerical integration

$$\theta_{\text{space}} \approx \frac{\sum_{i=1}^n \Delta L_i \times \mathbf{B}(L_i)}{R/c}, \quad (6.3)$$

where n is the number of tracing steps. The numerator, which represents the bending power and the deflection direction, is only depending on the magnetic field B and the total distance L , which themselves are functions of direction and time. Figure 6.4 shows that the total bending power along the straight line between the Moon and the experimental site, as well as the bearing angle (see definition in Figure 6.5) of the deflection angle, are smooth functions of the incident direction in the horizontal system. On the other hand, for a given incident direction and time, the magnitude of the deflection depends only on the rigidity (momentum) of the primary particle, which is unknown. These facts lead to the definition of a *deflection coordinate system* [119, 120], which is illustrated in Figure 6.5, with one axis parallel to the deflection direction, one axis perpendicular to the deflection direction and an axis along the direction of motion.



(a) The total bending power along the straight line from the Moon to the L3+C site. (b) The bearing angle of the deflection vector. (measured from the North towards the East)

Figure 6.4: The bending power and the deflection direction of the Earth magnetic field as a function of the incident direction in the horizontal system at a fixed time.

6.3 Monte Carlo study

6.3.1 Energy distribution of primary particles

With the air shower simulation, the primary-muon response function $R(p_\mu, p_N)$ defined by the muon momentum at the surface level (p_μ) and the momentum of the primary particle per nucleon (p_N), can be determined approximately. Figure 6.6 exhibits such a relation obtained from the CORSIKA (Version 6.200 with hadronic interaction models QGSJET and FLUKA, see Section 1.4.4) simulation for primary protons with a spectral index of $\gamma_0 = -2.7$. Protons are generated homogeneously on top of the atmosphere with zenith angles $\theta_z < 70^\circ$. The primary energy distribution corresponding to the differential muon flux dN/dp_μ is a rather wide distribution.

The probability of secondary muon production depends on the primary energy. Ideally, a primary particle with high enough energy can produce at least one muon in the air shower. Therefore, the probability to detect *one* muon with momentum cut p_μ^{cut} from a primary particle increases with primary energy, and approaches a maximum value at a certain energy, despite of the efficiency of the detector. Figure 6.7 shows the $p_N^{-\gamma_0} \cdot dN/dp_N$ distribution of the M.C. data for different primary spectral indices (γ_0). As expected, the distributions become flat at high primary energies. While at low energy, there is a sharp cut off having an inverse exponential shape. These findings suggest that the primary momentum distribution corresponding

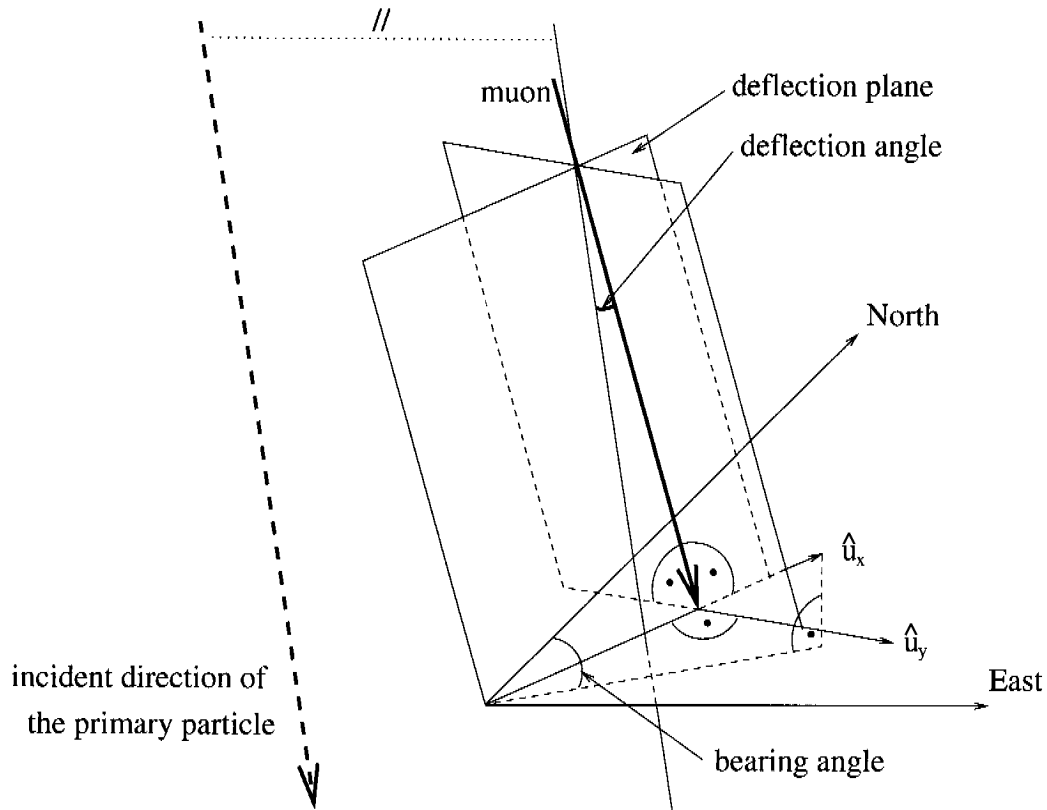


Figure 6.5: The *deflection coordinate system*. The deflection plane is the plane that contains the directional vector of the muon and stays parallel to the incoming direction of the primary particle. \hat{u}_x and \hat{u}_y are the two unit vectors of the deflection system. The bearing angle indicates the orientation of the deflection which is measured on the horizon plane from the North through the East.

to a given muon momentum can be approximated by a power law with an exponential factor,

$$f(p_N) = \frac{1}{p_0^{\gamma+1} \Gamma(-\gamma-1)} p_N^\gamma \exp\left(-\frac{p_0}{p_N}\right), \quad (6.4)$$

where γ and p_0 are free parameters, which are in turn functions of muon momentum p_μ (see below), to be determined by M.C. simulation. This function has been normalised to unity over the range $(0, \infty)$.

The M.C. data sample is divided into small muon momentum intervals, and the primary distributions (dN/dp_N) are fitted to this function. The results for p_0 and γ and their dependences on the muon momenta are shown in Figure 6.8. The value of p_0 increases linearly with the muon momentum and only slightly depends on the input value of the primary spectral index. The value of γ is larger than the input value (γ_0) and decreases logarithmically with increasing muon momentum. The two parameters (γ, p_0) are then replaced by

$$\gamma = \gamma' - c_1 \ln p_\mu, \quad p_0 = p_0' + c_2 p_\mu \quad (6.5)$$

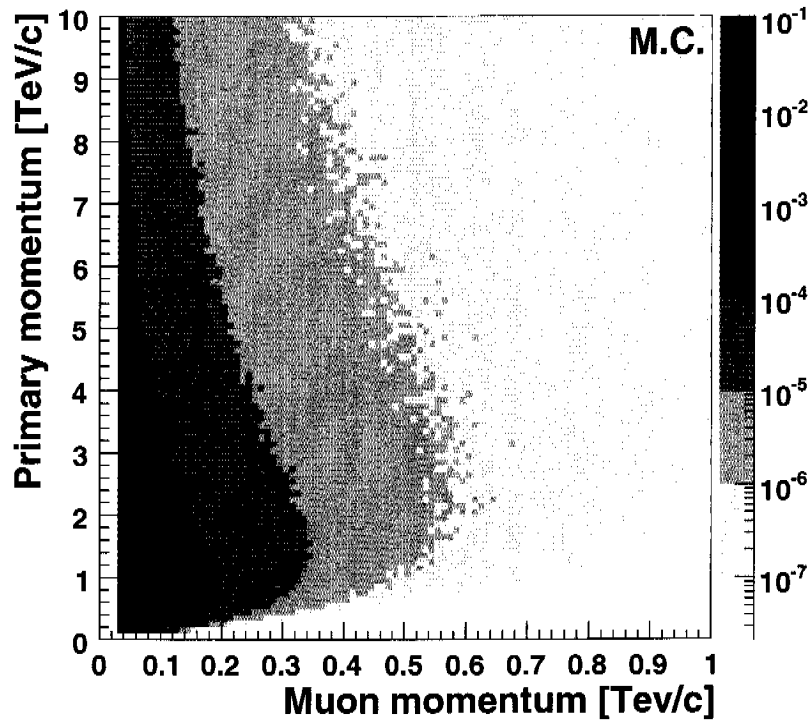


Figure 6.6: The relation between the momentum of primary protons and the momentum of secondary muons obtained from the CORSIKA (QGSJET+FLUKA) simulation. Primary protons are generated homogeneously on top of the atmosphere with a spectral index $\gamma_0 = -2.7$ and zenith angles $\theta_z < 70^\circ$. The grey scale represents the relative event density.

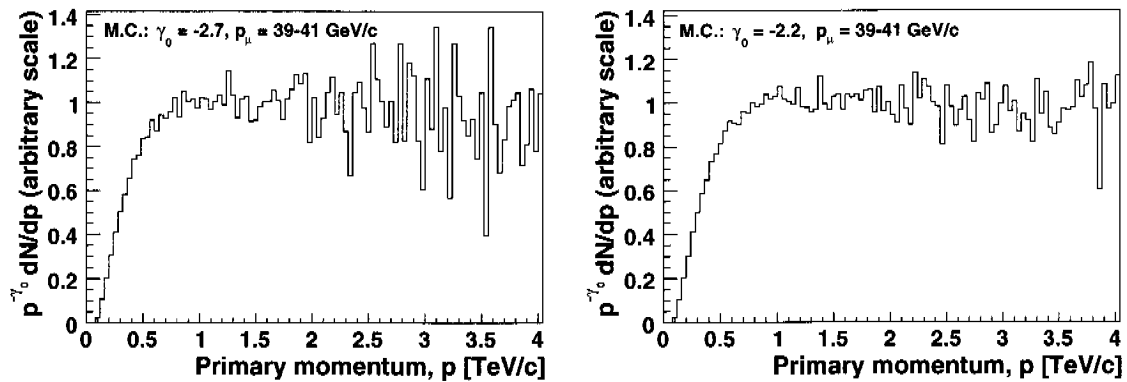


Figure 6.7: Distribution of the primary momenta for given muon momentum range 39 – 41 GeV/c. The simulation is performed with protons with spectral indices of -2.7 and -2.2 .

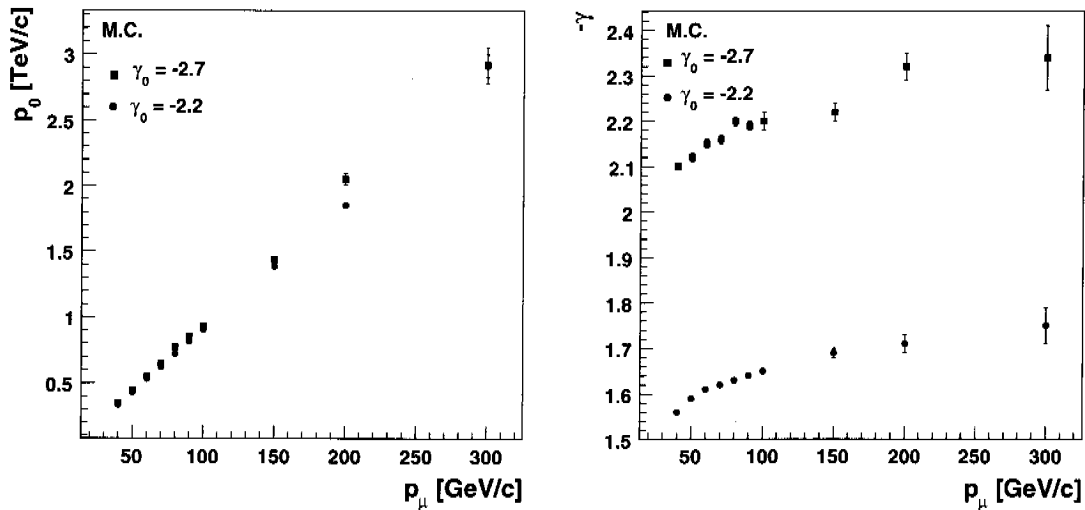


Figure 6.8: Primary energy distribution parameters (p_0 and γ) obtained with a least square fit to function (6.4) for small muon momenta intervals. To have enough statistics, the widths of the intervals are chosen to increase with the momenta which are 39-41, 49-51, 59-61, 68-72, 77-83, 86-94, 95-105, 140-160, 190-210 and 290-300 GeV/c respectively.

Table 6.2: Parameters of the primary energy distribution function (6.5) determined from the binned maximum likelihood fit.

Input (γ_0)	γ'	c_1	p'_0 (GeV/c)	c_2 ([GeV/c] $^{-1}$)
proton (-2.7)	-1.693 ± 0.005	0.110 ± 0.001	-49.1 ± 0.7	10.00 ± 0.01
proton (-2.2)	-1.24 ± 0.01	0.090 ± 0.002	-45.8 ± 1.6	9.56 ± 0.03
proton (-3.2)	-2.10 ± 0.02	0.144 ± 0.006	-56.8 ± 2.4	10.50 ± 0.05
helium (-2.7)	-1.71 ± 0.01	0.103 ± 0.004	-45.9 ± 1.9	9.83 ± 0.04

where γ' , p'_0 , c_1 and c_2 are free parameters, p_μ is the muon momentum at the surface level in units of GeV/c. The 2D primary-muon response histogram (p_μ, p_N) is fitted to function (6.4) with these four parameters using a binned likelihood method. The results are listed in Table 6.2. The power law factor of function (6.4) represents the momentum distribution of primary particles and the value of γ' is roughly equal to $\gamma_0 + 1$. On the other hand, the exponential factor represents the muon production probability which can be considered as “efficiency”, depending mainly on the muon momentum.

When reporting the final results of our analysis, we need to quote the energy range of the primary particles contributing to the observed Moon shadow. There are some general considerations concerning this point.

The mean energy. This is the most simple idea, but it has some obvious disadvantages. The primary particles have a wide energy distribution over several orders of magnitude, therefore, the mean energy has not too much physical meaning and its value is strongly dependent on the tail of the distribution, e.g. a very high value at the end of the spectrum can increase the mean value dramatically.

The median energy. A better representation of the primary energy corresponding to the differential muon flux is the median energy [219]. For the sake of simplicity, a crude estimator of this energy which is widely used, is ten times the corresponding muon energy. In [219], this relation was calculated with the scaling model of hadron interactions and was parameterised to

$$E_{\text{median}} = 6.9 \cdot (E_{\mu} + 2 \text{ GeV}) \quad (\text{for } 0.5 < E_{\mu} < 300 \text{ GeV}). \quad (6.6)$$

As pointed out by the authors themselves, this value depends on the primary spectral index. Since the energy distribution of antiprotons in the range we are searching for is unknown, this is also not a good solution.

An energy threshold. As mentioned before, the “efficiency” to detect at least *one* muon from the primary particle increases with the primary energy, and approaches 100% at a certain energy. Consequently, we can define the starting energy, where the “efficiency” reaches an arbitrary value η for a muon data sample with momentum cut p_{μ}^{T} , as the primary momentum threshold. For this purpose, the primary distribution corresponding to the integrated muon flux with threshold p_{μ}^{T} is fitted to function (6.4). The results are shown in Table 6.3. The “efficiency” factor, determined by the parameter p_0 , is nearly independent of the selected input values of γ_0 . Therefore, the threshold at a given “efficiency” η can be obtained simply through $p_{\text{N}}^{\text{T}} = -p_0 / \ln(\eta)$. Since the values of p_0 is roughly 11.7 times the muon momentum threshold p_{μ}^{T} , the threshold of the primary momentum per nucleon can be approximately parameterised to,

$$p_{\text{N}}^{\text{T}} = -11.7 \cdot p_{\mu}^{\text{T}} / \ln(\eta), \quad (6.7)$$

which is independent of the spectral index of the primary spectrum and it is assumed to be valid for $0 < \eta < 0.5$. For a power-law distribution with spectral index γ , the median momentum per nucleon of primary cosmic rays can be derived,

$$p_{\text{N}}^{\text{median}} = 0.5^{\frac{1}{\gamma+1}} p_{\text{N}}^{\text{T}} \quad (6.8)$$

The upper boundary, where 84% primary particles are included, is then,

$$p_{\text{N}}^{\text{UP}} = 0.16^{\frac{1}{\gamma+1}} p_{\text{N}}^{\text{T}}. \quad (6.9)$$

These two quantities are obviously depend on the spectral index of the primary distribution.

Table 6.3: The momentum distribution parameters (p_0 and γ defined in equation (6.4)) corresponding to a certain muon momentum cut (p_μ^T) for primary protons with different input spectra indices (γ_0).

$p_\mu^T(\text{GeV}/c)$ (at surface level)	$\gamma_0 = -2.7$ (input)		$\gamma_0 = -2.2$ (input)	
	$p_0(\text{TeV}/c)$	$-\gamma$	$p_0(\text{TeV}/c)$	$-\gamma$
30	0.36	1.94	0.37	1.44
40	0.47	1.95	0.47	1.45
50	0.59	1.96	0.59	1.46
60	0.70	1.97	0.70	1.46
70	0.82	1.98	0.81	1.47
80	0.93	1.99	0.92	1.47
90	1.05	2.00	1.03	1.48
100	1.16	2.00	1.15	1.48

Table 6.4: Absolute flux in number of particles (Φ_Z^0) and number of nucleons (Φ_N^0) at $E_0 = 1$ TeV/nucleon and spectral index γ_Z . The data of Φ_Z^0 and γ_Z are from Ref. [220]. Only elements having a relative abundance larger than 1% with respect to protons are selected.

	Z	A	$\Phi_Z^0 [(\text{m}^2 \text{ sr s TeV})^{-1}]$	$\Phi_N^0 [(\text{m}^2 \text{ sr s TeV})^{-1}]$	$-\gamma_Z$
H	1	1	8.73×10^{-2}	8.73×10^{-2}	2.71
He	2	4	5.71×10^{-2}	2.35×10^{-2}	2.64
C	6	12	1.06×10^{-2}	0.21×10^{-2}	2.66
N	7	14	2.35×10^{-3}	0.04×10^{-2}	2.72
O	8	16	1.57×10^{-2}	0.24×10^{-2}	2.68
Mg	12	24	8.01×10^{-3}	0.10×10^{-2}	2.64
Si	14	28	7.96×10^{-3}	0.07×10^{-2}	2.75
Fe	26	56	2.04×10^{-2}	0.19×10^{-2}	2.59

6.3.2 Primary cosmic-ray composition

As described in Chapter 1 the chemical composition of primary cosmic rays has been investigated with direct measurements. The most recent results are quoted in Table 6.4 (see Ref. [220] for a full compilation). Only elements having a relative abundance larger than 1% with respect to protons are selected. All of them have nearly identical spectral indices. In the hadronic interactions of EAS, nucleons in a nucleus can be considered as free since the bonding force can be neglected comparing to the strong interaction. Therefore, the muon production probability is determined by the number of nucleons and energy per nucleon $E_N = \frac{E_0}{A}$, with E_0 being the total energy of the nucleus. The absolute fluxes of the selected elements have been converted to a flux in number of nucleons and listed in Table 6.4. Assuming all

the elements having an identical spectral index of -2.7 , the portion of muons contributed by protons is 73%. The other elements have approximately the same value of $Z/N = 0.5$, and thus have a similar behaviour as helium nuclei when travelling in a magnetic field. Therefore, the observed muon flux is considered to be originated at 73% from protons and 27% from helium nuclei in the following discussions.

6.3.3 Deflection function

The Earth magnetic field can be calculated with models but the momentum of the primary particle is unknown. Therefore, the magnetic deflection in a given direction at a given time and for muons with given momenta are still widely distributed. According to equation (6.3) and (6.5), the distribution of the deflection angle (θ_{defl}), depending on the muon momentum (p_μ), the incident direction (\mathbf{r}) and the time (t), can be written as,

$$f_{\text{defl}}(\theta_{\text{defl}}; p_\mu, \mathbf{r}, t) = \left(\frac{TZe}{Ap_0} \right)^{\gamma+1} \frac{1}{\Gamma(-\gamma-1)} |\theta_{\text{defl}}|^{-\gamma-2} \exp\left(-\frac{Ap_0}{TZe} \theta_{\text{defl}}\right), \quad (6.10)$$

where γ and p_0 takes the form of Equation (6.5) with parameters γ' , c_1 , p'_0 and c_2 which in turn are derived from the CORSIKA simulation (see Table 6.2), Z and A is the charge number and the atomic number of the particle, and $T(\mathbf{r}, t) = \left| \int d\mathbf{L} \times \mathbf{B} \right|$ is the total bending power of the Earth magnetic field. This function is only defined on the semiaxis having the same sign as the charge number Z , i.e. the exponent of the exponential part should always be negative. On the opposite semiaxis, the probability density is always zero.

In the data, this distribution is convoluted with the angular resolution, which is assumed to be a Gaussian distribution

$$f_{\text{res}}(\theta_{\text{plane}}; p_\mu, \mathbf{r}) = \frac{1}{\sqrt{2\pi}\sigma(p_\mu, \mathbf{r})} \exp\left(-\frac{\theta_{\text{plane}}^2}{2\sigma^2(p_\mu, \mathbf{r})}\right). \quad (6.11)$$

The angular resolution $\sigma(p_\mu, \mathbf{r})$ is given by expression (5.19) and the parameters therein, θ_{plane} is the projected angle (θ_x or θ_y). In addition, taking into account the angular size of the Moon (R_M), the distribution of the events blocked by the Moon along the x -axis in the *deflection coordinate system* is

$$f_x(\theta_x; p_\mu, \mathbf{r}, t) = \int_{\theta_{\text{min}}}^{\theta_{\text{max}}} f_{\text{defl}}(\theta_x - \theta'; p_\mu, \mathbf{r}, t) d\theta' \int_{-R_M}^{R_M} \frac{2\sqrt{R_M^2 - \theta'^2}}{\pi R_M^2} f_{\text{res}}(\theta' - \theta''; p_\mu, \mathbf{r}) d\theta''. \quad (6.12)$$

6.3.4 Moon shadow simulation

The whole sky is divided into 100×100 cells in the horizontal coordinate system. Primary particles (essentially protons and helium nuclei with spectral indices of -2.7) are generated on top of the atmosphere in a cone of 10 degrees around each cell along the Moon trajectory

and according to the Moon exposure time inside the cell. All the primary particles are traced by the CORSIKA of version 6.200 with hadronic interaction models QGSJET and FLUKA (see Section 1.4.4) through the atmosphere. The produced secondary muons are scattered at the surface level according to the detector's size to increase the simulation efficiency. Then the muons are fed to the detector's simulation program (see Section 3.4). The simulated muon events are reconstructed in the same way as the raw data and the same selection criteria are applied. For each remaining event, the primary particle is back-traced to the altitude of the orbit of the Moon through the Earth magnetic field. If it hits the Moon, then it is removed from the primary flux.

6.4 The Moon data sample

The apparent direction (δ , α) of the Moon in the topocentric equatorial coordinate system is computed for the time at which each event passes the cuts (see Section 4.3) and transferred to the horizontal coordinate system with the SLALIB [221]¹ programme. Due to the close distance of the Moon, the parallax, which amounts to a fraction of a degree, has been taken into account in the SLALIB routines.

Events having opening angles less than 5° with respect to the Moon direction are considered to be 'Moon events'. Ten independent background data samples are selected also by altering the R.A. of the Moon by $i * 11^\circ / \cos \delta$ ($i = \pm 1, \pm 2, \pm 3, \pm 4, \pm 5$) while the declination (δ) is fixed. The background samples cross the sky in the same way as the real Moon data sample from the detector's point of view. As shown in Figure 6.9 these data sets are named as off-moon data samples A1, A2, ..., A5 and B1, B2, ..., B5, according to the corresponding sky region crossed, after or before the Moon. Over the long data-taking time, any difference on the live-time in these data samples could be neglected.

The momentum distribution of muons coming from the Moon direction is shown in Figure 6.10. It is nearly a power law with a spectral index of -3.1 at high momenta. To make the comparison to the previous study [119] easier, the same momentum ranges, i.e. $p_\mu > 100 \text{ GeV}/c$ and $65 < p_\mu < 100 \text{ GeV}/c$ are chosen. Since the angular resolution improved with the new version of the Ntuple data and has been studied elaborately with the double muon data, an additional momentum range with a lower boundary, down to $30 \text{ GeV}/c$ will be used as well. Actually, these momentum ranges are only used to check the shadowing effect, i.e. various histograms for the visualisation. For the study of the antiproton ratio, a binned and an unbinned maximum likelihood method will be used for the whole momentum range.

The distribution of the Moon position corresponding to the selected data sample and the muon incident direction in different coordinates are shown in Figure 6.11. The apparent radius of the Moon disk varies from 0.25° to 0.28° (see Figure 6.12) due to the Moon's ellipsoidal orbit and the size of the Earth. The average value is 0.272° .

¹SLALIB is a library of routines intended to make accurate and reliable positional-astronomy applications. The versions currently in service are written in Fortran 77. A special ('proprietary' ANSI C) version provided by the author [222] is used in this analysis.

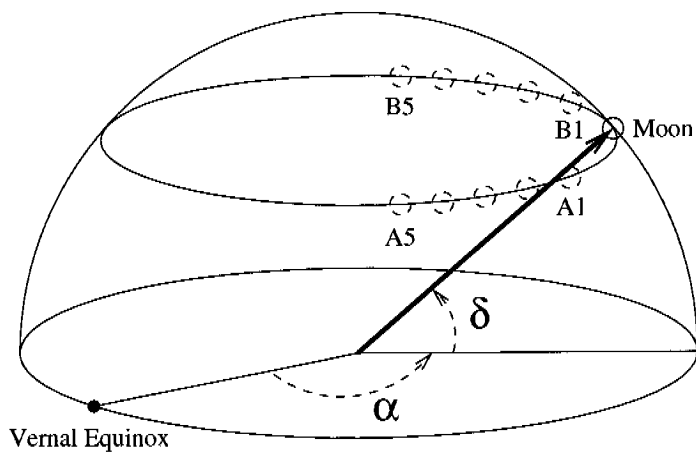


Figure 6.9: The relative positions of the Moon and the off-moons on the sky.

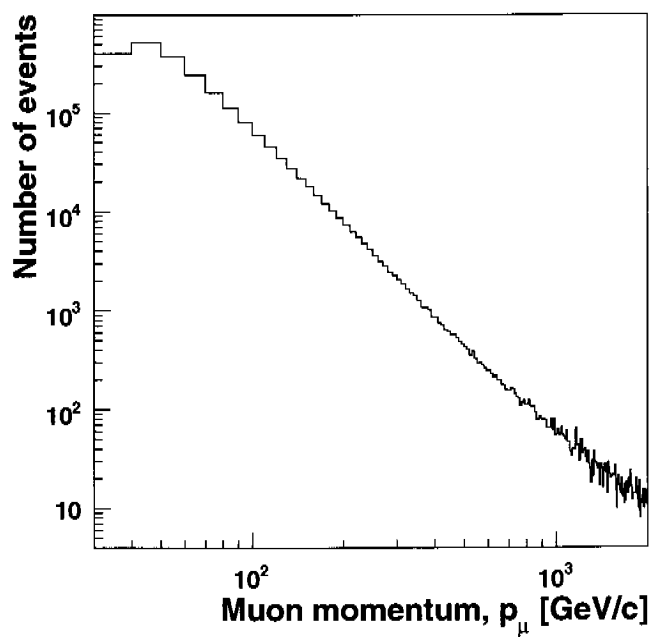
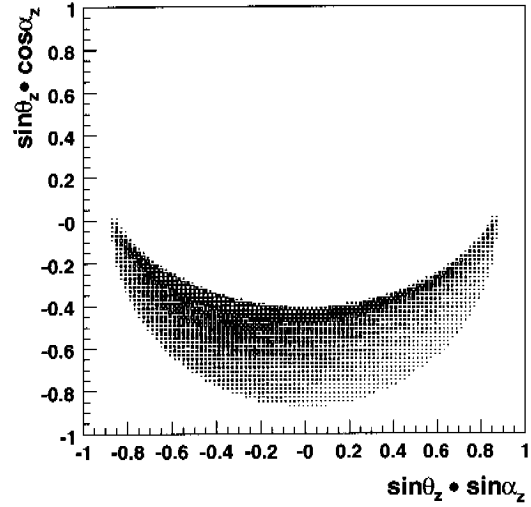
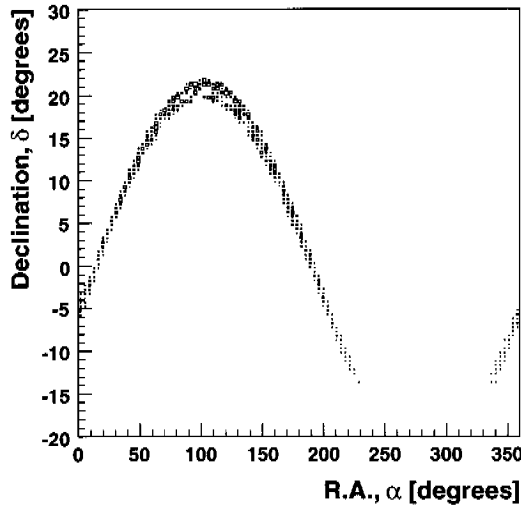
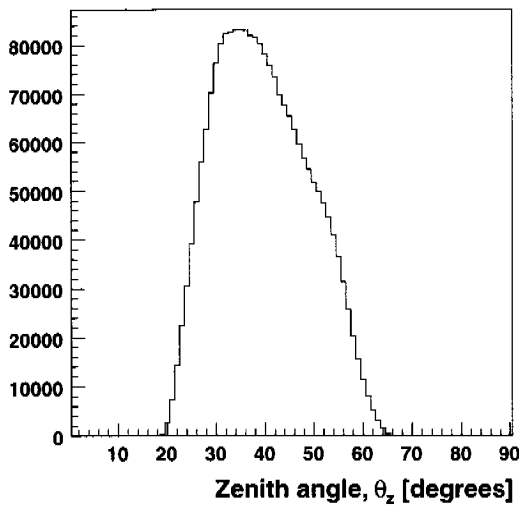


Figure 6.10: The momentum distribution of muons from the Moon data sample.

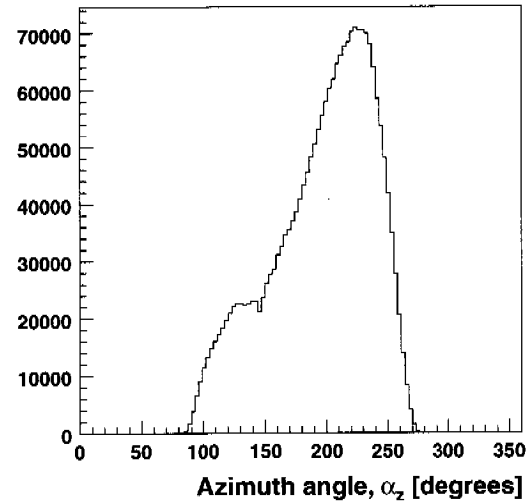


(a) Distribution of the Moon trajectory in the equatorial system

(b) Distribution of the Moon trajectory in the horizon system



(c) Zenith angle distribution of muons



(d) Azimuth angle distribution of muons. (structure due to the particular detector acceptance)

Figure 6.11: Some general distributions of the Moon data sample. The size of the boxes in (a) and (b) indicate the number of events.

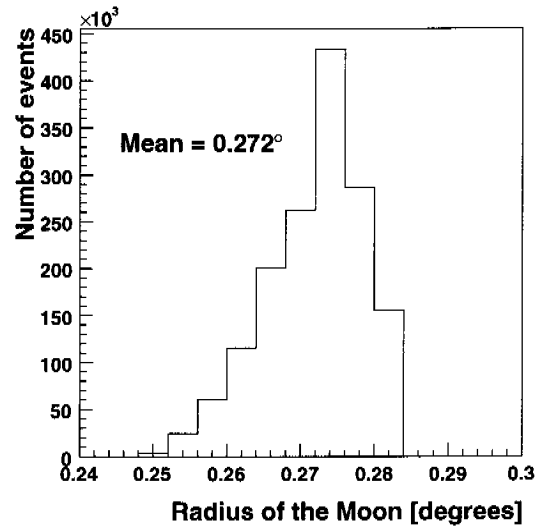


Figure 6.12: The radius of the Moon corresponding to the events in the Moon data sample.

6.4.1 The expected angular resolution

The angular resolution of muons with respect to their parent particles can be calculated event by event with function (5.19). Table 6.5 lists the average values for the muon momentum bands of $p_\mu > 100 \text{ GeV}/c$, $65 < p_\mu < 100 \text{ GeV}/c$ and $30 < p_\mu < 65 \text{ GeV}/c$ respectively.

Table 6.5: The average angular resolution for the three momentum bands determined with function 6.5. The errors are the RMS values of the corresponding distributions.

$p_\mu [\text{GeV}/c]$	Angular resolution ($^\circ$)
> 100	0.24 ± 0.07
65-100	0.44 ± 0.09
30-65	0.75 ± 0.17

6.4.2 The expected deflection in the Earth magnetic field

The bending power of the magnetic field ($\int d\mathbf{L} \times \mathbf{B}$) is calculated along the opposite direction of each incident muon in the Moon data sample. The distribution of the magnitude and direction of this vector are shown in Figure 6.13.

According to function (6.10) and the estimation that 73% muons are from protons and 27% can be represented by helium nuclei (see Section 6.3.2) the distribution of the deflection angle can be determined. The average deflection angle as a function of the muon momentum

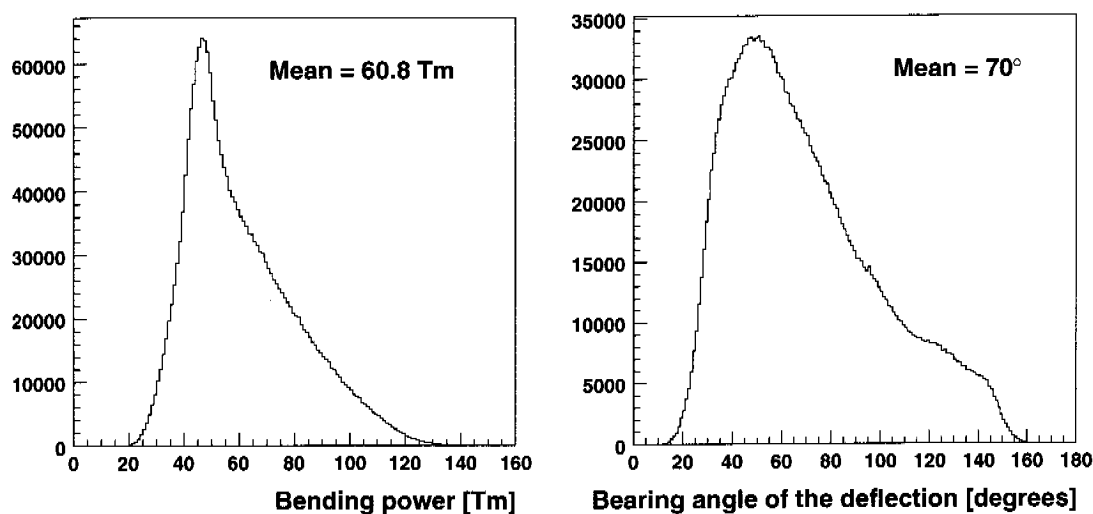


Figure 6.13: The bending power and the bearing angle of the deflection associated with the Moon events.

Table 6.6: The Landau approximation of the expected deflection angle distribution. The parameter MPC indicates the maximum of the distribution (see text).

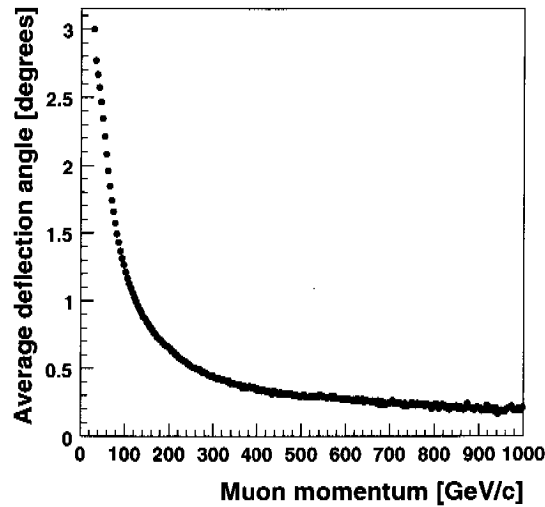
p_μ [GeV/c]	MPC [°]	σ_{Landau} [°]
> 100	0.24	0.26
65 – 100	0.51	0.48
30 – 65	0.82	0.76

is shown in Figure 6.14. The distributions of the deflection angle and the convoluted deflection angle (function (6.12)) in the three momentum bands are also presented in the same figure. The convolution significantly modifies the shapes of the distributions especially in the small-angle regions, but has only a marginal effect on the average values of the distributions.

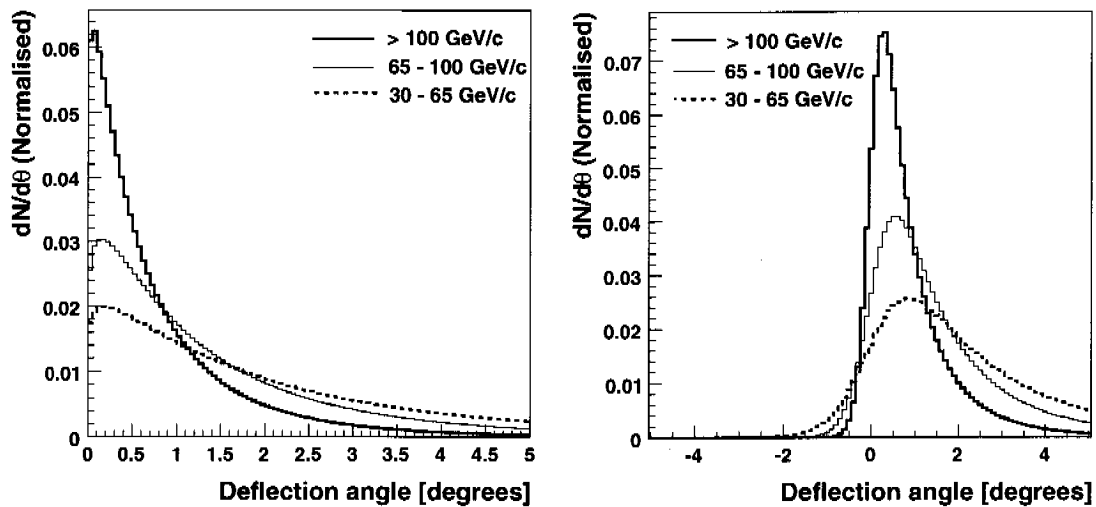
The distributions of the convoluted deflection angles have a Landau²-like shape in the central part. Table 6.6 lists the Corrected Most Probable value (MPC)³, i.e. the maximum of the distribution and σ_{Landau} of the Landau distribution for the three muon momentum ranges.

²Inspired from the previous analysis [119]. The Landau distribution is provided within the ROOT framework [193], adapted from the CERLIB routine G110 denlan.

³The Most Probable Value (MPV) is shifted to -0.22278298 in the CERLIB version of the Landau distribution with the parameter $\sigma_{\text{Landau}} = 1$. Therefore, the maximum of the Landau distribution is at $\text{MPC} = \text{MPV} - 0.22278298\sigma_{\text{Landau}}$.



(a) The average deflection angle as a function of muon momentum.



(b) Distributions of the deflection angles of the three momentum bands. There are 0.6%, 4.8% and 12.8% events which have deflection angles larger than 5° , and the average deflection angles are 0.80° , 1.29° and 1.63° respectively.

(c) Distributions of the convoluted deflection angles (function (6.12)). There are 0.9%, 4.9% and 13.0% events which have deflection angles larger than 5° , and the average deflection angles are 0.80° , 1.28° and 1.59° respectively.

Figure 6.14: The predicted deflection angle distributions determined with function (6.10).

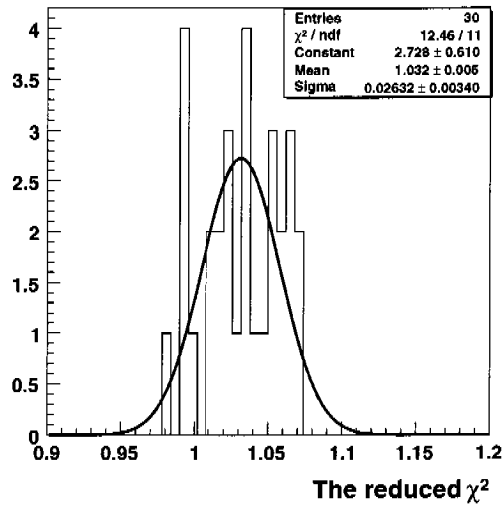


Figure 6.15: Distribution of the reduced χ^2 of the 2D fit to the background data samples (see text for the details). The solid curve is a maximum-likelihood fit to the Gaussian distribution.

6.4.3 The background

In this analysis, the muon event distribution in the absence of the Moon is considered as background which is assumed to be a smooth surface taking the form of

$$f(x, y) = \lambda(1 + ax + by),$$

where λ represents the average number of events per bin ($0.1^\circ \times 0.1^\circ$). This hypothesis is checked with the ten background data samples. The 2D histograms in the three momentum bands in the *deflection coordinate system* are fitted to this function. Due to the large number of degrees of freedom ($ndf = 4797$), the χ^2 value should obey the Gaussian statistics. Figure 6.15 presents the distribution of the values of the reduced chi-square. A maximum-likelihood fit revealed that the standard error of the distribution (0.026 ± 0.003) is consistent with the expected value of 0.029. Therefore, the hypothesis that the 2D histograms can be fitted to inclined surfaces is confirmed.

The average event densities obtained from the fits are shown in Figure 6.16. The event density tends to increase in the background data samples taken further away from the real Moon position. Since the parallax correction depends on the direction in the horizon system, the background samples have slightly different acceptances resulting in different number of events. These background data samples are mainly used for validation tests, and therefore this difference has no effect on the final results. Extrapolated to the real Moon position, the event densities should be 2817 ± 6 , 4025 ± 6 and 12566 ± 11 per degree² for the momentum range $p_\mu > 100 \text{ GeV}/c$, $65 < p_\mu < 100 \text{ GeV}/c$ and $30 < p_\mu < 65 \text{ GeV}/c$ respectively. In unit of the average solid angle of the Moon (Ω_M), these densities reads 654.7 ± 1.4 , 935.5 ± 1.4 and $2920.7 \pm 2.6 \Omega_M^{-1}$. These values represent the expected numbers of events blocked by the

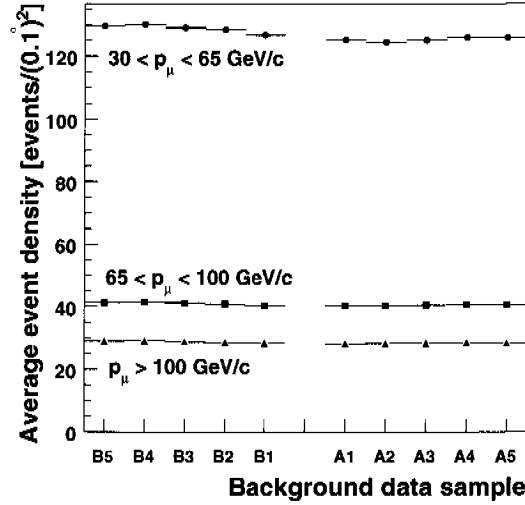


Figure 6.16: The average event density of the ten background data samples for the three different muon momentum ranges.

Moon in the three momentum ranges.

6.5 The shadowing effect

The simplest way to show the shadowing effect is to check the distribution of the angular distance of the muon with respect to the Moon. In Figure 6.17, the event density, i.e. the number of events divided by the solid angle measured in units of the average solid angle of the Moon (Ω_M), is shown as a function of the angular distance from the centre of the Moon. For comparison, the same distributions from the ten off-moon data samples are scaled and superimposed to them. The shadowing effect can be clearly seen in the first few bins. The flat distribution of off-moon data confirmed that the event deficits are not caused by mistakes in the analysis program.

Approximating the average angular resolution as a Gaussian distribution and taking into account the size of the Moon, the p.d.f corresponding to these plots can be given as

$$\frac{dN}{d\Omega}(\Delta\theta) = \lambda \left[1 - \int_0^{\theta_M} \int_0^{2\pi} r \cdot \frac{1}{2\pi\sigma^2} \exp\left(-\frac{(\Delta\theta - r \cos \phi)^2 + (r \sin \phi)^2}{2\sigma^2}\right) dr d\phi \right]. \quad (6.13)$$

However, due to the effect of the Earth magnetic field, the observed distributions significantly deviated from the expected p.d.f.. Therefore, the experimental angular resolution can not be derived from the one-dimensional histograms.

On the other hand, large fluctuations are expected in the two-dimensional histograms due to the low statistics in each bin. Therefore, a smoothing technique must be applied to get a

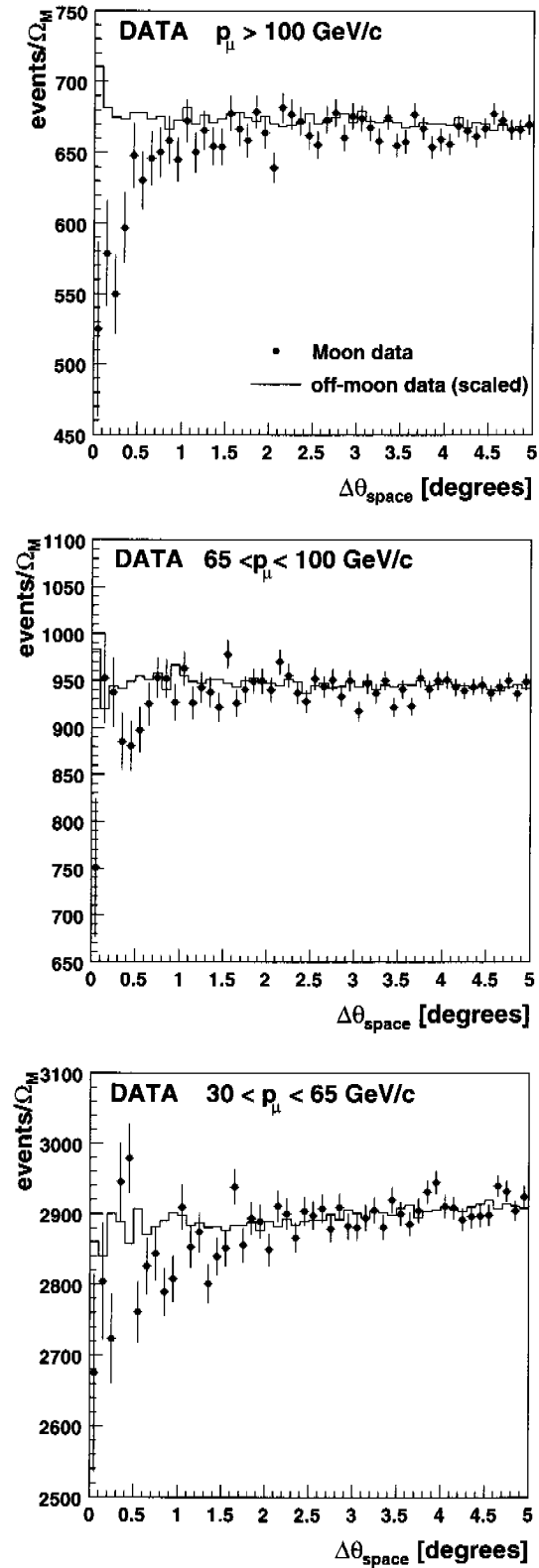


Figure 6.17: The event density as a function of the angular distance to the Moon. The lines represent the scaled event density of the superimposed ten off-moon data samples.

visible image. A signal-like Gaussian filter is a good choice for this purpose. The content of each bin ($n_{i,j}$) is replaced by the weighted average value of this bin and neighbour bins

$$n'_{i_0,j_0} = \frac{\sum_{i,j} n_{i,j} \cdot G(\sigma, x_i - x_0, y_j - y_0)}{\sum_{i,j} G(\sigma, x_i - x_0, y_j - y_0)} \quad (\text{if } \sqrt{(x_i - x_0)^2 + (y_j - y_0)^2} < 1.58 \sigma),$$

where (x_i, y_j) and (x_0, y_0) are the coordinates of the bins (i, j) and (i_0, j_0) respectively in any orthogonal coordinate system, and the weight $G(\sigma, x, y) = \frac{1}{2\pi\sigma^2} \exp(-\frac{x^2+y^2}{2\sigma^2})$ is a product of two independent Gaussian functions with identical standard deviations. The values of σ are based on the pre-determined quantities (see Section 6.4.1. The exact values are indicated on the plots (Figure 6.18)).

The significance of the event deficit is evaluated for the smoothed histograms in the equatorial coordinate system and the *deflection coordinate system* with the three momentum ranges. In the ‘pictures’ taken in the equatorial system (Figure 6.18), the shadows are observed to be deflected to the west side as expected. In the *deflection coordinate system*, the shadows are stretched along the x -axis while nearly symmetrically distributed along the y -axis, and have higher maximum significances (see the scales of the individual plots) than those in the equatorial system.

The positions of the centres of the deficits are in good agreements with the predicted values (Table 6.6) except in the plot for muons in the momentum band of 65 – 100 GeV/c in the *deflection coordinate system*, where the large fluctuations (see Figure 6.19 and text below) have significant effect on the smoothed image. Nevertheless, good agreement is obtained in the fits with the projected distribution (Figure 6.19 and the 2D histogram (Table 6.7)).

The projected slices along the x - and y -axis of the *deflection coordinate system* are shown in Figure 6.19. The shapes of the distributions significantly depend on the range used for the projection. To make the comparison meaningful, a uniform criterium is applied on the three muon momentum ranges. The projection ranges of the y -slices are set to be the sum of the radius of the Moon and the average angular resolution ($R_M + \sigma$). For the x -slices, the projection start from $-(R_M + \sigma)$, and end at the point determined with Figure 6.14 which contains 90% of the events.

The x -slices are fitted to a simple function where only a Gaussian (anti) signal with background is considered,

$$f(\theta_y) = N(1 + b \theta_y) - N_{\text{miss}} \frac{1}{\sqrt{2\pi}\sigma} \exp(-\frac{\theta_y^2}{2\sigma^2}).$$

“Subtracting” the RMS value of the Moon disk ($= R_M/2$) from the ‘Sigma’-values in the fit results of the x -slices, the effective angular resolutions are determined to be $0.25^\circ \pm 0.06^\circ$, $0.43^\circ \pm 0.12^\circ$ and $0.87^\circ \pm 0.50^\circ$ for the three muon momentum ranges respectively. They are in good agreement with the expected values (see Table 6.5). The number of missing events (see Figure 6.19) determined from the fit are also consistent with the values obtained from the background analysis (see Section 6.4.3). Good agreement is observed according to the reduced χ^2 values (see Figure 6.19).

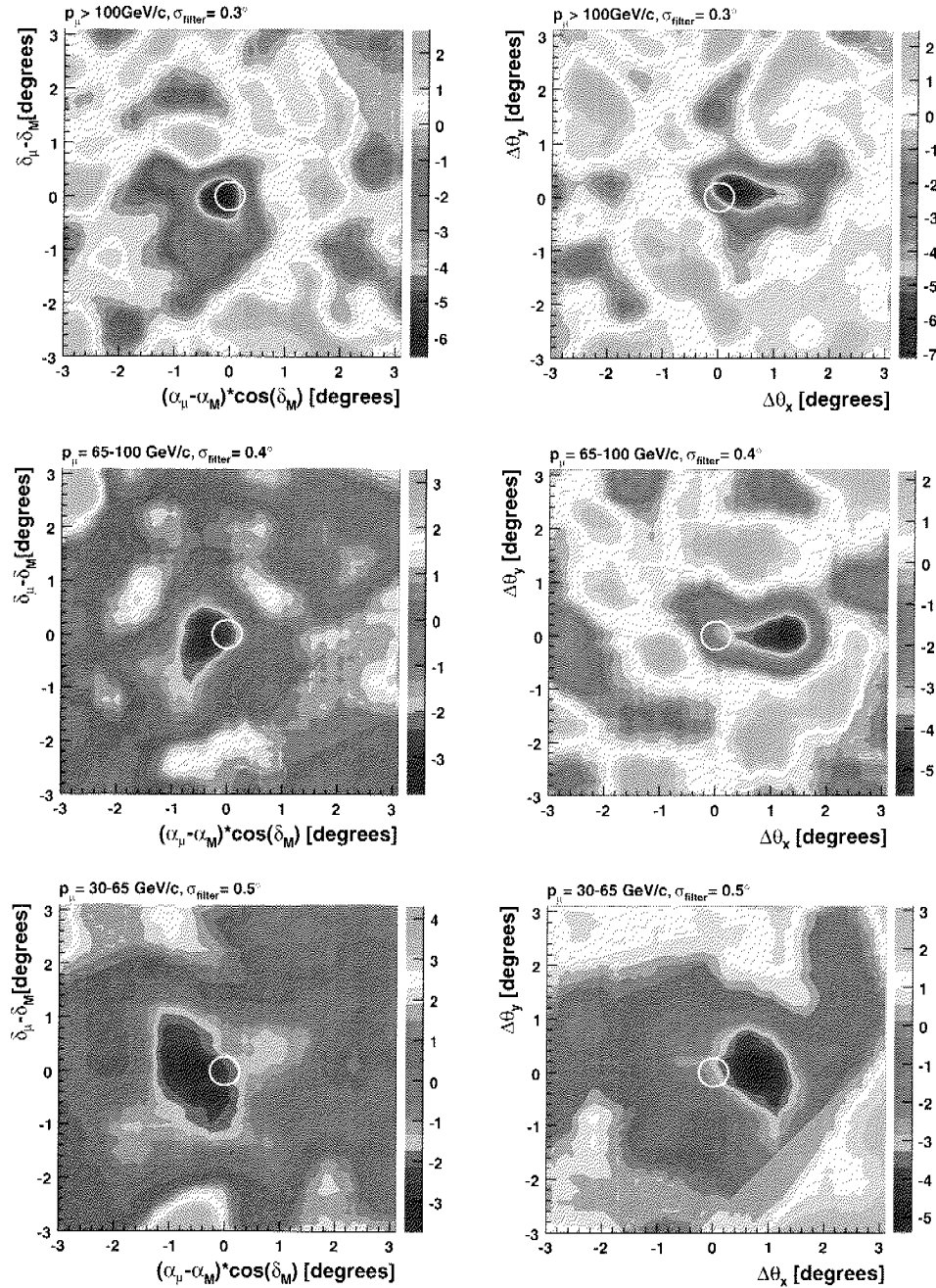
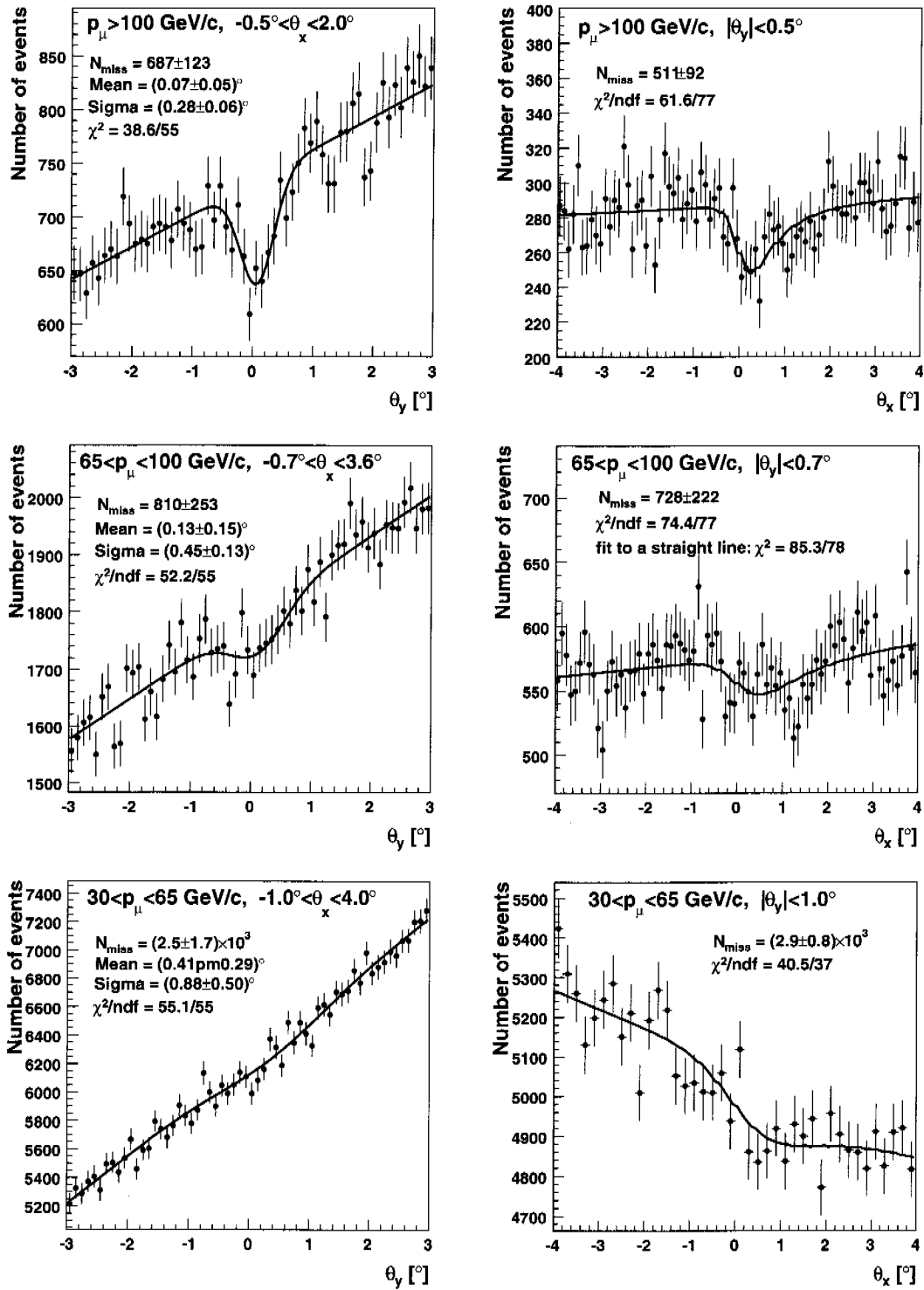


Figure 6.18: The significances of event deficits determined in the three momentum ranges. The left column is in the topocentric equatorial system, and the right column is in the *deflection system*. A smoothing technique with Gaussian filter has been applied to get a clear shadow image (see text). The white circles indicate the position and the size of the Moon. The shifts of the shadow in the equatorial system are increased with the muon momentum as expected. However, the shift of muon with momenta between 65 and 100 GeV in the *deflection system* is larger than the expected value. It is caused by the statistical fluctuations (see the projected histogram in Figure 6.19, where the fit position is in between the near and the far distance from the Moon. In the final two dimensional likelihood fit the position is also correctly positioned (see Table 6.7 and 6.8)).

Figure 6.19: Projected slices in the *deflection coordinate system*.

6.6 Maximum likelihood analysis

For simplicity, (x, y) is used to denote the two orthogonal coordinates in the *deflection system* throughout this section. The two dimensional maximum likelihood fits are performed in a symmetric rectangular region $(-X, -Y, X, Y)$, where $X = 4^\circ$ and $Y = 3^\circ$.

6.6.1 The likelihood function

According to the off-moon data analysis, the background can be approximated with an inclined smooth plane (see Section 6.4.3). The normalised background p.d.f in the rectangular region $(-X, -Y, X, Y)$ is

$$f_{\text{bck}}(x, y; a, b) = (1 + ax + by)/(4XY)$$

Assuming the distributions along x - and y -axis are uncorrelated, the p.d.f of the missing events can be given by a product of two independent terms,

$$f_{\text{deficit}}(x, y) = f_x(x)f_y(y)$$

By definition, the y -distribution of the missing muons should be determined only by the total angular resolution and the size of the Moon. In addition, M.C. simulations indicate that the total angular resolution of muons does nearly not depend on the type of primary particles. Therefore, the projection on the y -axis can be represented by a Gaussian distribution convoluted with the Moon disk,

$$f_y(y; y_0, k) = \int_{-R_M}^{R_M} \frac{2\sqrt{R_M^2 - u^2}}{\pi R_M^2} \frac{1}{\sqrt{2\pi} k \sigma(\mathbf{p}_\mu)} \exp\left(-\frac{(y - y_0 - u)^2}{2k^2 \sigma^2(\mathbf{p}_\mu)}\right) du \quad (6.14)$$

where $\sigma(\mathbf{p}_\mu)$ is determined with function (5.19) event by event and k is a free scaling factor to the pre-determined value of the angular resolution (see Chapter 5). Since the apparent radius of the Moon (R_M) varies from 0.25° to 0.28° (see Figure 6.12), its value is also determined event by event.

On the other hand, the projection of the distribution on the x -axis is depending on Z/A of the primary particle. Consider the muon contribution from protons, helium nuclei (see Section 6.3.2), and the potential contribution from antiprotons, the p.d.f on x -axis reads,

$$f_x(x; x_0, r_{\bar{p}}) = \frac{f_p(x - x_0) + r_\alpha f_\alpha(x - x_0) + r_{\bar{p}} f_{\bar{p}}(x - x_0)}{1 + r_\alpha + r_{\bar{p}}} \quad (6.15)$$

where $r_\alpha \equiv 0.27/0.73$ is the ratio of muons originated from helium nuclei with respect to that from protons, and $r_{\bar{p}}$ is the antiproton to proton ratio. The three p.d.f terms (f_p , f_α , and $f_{\bar{p}}$) have the same forms represented by function (6.12) and the underlying deflection distribution (6.10) with corresponding parameters.

Because both, the total number of background events (N_{bck} , the muon flux if the Moon is absent) and the number of events blocked by the Moon (N_{miss}) are experimental results

and thus Poisson distributed, the extended maximum likelihood method [223] is appropriate for this analysis. The likelihood function is the product of the Poisson probability to find $\nu = N_{\text{bck}} - N_{\text{miss}}$, and n individual probabilities,

$$\begin{aligned}\mathcal{L}(\boldsymbol{\theta}) &= \frac{\nu^n}{n!} e^{-\nu} \prod_{i=1}^n f(x_i, y_i; \boldsymbol{\theta}) \\ &= \frac{e^{-\nu}}{n!} \prod_{i=1}^n \nu f(x_i, y_i; \boldsymbol{\theta}) \\ &= \frac{e^{-\nu}}{n!} \prod_{i=1}^n [N_{\text{bck}} f_{\text{bck}}(x_i, y_i; \boldsymbol{\theta}) - N_{\text{miss}} f_{\text{defi cit}}(x_i, y_i; \boldsymbol{\theta})]\end{aligned}\quad (6.16)$$

where $\boldsymbol{\theta} = (N_{\text{bck}}, N_{\text{miss}}, a, b, x_0, y_0, k, r_{\overline{p}})$ is the set of free parameters.

The log-likelihood function can then be written as

$$\ln \mathcal{L}(\boldsymbol{\theta}) = -(N_{\text{bck}} - N_{\text{miss}}) + \sum_{i=1}^n \ln [N_{\text{bck}} f_{\text{bck}}(x_i, y_i; \boldsymbol{\theta}) - N_{\text{miss}} f_{\text{defi cit}}(x_i, y_i; \boldsymbol{\theta})]$$

The additive terms not depending on $\boldsymbol{\theta}$ have been dropped. The background function $f_{\text{bck}}(x, y)$ has been normalised over the fitting range $(-X, -Y, X, Y)$ already. The deficit function $f_{\text{defi cit}}(x, y)$, on the other hand, which is only normalised over $(-\infty, \infty)$, has to be normalised to unity over the fitting range also. This can be solved by replacing N_{miss} with $N'_{\text{miss}} = N_{\text{miss}} / \int_{-X}^X \int_{-Y}^Y f_{\text{defi cit}}(x, y; \boldsymbol{\theta}) dx dy$. The log-likelihood function then reads,

$$\begin{aligned}\ln \mathcal{L}(\boldsymbol{\theta}) &= - \left[N_{\text{bck}} - N'_{\text{miss}} \int_{-X}^X \int_{-Y}^Y f_{\text{defi cit}}(x, y; \boldsymbol{\theta}) dx dy \right] \\ &\quad + \sum_{i=1}^n \ln [N_{\text{bck}} f_{\text{bck}}(x_i, y_i; \boldsymbol{\theta}) - N'_{\text{miss}} f_{\text{defi cit}}(x_i, y_i; \boldsymbol{\theta})]\end{aligned}\quad (6.17)$$

Thanks to the large statistics, the binned maximum likelihood method is also applicable in this analysis. Since the sum has been done partially in the binning, by integrating over the total number of bins, we obtain the log-likelihood function with binned data,

$$\begin{aligned}\ln \mathcal{L}(\boldsymbol{\theta}) &= - \left[N_{\text{bck}} - N'_{\text{miss}} \int_{-X}^X \int_{-Y}^Y f_{\text{defi cit}}(x, y; \boldsymbol{\theta}) dx dy \right] \\ &\quad + \sum_{i,j=1}^{N_{\text{bins}}} n_{i,j} \ln [N_{\text{bck}} f_{\text{bck}}(x_i, y_j; \boldsymbol{\theta}) - N'_{\text{miss}} f_{\text{defi cit}}(x_i, y_j; \boldsymbol{\theta})]\end{aligned}\quad (6.18)$$

where $n_{i,j}$ is the number of events of bin (i, j) .

6.6.2 Verification of the angular resolution

The shadowing effect of the Moon is a good opportunity to verify the precision of the angular measurement of an experiment. In this stage, antimatter is assumed absent in the primary

Table 6.7: Maximum likelihood fit to the unbinned Moon data sample with Landau approximation for the deflection distribution without antimatter content.

p_μ [GeV/c]	N_{miss}	a [deg $^{-1}$]	b [deg $^{-1}$]	x_{MPC} [$^\circ$]	y_0 [$^\circ$]	k	σ_{landau} [$^\circ$]
> 100	796 ± 97	0.0052(12)	0.040(2)	0.27(8)	0.02(3)	1.10(8)	0.38(1)
65-100	659 ± 163	0.0049(10)	0.040(1)	0.57(17)	-0.03(8)	0.66(17)	0.46(6)

Table 6.8: Maximum likelihood fit to the binned Moon data sample with Landau approximation for the deflection distribution without antimatter content.

p_μ [GeV/c]	N_{miss}	a [deg $^{-1}$]	b [deg $^{-1}$]	x_{MPC} [$^\circ$]	y_0 [$^\circ$]	σ [$^\circ$]	σ_{landau} [$^\circ$]
> 100	830 ± 160	0.0052(12)	0.040(2)	0.28(11)	0.06(4)	0.29(5)	0.40(7)
65-100	700 ± 180	0.0049(10)	0.040(1)	0.51(11)	-0.02(9)	0.35(6)	0.47(11)

cosmic ray flux and the deflection of muons from protons and helium nuclei are represented by a single Landau distribution (see Section 6.4.2) for simplicity.

The unbinned- and binned-maximum likelihood analyses produce similar results which are tabulated in Table 6.7 and Table 6.8, respectively. As expected, the unbinned method gives smaller uncertainties.

The values of the scaling factors k (or the effective angular resolutions σ) are within two standard deviations from its expected values $k = 1$ (for expected values of σ , see Table 6.5). Therefore, the pre-determined angular resolution with the double-muon data and CORSIKA simulation is confirmed with the Moon shadow data, though with larger uncertainties. The maximum of the deficits (x_{MPC}, y_0) are also consistent with the smoothed shadow images in Figure 6.18 and the expected value obtained in Section 6.4.3 (see results in Table 6.6). The mean values of y_0 indicate that the pointing precision of the L3+C experiment is better than 0.1° . The same fit procedure failed in the low momentum range (30 – 65 GeV/c) due to large uncertainties caused by the worse angular resolution.

6.6.3 Search for primary antiprotons

Binned data, Landau approximation

A similar method to the previous analysis [120] is tried with the Landau approximation (see Section 6.4.2). From the combined likelihood curve of the two muon momentum bands $p_\mu > 100$ GeV/c and $65 < p_\mu < 100$ GeV/c (see Figure 6.20), the ratio of antiproton to matter is determined to be

$$r_{\bar{p}/\text{matter}} = -0.04 \pm 0.08.$$

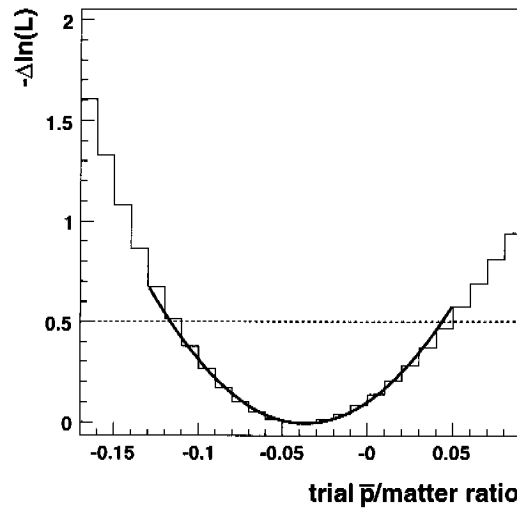


Figure 6.20: The relative log-likelihood value as function of the trial ratio of antiproton to matter obtained with binned data of $p_{\mu} > 65 \text{ GeV}/c$ with a Landau approximation.

According to [224], the upper limit of this ratio at 90% C.L. is 9.4%. As only 73% muons originated from primary protons, the upper limit of the antiproton to proton ratio is therefore

$$r_{\bar{p}/p}^{\text{limit}} = 13\% \text{ (90\% C.L.)}.$$

Comparing to the previous result, $r_{\bar{p}/\text{matter}} = -0.07 \pm 0.09$ [120], the current measurement has a slightly smaller uncertainty on the ratio. However, the previous work could set a lower limit, $r_{\bar{p}/p}^{\text{limit}} = 11\%$ (90% C.L.), thanks to the smaller value obtained for the antiproton to matter ratio. Taking into account the large uncertainties of the measurements, in fact, these two results are consistent. Or in other words, with the same method and the same momentum range, no improvement could be achieved with the improved angular resolution (the statistics being essentially the same).

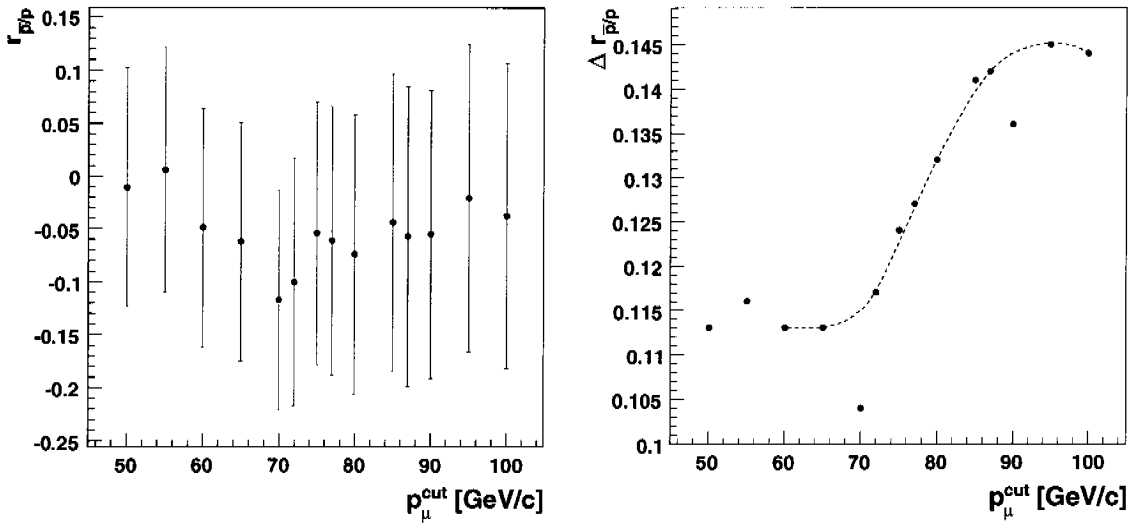
Unbinned data with a better deflection function

In order to improve the result, the more accurate p.d.f. (Function (6.12)) can be used.

In a first step, the p.d.f of antiprotons is assumed to be symmetric to that of protons. All together, there are nine free parameters, N_{bck} , N_{miss} , a , b , x_0 , y_0 , k_1 , k_2 , and $r_{\bar{p}/p}$. k_1 and k_2 are scaling parameters to the angular resolution (see Chapter 5) for the y - and x - axis respectively. The Moon data with different momentum cuts are fitted to function (6.17) with the unbinned maximum likelihood method using the minimisation package MINUIT [192] integrated in the ROOT framework [193]. The deduced parameters are listed in Table 6.9. The uncertainties of all the parameters except $r_{\bar{p}/p}$ are determined with the MIGRAD algorithm. The uncertainty of $r_{\bar{p}/p}$ is determined more precisely with the MINOS algorithm while the other parameters are fixed to the best fit values.

Table 6.9: Parameters obtained from the unbinned maximum likelihood fit for different momentum cuts.

p_{μ}^{cut} [GeV/c]	N_{miss} [$\times 10^3$]	$a[\text{deg}^{-1}]$	$b[\text{deg}^{-1}]$	$x_0[^\circ]$	$y_0[^\circ]$	k_1	k_2	$r_{\bar{p}/p}$
100	0.53(6)	0.0051(12)	0.040(2)	0.03(0)	0.00(1)	0.61(2)	1.79(1)	-0.038(144)
95	0.58(9)	0.0053(11)	0.040(1)	0.02(3)	0.00(4)	0.72(45)	1.60(6)	-0.021(145)
90	0.73(9)	0.0053(10)	0.040(1)	0.01(1)	-0.02(4)	0.82(25)	1.97(3)	-0.055(136)
85	0.77(11)	0.0053(10)	0.040(1)	0.05(6)	0.00(4)	0.76(23)	1.98(47)	-0.044(141)
80	0.88(13)	0.0054(9)	0.040(1)	0.03(3)	-0.01(3)	0.68(20)	2.13(42)	-0.074(132)
75	1.00(15)	0.0051(9)	0.040(1)	0.03(3)	-0.01(3)	0.74(21)	1.80(32)	-0.054(124)
70	1.03(16)	0.0054(8)	0.040(1)	0.02(3)	-0.01(4)	0.69(18)	1.60(39)	-0.117(104)
65	1.22(12)	0.0052(7)	0.040(1)	0.03(1)	0.00(3)	0.68(14)	1.66(3)	-0.062(113)
60	1.27(13)	0.0051(6)	0.041(6)	0.00(2)	0.00(3)	0.60(15)	1.16(39)	-0.049(113)
55	1.50(21)	0.0039(6)	0.040(1)	-0.02(7)	0.02(3)	0.53(10)	1.12(37)	0.006(116)
50	1.79(29)	0.0016(6)	0.040(1)	-0.02(9)	0.02(3)	0.59(15)	1.15(45)	-0.011(113)



(a) The \bar{p}/p ratio as a function of the muon momentum cut. (b) The uncertainty of the \bar{p}/p ratio as a function of the muon momentum cut (see text).

Figure 6.21: The antiproton to proton ratio and its uncertainty as a function of the muon momentum cut obtained with the two dimensional maximum likelihood with unbinned data.

Figure 6.21 presents the measured ratio of antiprotons to protons and its uncertainty as a function of the muon momentum cut. In order to better understand the dependence, more momentum-cut points are added to the figure. Above 70 GeV/c the statistical uncertainty

Table 6.10: The effect of different spectral indices on the \bar{p}/p ratio for Moon events above 70 GeV/c. The obtained \bar{p}/p ratio and in turn the upper limit (90% C. L.) as a function of the test value of the antiproton spectral index.

$\gamma_{\bar{p}}$ (test value)	$r_{\bar{p}/p}$	$r_{\bar{p}/p}^{\text{limit}}$ (90% C. L.)
-2.2	-0.130 ± 0.110	0.08
-2.7	-0.117 ± 0.104	0.08
-3.2	-0.020 ± 0.124	0.19
-3.7	-0.018 ± 0.124	0.18

becomes larger, as the statistics decreases. Below 70 GeV/c the uncertainty increases again because the angular resolution starts to play a role. Therefore, the best momentum cut corresponding to the lowest statistical uncertainty is 70 GeV/c. However, the uncertainty for this momentum-cut seems underestimated (because of fluctuations), and therefore a interpolated value from neighbouring points (see the curve in Figure 6.21(b)) is used instead

$$r_{\bar{p}/p} = -0.12 \pm 0.11 \quad (\text{for } p_{\mu} > 70 \text{ GeV}/c).$$

According to [224], the upper limit of this ratio at 90% C. L. is 8%.

6.6.4 The effect of different spectral indices on the \bar{p}/p ratio

Since the spectral index of antiprotons around the interesting energy range is unknown, the result may be biased. To check this point, primary antiprotons are assigned different spectral indices. For simplicity, assume only γ' among other parameters of Equation (6.5) depending on the input value of γ_0 with a simple relation $\gamma' = \gamma_0 + 1$. The \bar{p}/p ratio obtained in this way with the unbinned maximum likelihood fit for different antiproton spectral indices are tabulated in Table 6.10. The uncertainties of the results are determined by the total number of events and the angular resolution, and thus loosely correlated to the trial values of the antiproton spectral index. However, the absolute value of the \bar{p}/p ratio for a steep \bar{p} -spectrum is smaller.

The effect of different spectral indices on the \bar{p}/p ratio is also checked with a M.C. simulation (see Section 6.3.4). 10% of antiprotons with respect to protons are generated in the energy range of 200 to 2500 GeV with different spectral indices. The spectral index of protons is fixed to -2.7 . As shown in Table 6.11, significantly more muons are produced in the M.C. data samples with harder spectral index. On the other hand, the \bar{p}/p ratio, which is obtained with a binned maximum likelihood analysis similar to the one described in Section 6.6.3, is nearly independent of the input value of the spectral index.

Antiprotons with harder spectra may produce more secondary muons, but suffer less deflection in the Earth magnetic field, and therefore the \bar{p}/p ratio obtained with the maximum likelihood method is not sensitive to the spectral index.

Table 6.11: The effect of different spectral indices on assumed \bar{p}/p ratio equals to 0.1 for simulated data (see text for explanation).

$\gamma_{\bar{p}}$ (input)	$r_{\frac{N_{\mu}(\bar{p})}{N_{\mu}(p)}}$	$r_{\bar{p}/p}$ (fit)
-2.2	0.17	0.109
-2.7	0.096	0.106
-3.2	0.070	0.099
-3.7	0.050	0.096

6.7 Summary

The measurement on the ratio of antiprotons to protons in the primary flux has been performed with different methods. The results are consistent with each other. With a muon momentum cut of 70 GeV/c, the unbinned maximum likelihood analysis gives the \bar{p}/p ratio with the smallest uncertainty,

$$r_{\bar{p}/p} = -0.12 \pm 0.11 \quad (\text{for } p_{\mu} > 70 \text{ GeV}/c).$$

According to Equation (6.7), (6.8) and (6.9) and setting the “efficiency” factor to $1/e$, the corresponding energy range of primary protons is from 0.8 TeV to 2.4 TeV with a median energy of 1.2 TeV. The derived upper limit is shown in Figure 6.22 and compared to the previous L3+C result, some recent direct measurements of the \bar{p}/p ratio at low energies, and an upper limit obtained by MACRO using Sun shadow data.

In addition, the angular resolution is confirmed by the Moon shadow analysis and the pointing precision is determined to be better than 0.1° .

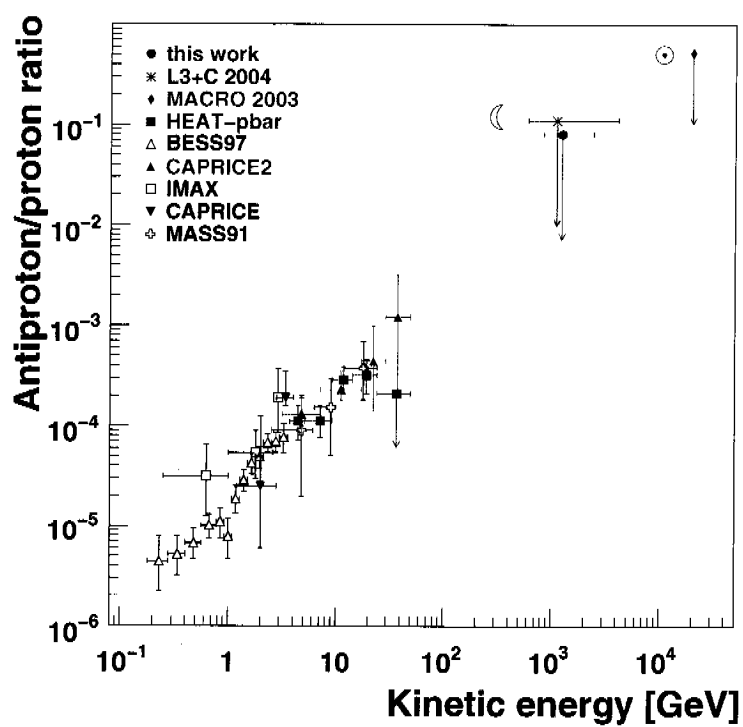


Figure 6.22: The upper limit of the antiproton to proton ratio (90% C.L.) compared with the previous L3+C result, some recent direct measurements at low energies (for references see Table 2.1), and an upper limit obtained by MACRO using Sun shadow data [209].

Chapter 7

Conclusion

This thesis presents a new search for antiprotons in high energy primary cosmic rays using the Moon shadow method with muon data collected by the L3+C experiment. The most important experimental requirement for a successful application of this new technique is the angular resolution of the detector. The angular smearing of the muons due to the production angle in the atmosphere, the multiple scattering and the energy losses in the matter above the L3+C set-up, as well as the intrinsic angular resolution of the detector, have been carefully determined with the help of Monte Carlo studies and the analysis of double muon events. The expected resolution, as well as the pointing precision ($< 0.1^\circ$) has been found in agreement with the result from the maximum likelihood analysis of the shadow data.

Shadows of the Moon have been observed for three muon momentum ranges: $> 100 \text{ GeV}/c$, $65 \text{ to } 100 \text{ GeV}/c$ and $30 \text{ to } 65 \text{ GeV}/c$, with a significance of 7.0σ , 5.8σ and 5.2σ respectively. The maximum likelihood analysis has been performed on both binned and un-binned data, delivering an upper limit for the ratio of antiprotons to protons in the primary flux of 0.08 (90% C. L.) and for primary energies around 1 TeV. At these energies the primary composition responsible for the observed muons corresponds to 73 % protons and 27 % helium and heavier nuclei. The resulting upper limit on the ratio has been demonstrated to be practically independent of the power index of the energy dependence of the primary flux.

For primary nucleons around 1 TeV no other experiment could presently compete with L3+C because of the excellent angular resolution and the low muon momentum threshold (corresponding also to a low primary momentum leading to a large deflection by the Earth magnetic field of the shadow image). Unfortunately the short data acquisition period has led to a quite limited statistics, inhibiting the possibility to get a better limit, or even to observe an antiproton flux at the % level of the proton flux, as one would expect by extrapolating from results obtained in direct measurements at low energies.

Bibliography

- [1] “First Circular – The 28th International Cosmic Ray Conference.” available at <http://www-rcn.icrr.u-tokyo.ac.jp/icrc2003/>, 2002.
- [2] T. K. Gaisser, “*Cosmic Rays and Particle Physics*”. Cambridge University press, Cambridge, 1990.
- [3] L. Jánossy, “*Cosmic Rays*”. Clarendon Press, Oxford, 2nd ed., 1948.
- [4] M. S. Longair, “*High energy astrophysics*”, vol. 1. Cambridge University Press, Cambridge, 2nd ed., 1992.
- [5] P. Le Coultre, “Astro-Teilchenphysik I+II.” Lecture Notes, ETH Zürich, 2002/2003.
- [6] V. Hess, “Unsolved Problems in Physics: Tasks for the Immediate Future in Cosmic Ray Studies,” in *Nobel Lectures. Physics 1922-1941*. Elsevier Publishing Company, Amsterdam, 1965.
- [7] R. K. Bock and A. Vasilescu, “*The Particle Detector BriefBook*”. 1999. available at <http://physics.web.cern.ch/Physics/ParticleDetector/BriefBook/>.
- [8] C. D. Anderson, “The Positive Electron,” *Phys. Rev.* **43** (1933) 491–494.
- [9] P. A. Dirac, “Theory of Electrons and Positrons,” in *Nobel Lectures. Physics 1922-1941*. Elsevier Publishing Company, Amsterdam, 1965.
- [10] C. D. Anderson and S. H. Neddermeyer, “Cloud Chamber Observations of Cosmic Rays at 4300 Meters Elevation and Near Sea-Level,” *Phys. Rev.* **50** (1936) 263–271.
- [11] S. H. Neddermeyer and C. D. Anderson, “Note on the Nature of Cosmic-Ray Particles,” *Phys. Rev* **51** (1937) 884–886.
- [12] S. H. Neddermeyer and C. D. Anderson, “Cosmic-Ray Particles of Intermediate Mass,” *Phys. Rev.* **54** (1938) 88–89.
- [13] R. A. Millikan, “Mesotron as the Name of the New Particle,” *Phys. Rev.* **55** (1939) 105.

- [14] H. Bhabha, "The Fundamental Length Introduced by the Theory of the Mesotron (Meson)," *Nature* **143** (1939) 276–277.
- [15] C. Powell, "The Cosmic Radiation," in *Nobel Lectures. Physics 1942-1962*. Elsevier Publishing Company, Amsterdam, 1964.
- [16] R. Battiston, "Rapporteur talk on Direct measurements and origin of Cosmic Rays," in *Proceedings of the 28th International Cosmic Ray Conference*, vol. 8, pp. 229–249. Tsukuba, Japan, 2003.
- [17] C. D. Anderson, "Energies of Cosmic-Ray Particles," *Phys. Rev.* **41** (1932) 405–421.
- [18] B. Rossi, "Interaction between cosmic rays and matter," *Nature* **132** (1933) 173–174.
- [19] B. Cassen, "On the Nature of Cosmic-Ray Showers," *Phys. Rev.* **44** (1933) 513.
- [20] C. D. Anderson, R. A. Millikan, S. Neddermeyer, and W. Pickering, "The Mechanism of Cosmic-Ray Counter Action," *Phys. Rev.* **45** (1934) 352–363.
- [21] W. H. Pickering, "A Note on the Production of Cosmic-Ray Showers," *Phys. Rev.* **47** (1935) 423.
- [22] D. K. Froman and J. C. Stearns, "Cosmic-Ray Showers and Bursts," *Rev. Mod. Phys.* **10** (1938) 133–192.
- [23] P. Auger, R. Maze, and T. Grivet-Meyer, "Large atmospheric cosmic showers containing ultra-penetrating corpuscles," *Comptes rendus* **206** (1938) 1721–1723.
- [24] P. Auger and R. Maze, "The great atmospheric cosmic showers," *Comptes rendus* **207** (1938) 228–230.
- [25] P. Auger, P. Ehrenfest, R. Maze, J. Daudin, and R. A. Fron, "Extensive Cosmic-Ray Showers," *Rev. Mod. Phys.* **11** (1939) 288–291.
- [26] "The story of high energy of cosmic rays."
<http://auger.ifj.edu.pl/Historia-s/Historia-s1A.htm>
- [27] J. Linsley, "Evidence for a Primary Cosmic-Ray Particle with Energy 10^{20} eV," *Phys. Rev. Lett.* **10** (1963) 146–148.
- [28] D. J. Bird *et al.*, "The cosmic-ray energy spectrum observed by the Fly's Eye," *Astrophys. J.* **424** (1994) 491–502.
- [29] The Auger Collaboration, "The Pierre Auger Project Design Report," 2nd ed., Fermilab, 1997. Available at <http://www.auger.org/tech.html>.
- [30] J. A. Simpson, "Elemental and Isotopic Composition of the Galactic Cosmic Rays," *Ann. Rev. Nucl. Part. Sci.* **33** (1983) 323–382.

- [31] W. Cronin, T. K. Gaisser, and S. P. Swordy, "Cosmic Rays at the Energy Frontier," *Sci. Amer.* **276** (1997) 44–49. the plot is also available at <http://astroparticle.uchicago.edu/archives.htm>.
- [32] A. Haungs, "Energy Spectrum and Mass Composition around the Knee by EAS Measurements," *J. Phys. G* **29** (2003) 809–820, astro-ph/0212481.
- [33] J. R. Hörandel, "Overview on direct and indirect measurements of cosmic rays — Some thoughts on galactic cosmic rays and the knee," in *Proceedings of the 19th European Cosmic Ray Symposium*. Florence, Italy, 2004. astro-ph/0501251.
- [34] **TOTEM** Collaboration, F. Ferro, "TOTEM physics," *Nucl. Phys. B - Proc Supp.* **146** (2004) 39–43.
- [35] T. Sako *et al.*, "LHCf: A new experiment to study very forward particle emission at LHC," in *Proceedings of 29th International Cosmic Ray Conference*. Pune, India, 2005.
- [36] K. Greisen, "End to the Cosmic-Ray Spectrum?," *Phys. Rev. Lett.* **16** (1966) 748–750.
- [37] G. Zatsepin and V. Kuzmin, "Upper limit of the spectrum of cosmic rays," *JETP Lett.* **4** (1966) 78–80.
- [38] D. F. Torres and L. A. Anchordoqui, "Astrophysical origins of ultrahigh energy cosmic rays," *Rep. Prog. Phys.* **67** (2004) 1663–1730.
- [39] Perkins, "*Particle Astrophysics*". Oxford University Press, 2003.
- [40] **JACEE** Collaboration, T. H. Burnett *et al.*, "JACEE emulsion chambers for studying the energy spectra of high energy cosmic ray protons and helium," *Nucl. Instr. and Meth. A* **251** (1986) 583–595.
- [41] K. Asakimori *et al.*, "Cosmic-Ray Proton and Helium Spectra: Results from the JACEE Experiment," *Astrophys. J.* **502** (1998) 278–283.
- [42] **RUNJOB** Collaboration, M. Hareyama *et al.*, "Energy determination of the cascade shower by means of a new type of emulsion chamber with diffuser module," *Nucl. Instr. and Meth. A* **512** (2003) 553–571.
- [43] **RUNJOB** Collaboration, V. A. Derbina *et al.*, "Cosmic-Ray Spectra and Composition in the Energy Range of 10-1000 TeV per Particle Obtained by the RUNJOB Experiment," *Astrophys. J.* **628** (2005) L41–L44.
- [44] **PAMELA** Collaboration, M. Circella, "The space mission PAMELA," *Nucl. Instr. and Meth. A* **518** (2004) 153–157.

- [45] **AMS-02** Collaboration, C. Lechanoine-Leluc, “AMS - A magnetic spectrometer on the International Space Station,” in *Proceedings of the 29th International Cosmic Ray Conference*. Pune, India, 2005.
- [46] T. Yoshida *et al.*, “BESS-polar experiment,” *Adv. Space Res.* **33** (2004) 1755–1762.
- [47] D. R. Lide, ed., “*CRC Handbook of Chemistry and Physics: a ready-reference book of chemical and physical data*”. CRC Press, 86th ed., 2005.
- [48] L. Anchordoqui *et al.*, “High energy physics in the atmosphere: phenomenology of cosmic ray air showers,” *Ann. Phys.* **314** (2004) 145–207.
- [49] A. Haungs, H. Rebel, and M. Roth, “Energy spectrum and mass composition of high-energy cosmic rays,” *Rep. Prog. Phys.* **66** (2003) 1145–1206.
- [50] S. Eidelman *et al.*, “Review of Particle Physics,” *Phys. Lett. B* **592** (2004) 1+.
- [51] I. A. Sokalski, E. V. Bugaev, and S. I. Klimushin, “MUM: Flexible precise Monte Carlo algorithm for muon propagation through thick layers of matter,” *Phys. Rev. D* **64** (2001) 074015, hep-ph/0010323. and references therein.
- [52] A. N. Cillis and S. J. Sciutto, “Extended air showers and muon interactions,” *Phys. Rev.* **64** (2001) 013010, astro-ph/0010488.
- [53] W. Rhode and C. Carloganu, “Muon Propagation in Water and Ice: Overview of Various Algorithms,” in *Proceedings of the Workshop on Simulation and Analysis Methods for Large Neutrino Telescopes*, C. Spiering, ed., p. 247. DESY Zeuthen, Germany, 1998.
- [54] K. Greisen, “Cosmic Ray Showers,” *Ann. Rev. Nucl. Sci.* **10** (1960) 63–108.
- [55] **Pierre Auger** Collaboration, X. Bertou, “Performance of the Pierre Auger Observatory surface array,” in *Proceedings of 29th International Cosmic Ray Conference*. Pune, India, 2005.
- [56] C. Bacci *et al.*, “Performance of the RPCs for the ARGO detector operated at the YangBaJing laboratory (4300m a.s.l.),” *Nucl. Instr. and Meth. A* **508** (2003) 110–115.
- [57] M. Unger, “*Measurement of the momentum spectrum of atmospheric muons with the L3 Detector*”. PhD thesis, Humboldt-University, Berlin, 2004.
- [58] **L3** Collaboration, P. Achard *et al.*, “Measurement of the atmospheric muon spectrum from 20 to 3000 GeV,” *Phys. Lett. B* **598** (2004) 15–32.
- [59] **EUSO** Collaboration, P. Gorodetzky, “Status report on the EUSO project at the end of phase A,” *Nucl. Phys. B - Proc Sup.* **138** (2004) 183–186.

- [60] J. Jelley *et al.*, “Radio pulses from extensive cosmic-ray air showers,” *Nature* **205** (1965) 327–328.
- [61] T. Huege and H. Falcke, “Radio emission from cosmic ray air showers. Coherent geosynchrotron radiation,” *Astron. Astrophys.* **412** (2003) 19–34, astro-ph/0309622.
- [62] H. Falcke *et al.*, “Detection and imaging of atmospheric radio flashes from cosmic ray air showers,” *Nature* **435** (2005) 313–316, astro-ph/0505383.
- [63] D. Heck, J. Knapp, J. Capdevielle, G. Schatz, and T. Thouw, “CORSIKA: A Monte Carlo Code to Simulate Extensive Air Showers,” FZKA 6019, Forschungszentrum Karlsruhe, 1998. See also <http://www-ik.fzk.de/corsika/>.
- [64] D. Heck, “The Air Shower Simulation Program CORSIKA,” in *Proceedings of the Workshop on Simulation and Analysis Methods for Large Neutrino Telescopes*, C. Spiering, ed., p. 228. DESY Zeuthen, Germany, 1998.
- [65] D. Heck and J. Knapp, “*Extensive Air Shower Simulations with CORSIKA: A User’s Guide*”. Institut für Kernphysik Forschungszentrum Karlsruhe, 2005.
- [66] N. N. Kalmykov and S. S. Ostapchenko, “The nucleus-nucleus interaction, nuclear fragmentation, and fluctuations of extensive air showers,” *Phys. Atom. Nucl.* **56** (1993) 346–353.
- [67] N. N. Kalmykov, S. S. Ostapchenko, and A. I. Pavlov, “Quark-Gluon-String Model and EAS Simulation Problems at Ultra-High Energies,” *Nucl. Phys. B - Proc Sup.* **52** (1997) 17–28.
- [68] K. Werner, “Strings, pomerons and the VENUS model of hadronic interactions at ultrarelativistic energies,” *Phys. Rep.* **232** (1993) 87–299.
- [69] J. Ranft, “Dual parton model at cosmic ray energies,” *Phys. Rev. D* **51** (1995) 64–84.
- [70] H. J. Drescher, M. Hladik, S. Ostapchenko, T. Pierog, and K. Werner, “Parton-based Gribov-Regge theory,” *Phys. Rep.* **350** (2001) 93–289, hep-ph/0007198.
- [71] R. S. Fletcher, T. K. Gaisser, P. Lipari, and T. Stanev, “SIBYLL: An event generator for simulation of high energy cosmic ray cascades,” *Phys. Rev. D* **50** (1994) 5710–5731.
- [72] J. N. Capdevielle, “A Monte Carlo generator for cosmic-ray collisions,” *J. Phys. G* **15** (1989) 909–924.
- [73] J. Knapp, D. Heck, S. J. Sciutto, M. T. Dova, and M. Risse, “Extensive air shower simulations at the highest energies,” *Astropart. Phys.* **19** (2003) 77–79.

- [74] <http://www.fluka.org/>.
- [75] S. Sciutto, “*AIRES User’s Manual and Reference Guide; version 2.6.0*”, 2002. available at <http://www.fisica.unlp.edu.ar/auger/aires/>.
- [76] R. Engel, G. Barr, T. Gaisser, S. Robbins, and T. Stanev, “TARGET 2.2 A Hadronic Interaction Model for Studying Inclusive Muon and Neutrino Fluxes,” in *Proceedings of the 28th International Cosmic Ray Conference*. Tsukuba, Japan, 2003.
- [77] “astronomy,” in *Encyclopædia Britannica Online*. <http://search.eb.com/eb/article-9108656> [Accessed 11 August 2005].
- [78] O. Chamberlain, E. Segrè, C. Wiegand, and T. Ypsilantis, “Observation of Antiprotons,” *Phys. Rev.* **100** (1955) 947–950.
- [79] A. D. Sakharov, “Violation of CP Invariance, C Asymmetry, and Baryon Asymmetry of the Universe,” *JETP Lett.* **5** (1967) 24–27.
- [80] P. D. B. Collins, Martin, A. Douglas, Squires, and E. J., “*Particle physics and cosmology*”. Wiley, New York, 1989.
- [81] G. Steigman, “Observational tests of antimatter cosmologies,” *Ann. Rev. Astron. Astrophys.* **14** (1976) 339–372.
- [82] AMS Collaboration, J. Alcaraz *et al.*, “Search for antihelium in cosmic rays,” *Phys. Lett. B* **461** (1999) 387–396.
- [83] H. Fuke *et al.*, “Search for Cosmic-Ray Antideuterons,” *Phys. Rev. Lett* **95** (2005) 081101, [astro-ph/0504361](http://arxiv.org/abs/astro-ph/0504361).
- [84] D. C. Kennedy, “Cosmic Ray Antiprotons,” [astro-ph/0003485](http://arxiv.org/abs/astro-ph/0003485).
- [85] R. L. Golden *et al.*, “Evidence for the existence of cosmic-ray antiprotons,” *Phys. Rev. Lett.* **43** (1979) 1196–1199.
- [86] R. L. Golden, B. G. Mauger, S. Nunn, and S. Horan, “Energy dependence of the \bar{P}/P ratio in cosmic rays,” *Astrophys. Lett.* **24** (1984) 75–83.
- [87] A. Buffington, S. M. Schindler, and C. R. Pennypacker, “A measurement of the cosmic-ray antiproton flux and a search for antihelium,” *Astrophys. J.* **248** (1981) 1179–1193.
- [88] R. E. Streitmatter, S. J. Stochaj, R. L. Ormes, J. F. Golden, and S. A. Stephens, “Experimental limit on low energy antiprotons in the cosmic radiation,” *Adv. Space Res.* **9** (1989) 65–69.

- [89] S. P. Ahlen, J. J. Beatty, S. Barwick, G. Gerbier, and C. R. Bower, "New limit on the low-energy antiproton/proton ratio in the Galactic cosmic radiation," *Phys. Rev. Lett.* **61** (1988) 145–148.
- [90] M. H. Salamon *et al.*, "Limits on the antiproton/proton ratio in the cosmic radiation from 100 MeV to 1580 MeV," *Astrophys. J.* **349** (1990) 78–90.
- [91] M. Hof *et al.*, "Measurement of Cosmic-Ray Antiprotons from 3.7 to 19 GeV," *Astrophys. J.* **467** (1996) L33–L36.
- [92] G. Basini *et al.*, "The Flux of Cosmic Ray Antiprotons from 3.7 to 24 GeV," in *Proceedings of 26th International Cosmic Ray Conference, OG.1.1.21*. Salt Lake City, 1999.
- [93] J. W. Mitchell *et al.*, "Measurement of 0.25-3.2 GeV Antiprotons in the Cosmic Radiation," *Phys. Rev. Lett.* **76** (1996) 3057–3060.
- [94] K. Yoshimura *et al.*, "Observation of cosmic-ray antiprotons at energies below 500 MeV," *Phys. Rev. Lett.* **75** (1995) 3792–3795.
- [95] BESS Collaboration, A. Moiseev *et al.*, "Cosmic-Ray Antiproton Flux in the Energy Range from 200 to 600 MeV," *Astrophys. J.* **474** (1997) 479–489.
- [96] M. Boezio, "The Cosmic-Ray Antiproton Flux between 0.62 and 3.19 GeV Measured Near Solar Minimum Activity," *Astrophys. J.* **487** (1997) 415–423.
- [97] H. Matsunaga *et al.*, "Measurement of Low-Energy Cosmic-Ray Antiprotons at Solar Minimum," *Phys. Rev. Lett.* **81** (1998) 4052–4055, astro-ph/9809326.
- [98] S. Orito *et al.*, "Precision Measurement of Cosmic-Ray Antiproton Spectrum," *Phys. Rev. Lett.* **84** (2000) 1078–1081, astro-ph/9906426.
- [99] T. Maeno *et al.*, "Successive measurements of cosmic-ray antiproton spectrum in a positive phase of the solar cycle," *Astropart. Phys.* **16** (2001) 121–128, astro-ph/0010381.
- [100] D. Bergström *et al.*, "First Mass-resolved Measurement of High-Energy Cosmic-Ray Antiprotons," *Astrophys. J.* **534** (2000) L177–L180.
- [101] M. Boezio *et al.*, "The cosmic-ray antiproton flux between 3 and 49 GeV," *Astrophys. J.* **561** (2001) 787–799, astro-ph/0103513.
- [102] AMS Collaboration, M. Aguilar *et al.*, "The Alpha Magnetic Spectrometer (AMS) on the International Space Station: Part I - results from the test flight on the space shuttle," *Phys. Rep.* **366** (2002) 331–405.

- [103] Y. Asaoka, "Measurements of Cosmic-Ray Low-Energy Antiproton and Proton Spectra in a Transient Period of Solar Field Reversal," *Phys. Rev. Lett.* **88** (2002) 051101, astro-ph/0109007.
- [104] A. S. Beach *et al.*, "Measurement of the Cosmic-Ray Antiproton-to-Proton Abundance Ratio between 4 and 50 GeV," *Phys. Rev. Lett.* **87** (2001) 271101, astro-ph/0111094.
- [105] S. Haino, "Measurement of cosmic-ray antiproton spectrum with BESS-2002," in *Proceedings of the 29th International Cosmic Ray Conference*. Pune, India, 2005.
- [106] Matsuda, "Observation of low energy antiprotons at the 2004 BESS-Polar flight in Antarctica," in *Proceedings of the 29th International Cosmic Ray Conference*. Pune, India, 2005.
- [107] S. A. Stephens and R. L. Golden, "The role of antiprotons in cosmic-ray physics," *Space Sci. Rev.* **46** (1987) 31–91.
- [108] S. A. Stephens, "Antiproton upper limits from the observed charge ratio of muons and their implications for cosmic ray models," *Astron. and Astrophys.* **149** (1985) 1–6.
- [109] L3 Collaboration, M. Unger, "Results from L3+C," in *Proceedings of the 19th European Cosmic Ray Symposium*. Florence, Italy, 2004.
- [110] P. Le Coultre, "Cosmic Ray Observation and Results from Experiments Using LEP Detectors at CERN," in *Proceedings of the 29th International Cosmic Ray Conference*. Pune, India, 2005.
- [111] T. K. Gaisser and R. K. Schaefer, "Cosmic-ray secondary antiprotons - A closer look," *Astrophys. J.* **394** (1992) 174–183.
- [112] L. Bergström, J. Edsjö, and P. Ullio, "Cosmic Antiprotons as a Probe for Supersymmetric Dark Matter?," *Astrophys. J.* **526** (1999) 215–235, astro-ph/9902012.
- [113] F. Donato *et al.*, "Antiprotons from Spallations of Cosmic Rays on Interstellar Matter," *Astrophys. J.* **563** (2001) 172–184, astro-ph/0103150.
- [114] I. V. Moskalenko, A. W. Strong, J. F. Ormes, and M. S. Potgieter, "Secondary Antiprotons and Propagation of Cosmic Rays in the Galaxy and Heliosphere," *Astrophys. J.* **565** (2002) 280–296, astro-ph/0106567.
- [115] R. Duperray, "Flux of light antimatter nuclei near Earth, induced by cosmic rays in the Galaxy and in the atmosphere," *Phys. Rev. D* **71** (2005) 083013, astro-ph/0503544.

- [116] T. Bringmann, “High-energetic Cosmic Antiprotons from Kaluza-Klein Dark Matter,” *J. Cosmol. Astropart. Phys.* **8** (2005) 6, astro-ph/0506219.
- [117] M. Chemarin, J. F. Parriaud, and Y. P. Xu, “Limit on High Energy Antiproton Flux in Space from the Shadowing of Cosmic Rays by the Moon,” L3 Note 2819, 2003.
- [118] A. Barrau *et al.*, “Antiprotons from primordial black holes,” *Astron. and Astrophys.* **388** (2002) 676–687, astro-ph/0112486.
- [119] J.-F. Parriaud, “*Recherche d’antimatière dans les rayons cosmiques en utilisant l’ombre de la Lune et de sources cosmiques avec le détecteur à muons de L3*”. PhD thesis, Université Claude Bernard - Lyon I, 2003.
- [120] L3 Collaboration, P. Achard *et al.*, “Measurement of the shadowing of high-energy cosmic rays by the Moon: A search for TeV-energy antiprotons,” *Astropart. Phys.* **23** (2005) 411–434.
- [121] Y. P. Xu, “Angular Resolution of the L3+C Experiment,” L3+C internal note, 2003.
- [122] L3 Collaboration, B. Adeva *et al.*, “The construction of the L3 experiment,” *Nucl. Instr. and Meth. A* **289** (1990) 35–102.
- [123] P. Le Coultre *et al.*, “L3, A new Tool for Cosmic Ray Muon Studies and the Search of High Energy Cosmic Ray Sources,” L3 note 1676, 1994.
- [124] U. Becker *et al.*, “Precision Measurement of the Cosmic Ray Muon Momentum Spectrum between 20 and 2000 GeV/c – A Letter of Intent –,” L3 note 1977, 1996.
- [125] J. Bähr *et al.*, “Physics Topics of the L3+Cosmics Experiment, Phase II,” L3+C internal note, 1997.
- [126] B. Petersen, C. Timmermans, and H. Wilkens, “Properties of the 98 data,” L3+C internal note, 1999.
- [127] The Muon Group of the L3 Collaboration, B. Adeva, *et al.*, “Muon detection in the L3 experiment at LEP,” *Nucl. Instr. and Meth. A* **277** (1989) 187–193.
- [128] The Muon Group of the L3 Collaboration, B. Adeva, *et al.*, “Test results of the L3 precision muon detector,” *Nucl. Instr. and Meth. A* **289** (1990) 335–341.
- [129] The Muon Group of the L3 Collaboration, B. Adeva, *et al.*, “Study of θ -inclined tracks in L3 muon chambers,” *Nucl. Instr. and Meth. A* **290** (1990) 115–121.
- [130] The Muon Group of the L3 Collaboration, B. Adeva, *et al.*, “A high resolution muon detector,” *Nucl. Instr. and Meth. A* **323** (1992) 109–124.
- [131] A. van Mil, “*Cosmic Ray Muons in the L3 Detector*”. PhD thesis, Nijmegen, 2000.

- [132] L3+C Collaboration, O. Adriani *et al.*, “The L3+C detector, a unique tool-set to study cosmic rays,” *Nucl. Instr. and Meth. A* **488** (2002) 209–225.
- [133] Philips, “XP2020, 12-stage photomultiplier tube”, 1989.
- [134] “DGRF/IGRF Geomagnetic Field Model 1945 - 2010 and Related Parameters.”
<http://nssdc.gsfc.nasa.gov/space/model/models/igrf.html>.
- [135] H. Wilkens, “*Experimental study of high energy muons from Extensive Air Showers in the energy range 100 TeV to 10 PeV*”. PhD thesis, University of Nijmegen, 2003.
- [136] H. Groenstege, T. Wijnen, P. Rewiersma, and J. Stolte, “CPC (Cosmic Personality Card) for the L3+Cosmics experiment,” ETR 99-02, 1999.
- [137] J. Christiansen, “32 channel general purpose TDC,” CERN/ECP-MIC, 1997.
- [138] H. Groenstege, T. Wijnen, P. Rewiersma, and J. Stolte, “NIMROD, 16 channel readout driver for the Drift Chambers used in the L3+Cosmics project,” ETR 99-06, 1999.
- [139] H. Verkooijen, “CTT-V2 - Cosmics Trigger and Timing module for phase 2 of the L3+Cosmic project,” ETR 99-01, NIKHEF, 1999.
- [140] T. Wijnen, B. Petersen, and C. Timmermans, “The L3+Cosmics Data Format,” HEN-425, 1999.
- [141] CN/ASD Group, “PAW – Physics Analysis Workstation”. CERN, 1999. See also <http://cern.ch/paw>.
- [142] CN/ASD Group, “GEANT – Detector Description and Simulation Tool”. CERN, 1994. See also <http://wwwinfo.cern.ch/asd/geant/index.html>.
- [143] B. Petersen, “*The Cosmic Ray Induced Muon Spectrum Measured With the L3 Detector*”. PhD thesis, University of Nijmegen, 2002.
- [144] A. Korn, “Cosmic muons in the L3 detector,” Master’s thesis, Humboldt University, Berlin, 1998.
- [145] R. Ramelli, “*Search for Cosmic Ray Point Sources and Anisotropy Measurement with the L3+C Experiment*”. PhD thesis 14683, ETH Zürich, 2002.
- [146] M. Zillig, “L3+Cosmics First Data Analysis - Reconstruction of Very Inclined Tracks,” Master’s thesis, ETH Zürich, 1998.
- [147] V. Karimäki, “Effective circle fitting for particle trajectories,” *Nucl. Instr. and Meth.* **305** (1991) 187–191.

- [148] V. Innocente, M. Maire, and E. Nagy, “*GEANE: Average Tracking and Error Propagation Package*”. CERN, 1991. W5013-E.
- [149] M. Unger, “Muon chamber alignment,” L3+C internal note, 2001.
- [150] V. Schmitt, “Analysis of Multi Muon Events in the L3 Detector,” Master’s thesis, Humboldt University, Berlin, 2000.
- [151] L. Li, “Cross Octant Reconstruction Program,” L3+C internal note, 2002.
- [152] F. Zhang, “The COL3 Cross-Octant (Version 2.0) Reconstruction Program,” L3+C internal note, 2003.
- [153] T. Hebbeker and A. Korn, “Simulation Programs for the L3-Cosmics Experiment,” L3+C internal note, 1998.
- [154] “L3+C webpage.”
<http://cern.ch/l3c>.
- [155] L3+C Collaboration, P. Le Coultre, “L3+C: Selected Results,” in *Proceedings of XIII International Symposium on Very High Energy Cosmic Ray Interactions*. Pylos, Greece, 2004.
- [156] E. V. Bugaev *et al.*, “Atmospheric muon flux at sea level, underground, and underwater,” *Phys. Rev. D* **58** (1998) 054001, hep-ph/9803488.
- [157] Q. Q. Zhu, “Search for point sources through muons,” L3+C internal note, 2002.
- [158] Z. G. Yao, “An All Sky Survey for Short Period Burst Signals, Using the L3+C Muon Detector,” presentation on ETH/IPP internal meeting, 2004.
- [159] L3+C Collaboration, P. Le Coultre, “Observation of a Flare Signal from a Fixed Position in the Northern Hemisphere through Muons with L3+C,” in *Proceedings of the 29th International Cosmic Ray Conference*. Pune, India, 2005.
- [160] M. V. D. Akker, “Search for TeV Gamma-Rays in Gamma-Ray Bursts with the L3+Cosmics detector,” L3+C internal note, 2003.
- [161] L. K. Ding, “Multi-Muon Events near Air Shower Cores seen by L3+Cosmic and the “Knee” Composition,” L3+C internal note, 2001.
- [162] F. Zhang, “*The study of the cosmic rays physics in the “KNEE” region using multiple muon events with the L3+C Experiment*”. PhD thesis, Graduate School of Chinese Academy of Science, Beijing, 2004. (In Chinese).
- [163] Z. Li, “Search for Muon-Burst Correlated to the Big Solar Flare in July 14 of 2000,” L3+C internal note, 2000.

- [164] Y. Q. Ma and Q. Q. Zhu, "An Overview of the Recent Work on Solar Flare Search," L3+C internal note, 2004.
- [165] P. Ladron, "The solar-flare of 14/July/2000. A running means search," L3+C internal note, 2004.
- [166] L3+C Collaboration, Y. Q. Ma, "Search for Kolar-like Events from L3+C Data," in *Proceedings of the 29th International Cosmic Ray Conference*. Pune, India, 2005.
- [167] L3+C Collaboration, X. H. Ma, "A Search for Low Velocity Exotic Particles with the L3+C Spectrometer," in *Proceedings of the 29th International Cosmic Ray Conference*. Pune, India, 2005.
- [168] P. Ladron, "Some statistics based on the COSM and MUCH Databases contents," L3+C internal note, 1999.
- [169] "The L3+C online logbooks 1999 and 2000."
http://cern.ch/~xuyyp/l3c_log.html.
- [170] P. Ladron, "The "good-bad guys" selection," L3+C internal note, 2000.
- [171] P. Ladron, "The different versions of the good-bad guys," L3+C internal note, 2001.
- [172] R. Leiste, "Short Description of the extended gb_guys files," L3+C internal note, 2001.
- [173] R. Nahnauer, "How to select unbiased L3+C data," L3+C internal note, 2001.
- [174] F. Zhang, "L3+C NTPL VERSION XO v2.0 Description," L3+C internal note, 2003.
- [175] Z. G. Yao, "GPS time corrections," L3+C internal presentation (general meeting), February, 2003.
- [176] Y. Becherini *et al.*, "Time correlations of high energy muons in an underground detector," *Astropart. Phys.* **23** (2005) 341–348.
- [177] H. A. Bethe, "Molire's Theory of Multiple Scattering," *Phys. Rev.* **89** (1953) 1256–1266.
- [178] W. T. Scott, "The Theory of Small-Angle Multiple Scattering of Fast Charged Particles," *Rev. Mod. Phys.* **35** (1963) 231–313.
- [179] G. Shen *et al.*, "Measurement of multiple scattering at 50 to 200 GeV/c," *Phys. Rev. D* **20** (1979) 1584–1588.
- [180] S. A. Akimenko *et al.*, "Multiple coulomb scattering of 7.3 and 11.7 GeV/c muons on a Cu target," *Nucl. Instr. and Meth. A* **243** (1986) 518–522.

- [181] A. V. Butkevich, R. P. Kokoulin, G. V. Matushko, and S. P. Mikheyev, "Comments on multiple scattering of high-energy muons in thick layers," *Nucl. Instr. and Meth. A* **488** (2002) 282–294.
- [182] B. Rossi and K. Greisen, "Cosmic-Ray Theory," *Rev. Mod. Phys.* **13** (1941) 240–309.
- [183] B. Rossi, "*High energy particles*". Prentice-Hall, Englewood Cliffs, N.J., 1952.
- [184] V. L. Highland, "Some practical remarks on multiple scattering," *Nucl. Instr. and Meth.* **129** (1975) 497–499. Erratum: *Nucl. Instr. and Meth.* **161** (1979) 171.
- [185] G. R. Lynch and O. I. Dahl, "Approximations to multiple Coulomb scattering," *Nucl. Instr. and Meth. B* **58** (1991) 6–10.
- [186] D. Chirkin and W. Rhode, "Muon Monte Carlo: a high-precision tool for muon propagation through matter," hep-ph/0407075.
- [187] **Soudan 2** Collaboration, J. Cobb *et al.*, "Observation of a shadow of the Moon in the underground muon flux in the Soudan 2 detector," *Phys. Rev. D* **61** (2000) 092002.
- [188] **MACRO** Collaboration, M. Ambrosio *et al.*, "Observation of the shadowing of cosmic rays by the Moon using a deep underground detector," *Phys. Rev. D* **59** (1999) 012003.
- [189] P. Majumdar *et al.*, "Angular resolution of the Pachmarhi array of Cerenkov telescopes," *Astropart. Phys.* **18** (2003) 333–349.
- [190] **TIBET AS γ** Collaboration, M. Amenomori *et al.*, "Performance of the Tibet-III Air-Shower Array," in *Proceedings of the 27th International Cosmic Ray Conference, HE, 1.6*. Hamburg, Germany, 2001.
- [191] M. Merck *et al.*, "Methods to determine the angular resolution of the HEGRA extended air shower scintillator array," *Astropart. Phys.* **5** (1996) 379–392.
- [192] CN/ASD Group, "*MINUIT – Function Minimization and Error Analysis*". CERN, 1998. See also <http://cern.ch/paw>.
- [193] R. Brun and F. Rademakers, "ROOT - An Object Oriented Data Analysis Framework," in *Proceedings AIHENP'96 Workshop*. Lausanne, Switzerland, September, 1996. See also <http://root.cern.ch/>.
- [194] J. Milke *et al.*, "Test of interaction models with the KASCADE hadron calorimeter," *Nucl. Phys. B - Proc. Sup.* **122** (2003) 388–391.
- [195] D. Heck, "Low Energy Hadronic Interaction Models," in *Proceedings of the XIII International Symposium on Very High Energy Cosmic Ray Interactions*. Pylos, Greece, 2004. astro-ph/0410735. *Nucl. Phys. B (Proc. Suppl.)* in print.

- [196] G. W. Clark, "Arrival Directions of Cosmic-Ray Air Showers from the Northern Sky," *Phys. Rev.* **108** (1957) 450–457.
- [197] D. E. Alexandreas *et al.*, "Observation of shadowing of ultrahigh-energy cosmic rays by the Moon and the Sun," *Phys. Rev. D* **43** (1991) 1735–1738.
- [198] M. Urban, P. Fleury, R. Lestienne, and F. Plouin, "Can we detect antimatter from other galaxies by the use of the Earth's magnetic field and the Moon as an absorber?," *Nucl. Phys. B - Proc Sup.* **14** (1990) 223–236.
- [199] A. Borione *et al.*, "Observation of the shadows of the Moon and Sun using 100 TeV cosmic rays," *Phys. Rev. D* **49** (1994) 1171–1177.
- [200] **TIBET AS γ** Collaboration, M. Amenomori *et al.*, "Cosmic-ray deficit from the directions of the Moon and the Sun detected with the Tibet air-shower array," *Phys. Rev. D* **47** (1993) 2675–2681.
- [201] **TIBET AS γ** Collaboration, M. Amenomori *et al.*, "Direct Evidence of the Interplanetary Magnetic Field Effect on the Cosmic-Ray Shadow by the Sun," *Astrophys. J.* **415** (1993) L147–L150.
- [202] **TIBET AS γ** Collaboration, M. Amenomori *et al.*, "Antiproton Proton Ratio at 10^{13} eV Inferred from the Superposition of Sun Shadows Using the Tibet Air Shower Array," in *Proceedings of the 24th International Cosmic Ray Conference.*, vol. 3, pp. 84–87. Rome, Italy, 1995.
- [203] **TIBET AS γ** Collaboration, K. Hibino, "An Upper Limit on Cosmic-ray Antiproton/proton Flux Ratio Estimated by the Moon's Shadow with the Tibet III Air Shower Array," in *Proceedings of the 29th International Cosmic Ray Conference. HE 1.1.* Pune, India, 2005.
- [204] **Milagro** Collaboration, M. Wascko, "Study of the Shadow of the Moon and Sun with VHE Cosmic Rays," in *Proceedings of the 26th International Cosmic Ray Conference.* Salt Lake City, USA, 1999.
- [205] M. O. Wascko, "Study of the shadow of the moon in very high energy cosmic rays with the Milagrito water Cherenkov detector". PhD thesis, University of California, Riverside, 2001.
- [206] **Milagro** Collaboration, X. Xu, "The Cosmic Ray Shadows of the Moon and the Sun Detected by the Milagro Gamma Ray Observatory," in *Proceedings of the 28th International Cosmic Ray Conference.* Tsukuba, Japan, 2003.
- [207] D. Pomaredé *et al.*, "A new optical filter for the ARTEMIS experiment," *Nucl. Instr. and Meth. A* **446** (2000) 469–489.

- [208] B. Bartoli, "Observation of the Moon shadow using a new reconstruction technique in the CLUE experiment," *IL Nuovo Cimento* **24** (2001) 669–674.
- [209] **MACRO** Collaboration, M. Ambrosio *et al.*, "Moon and Sun shadowing effect in the MACRO detector," *Astropart. Phys.* **20** (2003) 145–156.
- [210] M. A. Hapgood, "Space physics coordinate transformations: A user guide," *Planet. Space Sci.* **40** (1992), no. 5, 711–717. Corrigendum: *Planet. Space Sci.*, **40** (1997), 1047.
- [211] M. Mayoud, "Applied metrology for LEP," in *CERN Accelerator School on Applied Geodesy for Particle Accelerators [CERN-87-01]*, S. Turner, ed., CERN. 1986.
- [212] International Association of Geomagnetism and Aeronomy (IAGA), Division V, Working Group VMOD: Geomagnetic Field Modeling, "The 10th-Generation International Geomagnetic Reference Field," *Geophys. J. Int.* **161** (2005) 561–565. See also <http://www.ngdc.noaa.gov/seg/geomag/>.
- [213] D. P. Stern, "The art of mapping the magnetosphere," *J. Geophys. Res.* **99** (1994) 17169–17198.
- [214] N. A. Tsyganenko, "Quantitative models of the magnetospheric magnetic field - Methods and results," *Space Sci. Rev.* **54** (1990) 75–186.
- [215] C. E. Jordan, "Empirical models of the magnetospheric magnetic field," *Rev. Geophys.* **32** (1994) 139–158.
- [216] N. A. Tsyganenko, "Modeling the Earth's magnetospheric magnetic field confined within a realistic magnetopause," *J. Geophys. Res.* **100** (1995) 5599–5612.
- [217] J. H. King and N. E. Papitashvili, "Solar wind spatial scales in and comparisons of hourly Wind and ACE plasma and magnetic field data," *J. Geophys. Res.* **110** (2005) A2104. See also <http://nssdc.gsfc.nasa.gov/omniweb/>.
- [218] C. Russell, "The solar wind interaction with the Earth's magnetosphere: a tutorial," *IEEE Trans. Plasma Sci.* **28** (2000) 1818–1830. a color version available at http://http://www-ssc.igpp.ucla.edu/personnel/russell/papers/chrono/in_press.html.
- [219] A. K. Das and A. K. De, "The interrelation between the primary cosmic-ray nucleon and sea-level muon energies using the scaling model," *J. Phys. G* **6** (1980) 411–412.
- [220] J. R. Hörandel, "On the knee in the energy spectrum of cosmic rays," *Astropart. Phys.* **19** (2003) 193–220, astro-ph/0210453.
- [221] P. T. Wallace, "SLALIB — Positional Astronomy Library," starlink user note 67, CCLRC / Rutherford Appleton Laboratory, 2003. <http://star-www.rl.ac.uk/star/docs/sun67.htx/sun67.html>.

- [222] P. Wallace. private communication, 2002.
- [223] G. Cowan, "*Statistical Data Analysis*". Oxford University Press, 1998.
- [224] G. J. Feldman and R. D. Cousins, "Unified approach to the classical statistical analysis of small signals," *Phys. Rev. D* **57** (1998) 3873–3889.

List of Abbreviations

CERN	European Organization for Nuclear Research the original name in French: Centre European pour la Recherche Nucleaire
C. L.	Confidence Level
CTT	Cosmics Trigger and Timing Module
DAQ	Data AcQuisition
EAS	Extensive Air Showers
GPS	Global Positioning System
GRB	Gamma-Ray Burst (γ -Ray Burst)
GUT	Grand Unification Theory
GZK	Greise-Zatsepin-Kuzmin (cutoff)
IMF	Interplanetary Magnetic Field
L3+C	L3+Cosmic
LEP	Large Electron Positron collider
M. C.	Monte Carlo
MDR	Maximum Detectable Rigidity
NKG	Nishimura-Kamata-Greisen (formula)
PMT	Photo Multiplier Tube
QED	Quantum Electromagnetic Dynamics
R. A.	Right Ascension
RICH	Ring Imaging Cherenkov Counter
TDC	Time Data Converter
TOF	Time Of Flight
TRD	Transition Radiation Detector

Acknowledgements

I am very grateful to Prof. Felicitas Pauss for giving me the opportunity to work on this interesting subject in her group at CERN, for supporting my attendance to international conference and schools, and for the helpful comments on my thesis. I would like to express my thanks to Prof. Jan Olof Stenflo for his acceptance to be my co-referee.

I wish to express my sincere appreciation to Dr. Pierre Le Coultre for his guidance and encouragement over the years. In addition to the discussions on physics and data analysis, he also carefully scrutinised the many drafts of this thesis and corrected my English. And thanks for his invitations to the Vallée de Joux.

I would like to thank Dr. Yao Zhiguo for providing me experiences on data analysis and computing, as well as his effort on managing the data production and making the data access as easy as possible which I benefited directly. Thanks also for his long friendship.

I am indebted to many colleagues of the L3+C collaboration. Particular thanks go to Dr. Michel Chemarin and Jean-Francois Parriaud for introducing me to the data analysis and our many discussions at the early stage of this thesis. I wish to thank Prof. Ma Yuqian, Prof. Zhu Qingqi, Dr. Pedro Ladron De Guevara, Dr. Michael Unger, Dr. Yu Lei, and Prof. Larry Jones for their helpful comments. I want to thank Zhang Feng, who finalised and improved the “cross-octant” event reconstruction and therefore made all the data available to this analysis.

I wish to thank our group secretary, Gabriele Kogler, for her kind services.

Finally, I would like to express my gratitude to my family for their constant support and understanding.

Curriculum Vitae

- April 10, 1971** Born in Jilin, China
- 1978-1983** Primary school in Jilin, China
- 1983-1986** Secondary school in Jilin, China
- 1986-1989** High school in Jilin, China
- 1989-1993** Studied Physics at Jilin University, China.
- 1993-2002** Worked at the Laboratory for cosmic ray and high energy astrophysics of the Institute of High Energy Physics (IHEP), Beijing, China. Worked mainly on a satellite-borne gamma-ray burst monitor. I developed part of the DAQ system including both the hardware and software, as well as a dedicated test system. I was responsible for the detector simulation, in-flight calibration, run control, data processing and analysis. In addition, I also worked on a large balloon-borne X-ray detector, and did some pilot work (simulation, writing proposal) on a soft X-ray spectrometer for a lunar explorer.
- 1998-1999** Worked at CERN within the L3+C collaboration. Participated in the online software development, scintillation detector installation and test, as well as data taking and data quality check.
- July 2001** Obtained Master's degree in Science under the supervision of Prof. Yuqian Ma.
- 2002-2005** Worked on astroparticle physics at CERN as a PhD candidate within the group of the Institute for Particle Physics of ETH Zürich, under the supervision of Prof. Dr. Felicitas Pauss, and Dr. Pierre Le Coultre.